

Nanoparticle Forming Reactive Plasmas: A Multidiagnostic Approach

Dissertation

zur Erlangung des akademischen Grades
Doktor der Naturwissenschaften
(Dr.rer.nat.)
der Mathematisch-Naturwissenschaftlichen Fakultät
der Christian-Albrechts-Universität zu Kiel

Alexander Hinz
Kiel
2018

1. Gutachter: Prof. Dr. Holger Kersten
 2. Gutachter: Prof. Dr. Franz Faupel
 3. Gutachter: Prof. Dr.-Ing. Peter Awakowicz
- Datum der mündlichen Prüfung: 13.07.2018

Erklärung

Ich versichere an Eides statt, dass diese Dissertation, außer der Beratung durch meine Betreuer, nach Inhalt und Form meine eigene Arbeit ist. Die Arbeiten Dritter habe ich entsprechend gekennzeichnet. Des Weiteren versichere ich, dass diese Arbeit weder in Gänze noch in Teilen im Rahmen eines Prüfungsverfahrens vorgelegen hat, veröffentlicht worden ist oder zur Veröffentlichung eingereicht wurde. Zudem versichere ich, dass die Arbeit unter Einhaltung der Regeln guter wissenschaftlicher Praxis der Deutschen Forschungsgemeinschaft entstanden ist.

Ort, Datum

Unterschrift

I would have written a shorter thesis, but I did not have the time.

free after Blaise Pascal

Kurzfassung

Diese Arbeit fasst Experimente, die im Rahmen des Sonderforschungsbereiches *TR24-Grundlagen komplexer Plasmen* erzielt wurden, zusammen.

Präziser ausgedrückt fasst diese Arbeit Experimente zusammen, deren Ziel die Untersuchung der Bildung von Nanopartikeln in reaktiven Plasmen und der Wechselwirkung der dispergierten Nanopartikel mit der Entladung war. Dazu wurde ein multidiagnostischer Ansatz verwendet.

Der multidiagnostische Ansatz machte die Entwicklung eines neuen Plasmareaktors notwendig. Trotz seiner kleinen Größe können am sogenannten 'Pequod'-Reaktor eine Reihe von verschiedenen Diagnostiken installiert werden.

Der untersuchte Entladungszyklus ist in drei Phasen (I-III) unterteilt worden. Das Sammeln von Nanopartikeln aus der Entladung hat gezeigt, dass sich schon 2 Sekunden nach Zündung der Entladung Nanopartikel gebildet haben. Die konventionelle orbit motion limit (OML)-Theorie wurde um die Schottky-Emission von heißen Nanopartikeln erweitert, um die Verzögerung der Aufladung bis zum Beginn der Phase II circa 9 s nach Zündung der Entladung zu erklären. Der Anstieg des Anregungsgrades während Phase II wurde als ein Anstieg der Elektronentemperatur T_e interpretiert, der den Abfall der freien Elektronendichte n_e überwiegt. Simulationen deuten daraufhin, dass Coulomb-Stöße die Elektronenstoßfrequenz für Impulsverlust ν_e^m beeinflussen können. Die Dynamik der Hochspannungsrandschicht an der getriebenen Elektrode deutet an, dass die mit Nanopartikeln gefüllte Entladung sich zumindest zum Teil wie eine elektronegative Entladung verhält. Während Phase III werden die Veränderungen, die während Phase II beobachtet wurden, umgekehrt. Es wurde spekuliert, dass dies durch eine Neuordnung des Nanopartikel-Ensembles und den Verlust von Nanopartikeln verursacht wird.

Das Wachstum der 1. Partikelgeneration kann in zwei Bereiche unterteilt werden. Das Wachstum großer Nanopartikel wird durch Oberflächenabscheidung dominiert, wohingegen das Wachstum kleinerer Nanopartikel durch einen anderen Mechanismus dominiert wird. Ein simples Modell basierend auf binärer Koaleszenz von Nanopartikeln wurde benutzt, um das Wachstum der kleinen Nanopartikel zu erklären.

Die Aussichten für den Einsatz von Kleinwinkel-Röntgenstreuung (SAXS) als Diagnostik wurden untersucht, indem Streuexperimente an eingeschlossenen Nanopartikel-Ensembles durchgeführt wurden. Bedauerlicherweise komplizierten experimentelle Probleme die Experimente am P03 Strahlrohr am DESY. Trotzdem suggerieren die ermittelten Ergebnisse, dass SAXS nicht die Methode der Wahl für die Untersuchung von dynamischen Systemen ist.

Abstract

This work summarises experiments that were performed in the framework of the *TR24-Grundlagen komplexer Plasmen*. Specifically, the experiments summarised in this work were aiming at investigating the process of nanoparticle formation in reactive plasmas and the interaction between the dispersed nanoparticles and the discharge with a multidagnostic approach.

The multidagnostic approach required the design of a new plasma reactor. Despite its small size, the so called 'Pequod'-reactor has several ports for the installation of various diagnostics.

The investigated discharge cycle has been subdivided into three phases (I-III). The collection of nanoparticles from the discharge revealed that nanoparticles have already formed 2 s after ignition of the discharge. The conventional orbit motion limit (OML)-theory has been extended by Schottky-emission from hot nanoparticles to explain the observed delay of the charging process until the onset of phase II approximately 9 s after ignition of the discharge. The increase of the degree of excitation during phase II has been interpreted as a rise of the electron temperature T_e that outweighs the drop of the free electron density n_e . Simulations suggest that Coulomb collisions can have an influence on the electron collision frequency for momentum loss ν_e^m . The dynamics of the high voltage sheath at the driven electrode indicate that the nanoparticle loaded discharge behaves at least partially like an electronegative discharge. During phase III the changes that were observed during phase II are reversed. It has been speculated that this is caused by a rearrangement of the nanoparticles ensemble and the loss of nanoparticles from the discharge.

The growth of the 1st nanoparticle generation can be subdivided into two regimes. The growth of large nanoparticles is dominated by surface deposition, whereas the growth of smaller nanoparticles is dominated by another mechanism. A simple binary coalescence model has been used to explain the growth of the small nanoparticles.

The prospects of small angle X-ray scattering (SAXS) as a diagnostic for the particle formation have been evaluated by performing scattering experiments on trapped nanoparticle ensembles. Unfortunately, several experimental problems complicated the experiments at the P03 beamline at the DESY synchrotron facility. Nevertheless, the obtained results suggest that SAXS is not the method of choice for investigating dynamic systems.

Contents

Kurzfassung	VII
Abstract	VIII
1 Introduction	1
2 Theoretical Background	3
2.1 Fundamental aspects of RF discharges	3
2.2 Formation of Nanoparticles in Reactive Plasmas	10
2.3 Charging of Nanoparticles in Plasmas	13
2.4 In-situ diagnostics	17
2.4.1 Impedance Probe	17
2.4.2 Optical Emission Spectroscopy	18
2.4.3 Mass Spectrometry	21
2.4.4 Multipole Resonance Probe	21
2.4.5 UV/Vis-transmission Spectroscopy	23
2.4.6 Small Angle X-ray Scattering	26
2.5 Ex-situ diagnostics	29
2.5.1 Scanning Electron Microscopy	29
2.5.2 Transmission Electron Microscopy	31
3 Experimental Setups	35
3.1 The 'Pequod'-Reactor	35
3.1.1 Reactor Vessel	35
3.1.2 Gas Supply and Vacuum System	37
3.1.3 Electrode System	40
3.2 Particle Collector Module	43
3.3 Discharge Diagnostics	45
3.3.1 Impedance Probe	45
3.3.2 Optical Emission Spectroscopy	45
3.3.3 Quadrupole Mass Spectrometer	45

3.3.4	Multipole Resonance Probe	46
3.3.5	UV/Vis-transmission Spectroscopy	46
3.3.6	Small Angle X-ray Scattering	47
3.4	Electron Microscopes	50
4	Results	51
4.1	Cyclic Behaviour of the Discharge	51
4.2	Investigation of the 1st Discharge Cycle	62
4.3	Onset of Particle Formation (Phase I)	67
4.3.1	Collection of Small Nanoparticles	67
4.3.2	Schottky-emission from hot nanoparticles	69
4.3.3	Detection of small nanoparticles	83
4.4	Electron Depletion (Phase II)	86
4.4.1	Increase of the Degree of Excitation	86
4.4.2	The Influence of Coulomb Collisions	93
4.4.3	Dynamics of the Sheath	102
4.5	Loss of Nanoparticles (Phase III)	109
4.6	Particle Formation in the 1st discharge cycle	114
4.7	SAXS Investigations of Particle Formation	123
5	Summary and Outlook	131
A		137
A.1	List of Acronyms	137
A.2	List of Mathematical Symbols	138
	Bibliography	143
	Acknowledgments	162
	List of Publications	163

Chapter 1

Introduction

Plasma. This fourth state of matter, describing a fully or partially ionized gas displaying collective behaviour, may appear as something very exotic. However, most of the visible matter in the universe is indeed in this state. The myriad of stars illuminating the sky at night as well as our very own sun are plasmas. But, unbeknownst to most humans a large variety of plasmas can be found on earth itself and play an important role in our modern world. Such plasmas include low pressure plasmas for the processing of semiconductors [1–3], atmospheric pressure plasma jets finding applications in the emerging field of plasma medicine [4–8], and high temperature plasmas in fusion reactors [9–11].

Even the most simple plasmas, for example an ensemble of electrons and ionized noble gas atoms, are complex systems in their own right. Nonetheless, at the beginning of the 1990's the field of complex plasmas emerged. The field of complex plasmas, often referred to as dusty plasmas, is dedicated to the investigation of phenomena arising from the interaction between plasmas and solid particles dispersed in them. In the 1990's a lot of the research in this field was driven by industrially relevant processes. Formation of particles in reactive plasmas used for the processing of semiconductors had been identified as a major source of wafer contamination [12–14]. Since then the field of complex plasmas has substantially broadened. Nowadays it is not only restricted to industrial process but also contributes, for example, to fundamental research in statistical physics [15–17]. Even fusion research can benefit from the insights gained by the research in the field of complex plasmas [18–20].

In principal, there are two routes for producing a complex plasma. The first route is the dispersion of externally produced particles in a plasma. This approach is often used to disperse a well defined amount of microparticles in a plasma to generate 2d or 3d plasma crystals [21–24]. The second route

uses reactive plasmas to generate the particles inside the plasma itself. The particle ensembles generated in this way have very high number densities so that they substantially alter the properties of the plasma in which they are dispersed. This second route is seen as a promising candidate for the production of nanoparticles. The properties of the nanoparticles can be tailored by adjusting the plasma parameters and the reactive atmosphere. Furthermore, charging of the nanoparticles inside the plasma prevents agglomeration and this production method is compatible with other plasma processes, for example the deposition of thin films with plasma enhanced chemical vapour deposition (PECVD). But, a trial and error approach for the optimization of such a process would certainly consume a lot of valuable resources. Thus, it will be advantageous to gain a detailed understanding of the complex interplay between the plasma and the particles dispersed in it before one attempts to develop an industrial process. A detailed understanding of the underlying physics will certainly not only benefit the field of complex plasmas but plasma physics as a whole.

The use of one or two diagnostics is insufficient to get a detailed understanding of these plasmas. Moreover, the results from different experiments can often not be directly compared because the behavior of complex plasmas is not only determined by the plasma parameters but also by the reactor in which the plasma is generated, i.e. via the gas flow. This work is, therefore, aiming at providing a versatile plasma reactor allowing for the installation of a variety of conventional and unconventional diagnostics, so that the data from different diagnostics is readily comparable. The formation of nanoparticles in a capacitively coupled high frequency discharge operated in an Ar – C₂H₂ atmosphere was chosen as a model system. These experiments are part of the effort of the *TR24-Grundlagen komplexer Plasmen* to investigate the fundamental processes in complex plasmas.

The remaining part of this work is structured as follows: chapter 2 provides the reader with a repetition of the basic aspects of the investigated system and the employed diagnostics. The 'Pequod'-reactor, designed and constructed as part of this work, as well as the diagnostics are described in chapter 3. The investigation of the particle formation and its influence on the discharge parameters is presented and discussed in chapter 4. It begins with a discussion of the cyclic formation of nanoparticles in the investigated discharge. This more general discussion is followed by a detailed investigation of the discharge's behaviour during the different phases of one cycle. The particle formation process itself is investigated in a separate subsection. In the end of chapter 4 the prospects of small angle x-ray scattering (SAXS) as a diagnostic are evaluated. The work is closed by a summary in chapter 5.

Chapter 2

Theoretical Background

2.1 Fundamental aspects of RF discharges

The study of RF discharges is a broad field not only because the parameter space for operating these discharges is large but also because RF discharges can be excited in many different ways [25–29]. The most well known excitation schemes are capacitive and inductive coupling. In order to avoid flooding the reader with superfluous information, the following paragraphs are not intended to be an exhaustive review but a pointed description of the fundamental aspects of RF discharges that are relevant for this work. For an exhaustive repetition the interested reader should resort to standard text books [30–32] or well known reviews [33, 34].

A typical laboratory RF discharge is operated with a driving frequency $f_{\text{RF}} = 13.56$ MHz in the pressure range of $1 \text{ Pa} \leq p \leq 100 \text{ Pa}$ and at RF-power levels of $5 \text{ W} \leq P_{\text{RF}} \leq 200 \text{ W}$. The choice of $f_{\text{RF}} = 13.56$ MHz is somewhat arbitrary. It is more or less just a compromise between an efficient power coupling into the discharge, which will be discussed later, the availability of frequencies for public use, and economics of scale. The frequency band that contains $f_{\text{RF}} = 13.56$ MHz is indeed open for public use and one can obtain a reasonably efficient power coupling into the discharge at this driving frequency. After manufacturers started to include RF generators and matching networks optimised for operating at this frequency in their product portfolios, $f_{\text{RF}} = 13.56$ MHz became an unofficial standard frequency for driving RF discharges. One can of course get generators and matching networks optimised for operation at other frequencies. For example, the 2nd harmonic at $f_{\text{RF}} = 27.12$ MHz is another popular driving frequency. But, most of the work on RF discharges has been performed at $f_{\text{RF}} = 13.56$ MHz, so that one has larger database for comparing and interpreting results if one

uses the same driving frequency.

Before the structure of RF discharges will be explained in detail, important basic concepts and fundamental plasma parameters will be introduced. But, even before that the difference between a plasma and a discharge will be explained. The term 'plasma' strictly only refers to a fully or partially ionised gas mixture that displays collective behaviour [32]. The term 'discharge' is more sloppily defined. It includes not only the plasma but also aspects that affect its behaviour and properties. For example, the sheaths surrounding the plasma can be seen as part of the discharge. Another example, which is relevant for this work, are nanoparticles that are dispersed in the plasma. The particles themselves are not part of the plasma but are part of the discharge. Another example is the excitation mechanism. Typically, one does not speak of DC plasmas or RF plasmas but of DC discharges and RF discharges. The excitation mechanism defines the properties of the plasma, but the excitation mechanism itself is not part of the plasma.

RF discharges operated at the conditions mentioned in the preceding paragraph belong to the class of low-pressure plasmas. They can also be classified as low-temperature plasmas or non-equilibrium plasmas. Whereas the classification as low-pressure plasma is quite intuitive, the classification as low-temperature or non-equilibrium plasma is more useful for describing one of the key features of RF discharges. This feature is the lack of thermal equilibrium between the electrons and the heavier species, i.e. ions and neutral atoms. Whereas the mean kinetic energy of the ions and neutral gas atoms is characterised by a temperature that is often above but still relatively close to room temperature, the mean kinetic energy of the electrons typically reaches a few eV in typical RF discharges. As will be shown later only the electrons take up energy efficiently from the RF fields driving the discharge. But, this alone does not explain why the electrons are not in thermal equilibrium with the heavier species. If they were an efficient energy transfer from the electron ensemble to the heavier species, they should reach thermal equilibrium. It is indeed the lack of an efficient energy transfer from the electron ensemble to the heavier species that results in the non-equilibrium conditions in the discharge. In a typical RF discharge the degree of ionisation is low, i.e. not larger than a few percent. Ion-electron collisions are relatively rare and do not contribute significantly to the energy transfer. The electrons primarily transfer their energy to the heavy neutral species by collisions. If one considers the elastic collisions it becomes clear why the energy transfer is so inefficient. In an elastic collision with a heavy neutral species an electron loses a relative amount of its kinetic energy $E_{\text{kin,e}}$ that is

given by

$$\frac{\Delta E_{\text{kin,e}}}{E_{\text{kin,e}}} = 1 - \left(\frac{m_e - m}{m_e + m} \right). \quad (2.1)$$

Because the mass m of the heavy species is much larger than the electron mass m_e . The term in brackets is close to 1 and the electron only transfers a tiny fraction of its kinetic energy in every collision. For example, an electron transfers less than $6 \times 10^{-3} \%$ of its kinetic energy in an elastic collision with an Ar atom. Just imagine a ping pong ball colliding with a bowling ball. An electron would need to collide very frequently with the heavy species before it has transferred a considerable amount of its kinetic energy. Additionally, one has to take into account that the electrons constantly take up energy from the RF fields. This imbalance between the energy transfer to the electron ensemble from the RF field and the energy transfer from the electron ensemble to the heavier species causes the non-equilibrium conditions in RF discharges.

Another important concept for RF discharges, like in all discharges, is the concept of quasineutrality of the plasma. Macroscopically the plasma is neutral. However, locally the quasineutrality can be violated. The length scale on which this condition can be violated is defined by the screening length of the plasma. As the screening of excess charges is described by a Debye-Hückel potential, also known as Yukawa potential, the screening length is commonly referred to as Debye length λ_D . On length scales larger than λ_D the free electrons and ions shield the perturbation of the quasineutrality. As both ions and electrons contribute to the screening the Debye length is given by

$$\frac{1}{\lambda_D^2} = \frac{1}{\lambda_{D,e}^2} + \frac{1}{\lambda_{D,i}^2} \quad (2.2)$$

The electron Debye length $\lambda_{D,e}$ and the ion Debye length $\lambda_{D,i}$ are given by

$$\lambda_{D,e} = \left(\frac{\epsilon_0 k_B T_e}{n_e e^2} \right)^{1/2} \quad (2.3)$$

and

$$\lambda_{D,i} = \left(\frac{\epsilon_0 k_B T_i}{n_i e^2} \right)^{1/2}, \quad (2.4)$$

respectively. Apart from the permittivity of free space ϵ_0 , the Boltzmann constant k_B , and the elementary charge e , the different Debye lengths are defined by properties of the electron and ion ensembles. The electron temperature T_e and the free electron electron density n_e define $\lambda_{D,e}$, whereas $\lambda_{D,i}$ is defined by the ion temperature T_i and the ion density n_i . The higher

the temperature of the electrons or ions is, the larger are their respective Debye lengths. As T_e is typically much larger than T_i in RF discharges, λ_D is dominated by the contribution from the ions $\lambda_D \approx \lambda_{D,i}$. A closely related concept is that of the plasma frequency. It defines the time scale on which the plasma can react to a perturbation. Like for the Debye length one can a plasma frequency for both the electrons and the ions. The electron plasma frequency $\omega_{p,e}$ is given by

$$\omega_{p,e} = \left(\frac{n_e e^2}{\epsilon_0 m_e} \right)^{1/2}. \quad (2.5)$$

With the ion mass m_i , the ion plasma frequency $\omega_{p,i}$ can be expressed as

$$\omega_{p,i} = \left(\frac{n_i e^2}{\epsilon_0 m_i} \right)^{1/2}. \quad (2.6)$$

As any ion mass is much larger than m_e , the ion plasma frequency is much lower than the electron plasma frequency. The driving frequency f_{RF} of RF discharges lies between both values. This means that the electrons can follow the RF field, whereas the ions are unable to follow the RF field. The ions are only affected by DC fields that develop in RF discharges.

The lower mass of the electrons, i.e. a higher mobility, compared to that of the ions result in a higher mobility of the electrons than the ions. This difference in the mobility of electrons and ions results in the formation of sheaths around the plasma. If an electrically floating wall is getting in contact with a plasma, ion and electron currents will flow to the wall. Because the electrons have a higher mobility the electron current exceeds the ion current. As a consequence the wall charges up negatively. A potential barrier builds up that reduces the electron current until ion and electron current are equal. The electrical potential of the wall has reached the so-called floating potential Φ_f . Close to the wall the free electron density n_e is lower than in the plasma bulk, because the electrons are repelled by the floating potential which is negative with respect to the potential Φ_p of the plasma bulk, the so-called plasma potential. The ion density n_i is also reduced in the vicinity of the wall, because they are accelerated to the wall by Φ_f . At some point n_e and n_i will start to deviate. This violation of the quasineutrality condition defines the thickness d_s of the sheath. The reader may now assume that the thickness of the sheath is given by $d_s \approx \lambda_D$. But, this is not the case. In the derivation of the Debye length it is assumed that the perturbation of the plasma is small compared to the thermal energy of the ions and electrons, i.e. $|e\Phi| \ll k_b T$. This assumption is violated in the case of the floating potential. In general,

it exceeds several volts. A better description of the sheath thickness is given by the Child-Langmuir law [35, 36]

$$j_i = \frac{4}{9} \epsilon_0 \left(\frac{2e}{m_i} \right)^{1/2} \frac{V_s^{3/2}}{d_s^2}, \quad (2.7)$$

which relates the ion current density j_i through the sheath with the voltage drop V_s across the sheath. Sheaths also form around grounded surfaces or surfaces with varying potential, like the electrodes of an RF discharge. The root cause for the formation of a sheath is always the same it ensures equal ion and electron currents through the surfaces. The sheath matches the parameters of the unperturbed plasma with the boundary conditions imposed by the surface in contact with the plasma. Thus, the sheath changes if the plasma parameters or the boundary conditions change. For example, the sheath in front of the driven electrodes of an RF discharge is not static but changes dynamically with the driving voltage. The dynamics of these sheaths are not described by the Child-Langmuir law, but it can be used to estimate the average thickness of the sheath. Models that describe the dynamics of the sheath of the driven electrode of capacitively coupled RF discharges have been developed by *Lieberman* [37, 38].

After having introduced the concept of the sheath, one can now develop an equivalent circuit model of an RF discharge. Because they are relevant for this work, a model for parallel-plate capacitively coupled RF discharges will be developed. A sketch of an idealised parallel-plate capacitively coupled RF discharge is depicted in figure 2.1. The discharge is formed between two

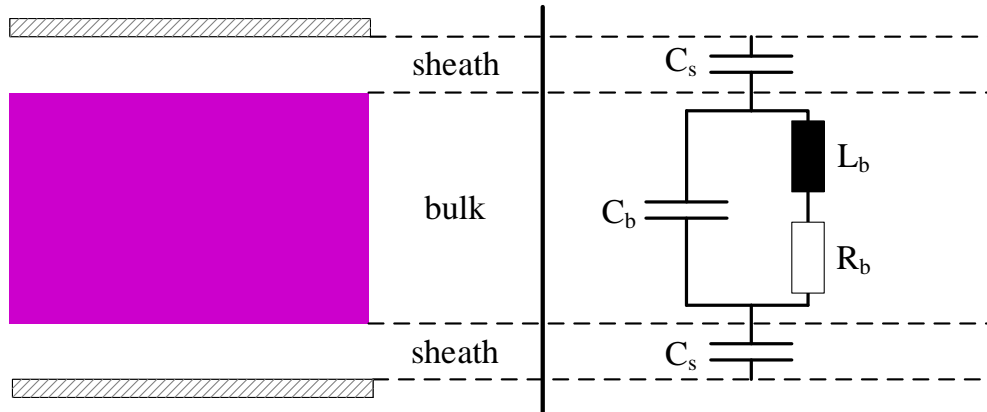


Figure 2.1: Sketch of an idealised parallel-plate capacitively coupled RF discharge and a simple equivalent circuit model.

parallel conducting plates. Either both plates are powered in a suitable way

by an RF generator or only one of the plates is powered. In that case the other plate is grounded. The discharge consists of three parts. Two sheaths in front of the plates and a plasma bulk between the sheaths. A simple equivalent circuit model of the discharge can also be found in figure 2.1. It is a series connection of three capacitors [32]. Each sheath is described by an ideal unfilled capacitor with Capacitance C_s . The plasma bulk is described by capacitor with capacitance C_b that is filled with a lossy medium, the plasma. The plasma is described as a series connection of an inductor with inductance L_b and a resistor with resistance R_b . The inductor models the inertia of the electrons and the resistor models the collision, primarily with neutrals species, of electrons. The resistivity ρ_b of the plasma bulk is given by [32]

$$\rho_b = \frac{m_e \nu_e^m}{n_e e^2} \quad (2.8)$$

The collisions are described by the electron collision frequency ν_e^m for momentum loss.

Depending on the size of the plates, or more generally speaking the electrodes, the parallel-plate discharges are symmetric or asymmetric. For a symmetric discharge the size of both electrodes has to be equal. If this is not the case the discharge will be asymmetric. If they have not been specifically designed for being symmetric, most parallel plate discharges will be asymmetric. Even if the electrodes have in principal the same area, most of these discharges will be asymmetric, because the plasma is in contact with other grounded surfaces. These surfaces can include grounded reactor walls or grounded shields around the electrodes. Thus, the area of the grounded plate is enlarged. Capacitively coupled asymmetric discharges develop a so-called self-bias voltage V_{SB} at the powered plate (cf. figure 2.2). In capacitively coupled discharges a capacitor blocks the current flow between the discharge and the RF generator. The net current flowing into the discharge must be zero over one RF cycle. Let us assume that, like in most systems, the area of the grounded electrode, is larger than the area of the powered electrode. Let us further assume that that the impedance Z_b of the plasma bulk vanishes. In that case the sheath capacitances act as capacitive voltage dividers for the RF voltage. The potential between the two capacitors is the plasma potential Φ_p . If the area of both electrodes is equal, the net current flowing into the discharge is always zero over one RF cycle. The currents passing through one electrode in the first half of the RF cycle pass through the other electrode in next half of the cycle. But, if the areas are unequal, this not the case. At the grounded electrode one has the following situation. The current density towards the grounded electrode is given by the voltage drop V_s across the sheath, i.e. Φ_p in this case. As long as Φ_p is positive the

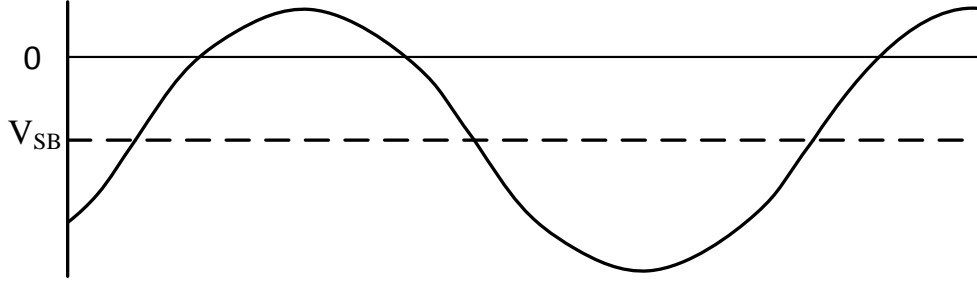


Figure 2.2: Illustration of the self-bias voltage V_{SB} . The boundary conditions of capacitively coupled asymmetric discharges result in the development of a large DC component, the self-bias voltage V_{SB} of the voltage at the powered plate, which is indicated by the solid curve.

sheath is intact and a net ion current flows to the grounded electrode. From the perspective of the grounded electrode this is the same situation as being connected to a voltage source through the sheath capacitance. From the perspective of the grounded electrode a net current flows through it as long as Φ_p is positive. To fulfill the condition of having a zero net current, Φ_p has to reach ground potential so that the sheath collapses and electrons can reach the grounded electrode to compensate the ion current, that has previously flown to the grounded electrode. Arguably this is also true for the symmetric case. But, in that case Φ_p is symmetric with respect to both electrodes. This is not true for the asymmetric case. Because the sheath capacitance is larger, V_s is smaller across the sheath in front of the grounded electrode. Thus, the oscillation of Φ_p is small. To compensate for the small oscillation amplitude that is insufficient to pull Φ_p to the ground potential, V_{SB} builds up. It basically shifts Φ_p to lower values until the oscillation amplitude of Φ_p , which is caused by the driving RF voltage, is large enough to pull Φ_p to the ground potential.

A larger the asymmetry, i.e. the difference between the areas of both electrodes, of the discharge results in a larger self-bias voltage. The large self-bias voltage results in the formation of a thick sheath at the powered electrode. Because the thick sheath has a low capacitance its impedance is much larger than the impedance of the sheath at the grounded electrode. Thus, the thin sheath at the grounded electrode is often neglected in equivalent circuit models of asymmetric discharges. Because the contribution from the capacitance C_b and the inductance L_b to the impedance of the plasma bulk are usually small in RF discharges, they are often also neglected. In that case capacitively coupled asymmetric RF discharges are described as a series

connection of a capacitor representing the sheath of the powered electrode and a resistor representing the plasma bulk.

Another important aspect of capacitively coupled RF discharges are the mechanisms that sustain the discharge. At low RF-power levels, the discharge operates in the so-called α -regime. In this regime the discharge is sustained by the so-called wave-riding mechanism. Because the resistance R_b of the plasma bulk is usually low in RF discharges, the voltage drop across the bulk is small and the electrons do not gain much energy in the bulk. Only electrons that are close to the sheaths of the plates, or, using a more general expression, electrodes gain large amounts of energy. The sheaths at the powered electrodes are expanding and contracting during one RF cycle. If electrons diffuse into the volume that is traversed by the expanding sheath, they are accelerated by the field inside the sheath. If they have gained enough energy from the sheath they can ionise neutral gas species in inelastic collisions. Therefore, ionisation, ore more generally excitation, predominantly takes place in the vicinity of the sheath edge. Thus, the highest emission intensity is also observed near the edge of the sheath (cf. figure 2.3). At higher RF-power levels the discharge operates in the γ -regime. In this regime the discharge is sustained by secondary electrons emitted from the electrodes. The secondary electrons are generated by ions that have been accelerated towards the electrode. At low RF-power levels the ions do not have enough energy to generate a significant amount of secondary electrons. Thus, the γ -regime is only observed at high RF-power levels. The same voltage drop across the sheath that accelerated the ions towards the electrode, also accelerates the secondary electrons. But, the electrons are accelerated away from the electrode into the plasma bulk. In the bulk the secondary electrons transfer their energy to neutral gas species. In the γ -regime a different emission pattern is observed. In addition to local maxima near the sheath edge, a global maximum of the emission intensity forms in the plasma bulk (cf. figure 2.3).

2.2 Formation of Nanoparticles in Reactive Plasmas

The formation of nanoparticles in reactive hydrocarbon and silane plasmas has been extensively studied since the 1980s. However, not all aspects of the formation process are well understood. Nevertheless, models that aim at describing the complete formation process have been developed. Especially, one of these models has evolved into some sort of standard model for describing

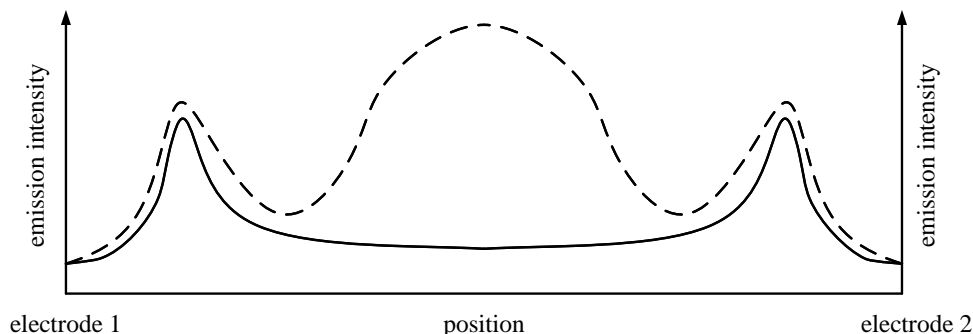


Figure 2.3: Sketch of the spatial distribution of the emission intensity of a symmetric capacitively coupled RF discharge. The solid curve corresponds to the α -regime and the dashed curve indicates the γ -regime.

the formation of nanoparticles in reactive hydrocarbon and silane plasmas. A well known description of this standard model by *Bouchoule et al.* is given in [39]. A more extensive review about the formation of nanoparticles in reactive plasmas can be found in the text by *Watanabe* [40]. According to this standard model, the formation process can be subdivided into three phases. An illustration of the formation process in a reactive hydrocarbon plasma and its subdivision into the three phases is depicted in figure 2.4.

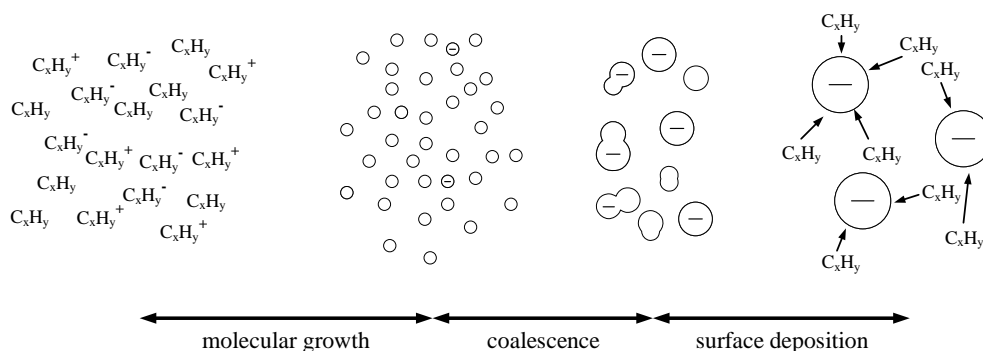
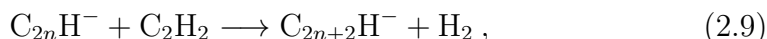


Figure 2.4: Sketch of the standard model of nanoparticle formation in a reactive hydrocarbon plasma.

The particle formation starts immediately after ignition. The precursor molecules are broken up into smaller fragments, radicals, and different positive and negative ions. At the same time these species are consumed

in reactions that produce larger molecules. One could call this mixture of different species the primordial soup of nanoparticle formation. For an excellent overview of the reactions that can take place in a reactive hydrocarbon plasma, the interested reader may resort to the work by *Boegarts et al.* [41–43]. Especially the formation of large negative ions, for example in reactions of the type



is considered as an important step in the formation of nanoparticles in reactive hydrocarbon plasmas. In contrast to neutral molecules these negative ions are retained in the plasma bulk by the electrical field inside the plasma bulk. They are not so efficiently trapped inside the bulk that it is impossible for them to leave the bulk, but their residence time in the bulk is longer. Thus, they can grow longer and it is more likely that they evolve into a small nanoparticle. The growth of the large negative ions by ion-molecular reactions, like the one mentioned above, stops as soon as the ions are neutralised. This molecular growth is the first phase of the particle formation process. It begins with a mixture of different molecular species and at its end a large number of small nanoparticles has formed. A specific feature of the formed nanoparticle ensemble is its quite narrow size distribution. This narrow size distribution is a result of the special growth conditions in a plasma. The particles charge up negatively in a plasma, because the electrons have a higher mobility than the positive ions (cf. subsection 2.3) However, the nanoparticles are still very small at this stage, i.e. at maximum a few nanometers. Thus, the majority of the particles is not permanently negatively charged, but uncharged on average. Nevertheless, also the on-average uncharged particles are very efficiently trapped in the plasma bulk. Because the charged particles drift much faster in the electrical field of the bulk than they diffuse as uncharged particles, they are trapped in the plasma bulk as long as they charge up negatively occasionally during their residence time. Because the rate at which the particle charge up negatively is size dependent the trapping efficiency is also size dependent. Very small particles do not charge up as often as larger particle. The small particles leave the plasma bulk at a higher rate. This selective trapping [39] narrows the size distribution.

The next phase of the formation process is defined by the agglomeration and coalescence of the nanoparticles. At this stage the nanoparticle number density n_p and the average particle diameter $\langle d_p \rangle$ have become large enough so that the nanoparticles start to agglomerate. But, they do not only agglomerate but also coalesce. If the particles only agglomerated it would be difficult to explain why the particles keep their spherical shape. One might expect that the agglomeration of the particles leads to a substantial broad-

ening of the size distribution, but this does not seem to be the case. The agglomeration process is self-limiting. As soon as the nanoparticles reach a certain size, they will acquire a permanent negative charge. As the negatively charged particles repel each other they cannot agglomerate anymore. They can only agglomerate with smaller uncharged particles. This limits the size to which the particles can grow by agglomeration and subsequent coalescence. As mentioned earlier the minimum particle size during this phase is limited by the selective trapping effect. In combination both effects keep the size distribution of the nanoparticles narrow. The growth of the nanoparticles, supposedly, also suppresses the formation of large quantities of small nanoparticles. Although their growth is dominated by agglomeration and coalescence, the particles also grow by surface deposition. They consume the molecules that would participate in the formation of new nanoparticles. Additionally, they reduce the free electron density n_e , when they charge up permanently. This should reduce the number of negative ions in the plasma.

The last phase of the formation process is dominated by surface deposition onto the nanoparticles. All particles are charged up negatively so that agglomeration and coalescence are not possible. The particles grow as long as they remain trapped in the discharge. Eventually, the particles are lost from the discharge because the forces pushing them out of the discharge have become so large that they can overcome the electrostatic force that retains the particles in the discharge.

The plasma, or more generally the discharge, is of course not unaffected by the formation of the nanoparticles, especially, if the formed nanoparticle ensemble is very large. The most drastic response of the discharge to the particle formation is the so-called $\alpha - \gamma'$ transition [39]. According to the standard model, it coincides with the coalescence phase of the particle formation process. As the particles charge up negatively, the free electron density n_e decreases. To compensate the loss of the electrons, which sustain the discharge, the electron temperature T_e increases. This is a manifestation of the self-balancing nature of plasmas. Because, n_e and T_e are fundamentally important parameters of the discharge, all other discharge parameters are expected to be affected by the $\alpha - \gamma'$ as well, either directly or indirectly.

2.3 Charging of Nanoparticles in Plasmas

The charging of nanoparticles in plasmas is still actively researched (cf. for example [44–47]) and no complete general theory has been developed, even if one restricts the theory to the charging of nanoparticles in low-temperature plasmas. The theory for charging of nanoparticle in low-temperature plasmas

with the highest acceptance is the so-called orbit motion limit (OML) theory. It uses the same concepts as the OML theory for plasma probes. A well written description of the OML theory for both particles and probes can be found in the book by [32]. The charged particle is described as a spherical capacitor. The inner electrode is formed by the charged particles, whereas the outer electrode is a virtual surface at a distance equal to the Debye-length λ_D of the plasma. In this configuration the charge Q_p of the particle is given by the product $C_p \Phi_f = Q_p$ of the capacitance C_p of the capacitor and the floating potential Φ_f of the particle. For convenience, the potential Φ_p of the plasma surrounding the particle was set to $\Phi_p = 0$. The capacitance is given by

$$C_p = 4\pi\epsilon_0 \frac{r_p \lambda_D}{\lambda_D - r_p}. \quad (2.10)$$

The permittivity of free space is denoted by ϵ_0 . By rearranging one gets

$$C_p = 4\pi\epsilon_0 r_p \left(\frac{\lambda_D^2 + r_p \lambda_D}{\lambda_D^2 - r_p^2} \right). \quad (2.11)$$

If the Debye-length is considerably larger than r_p one can simplify relation (2.11) to

$$C_p = 4\pi\epsilon_0 r_p \left(1 + \frac{r_p}{\lambda_D} \right). \quad (2.12)$$

by using the approximation $\lambda_D^2 - r_p^2 \approx \lambda_D^2$. Because the particle diameter d_p is primarily used for describing the particle size in this work, it is replacing r_p in the final expression of the particle charge

$$Q_p = 2\pi\epsilon_0 d_p \left(1 + \frac{d_p}{2\lambda_D} \right) \Phi_f. \quad (2.13)$$

Because the floating potential Φ_f of the particle cannot be measured directly, one has to express Φ_f as a function of parameters that are experimentally accessible. A suitable expression can be found if one considers the balance of currents to the particle. By definition the total current to the particle I must vanish ($I(\Phi)_{\Phi=\Phi_f} = 0$) if the potential Φ of the particle reaches Φ_f . This condition can be expressed as a balance

$$I_i = I_e \quad (2.14)$$

of the ion current I_i and the electron current I_e towards the particle. Initially, I_e is larger than I_i because the electrons have a higher mobility than the ions. The particle starts to charge up negatively; the potential of the particle is

negative. Thus, the incident electrons have to overcome a potential barrier to reach the particle. The electron current is given by [32]

$$I_e = \frac{en_e\pi d_p^2}{4} \left(\frac{k_B T_e}{2\pi m_e} \right)^{1/2} \exp\left(\frac{e\Phi}{k_B T_e} \right) \quad (2.15)$$

with the free electron density n_e , the electron temperature T_e , the Boltzmann-constant k_B , the mass of the free electron m_e , and the elementary charge e . In contrast to the electrons, the positively charged ions are attracted by the negatively charged particle. An uncharged particle would be hit by all ions that approach the ion with an impact parameter b smaller than the particle radius r_p . However, the negatively charged particle is hit by ions that approach the particle with impact parameters that are larger than r_p . This is illustrated in figure 2.5. All ions that approach the particle with

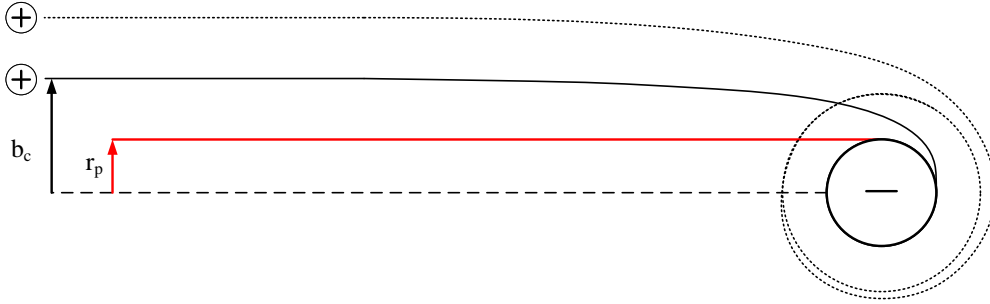


Figure 2.5: Illustration of the trajectory of ions approaching a negatively charged particle with radius r_p with impact parameters equal and larger than the collection radius b_c .

impact parameters smaller than the so called collection radius b_c hit the ion and contribute to I_i . The ion current is then given by [32]

$$I_i = \frac{en_e\pi d_p^2}{4} \left(\frac{k_B T_i}{2\pi m_i} \right)^{1/2} \left[1 - \frac{e\Phi}{k_B T_i} \right] \quad (2.16)$$

with the ion temperature T_i and the ion mass m_i . Ions with impact parameters larger than b_c can become trapped in a stable orbit around the particle. But they do not contribute to I_i unless they are knocked out of their stable orbit by a collision and collide with the particle. The contribution from those ions is not included in the simple version of the OML-theory described here. With the mass ratio $\mu = m_i/m_e$, the temperature ratio $\Gamma = T_e/T_i$, the

normalised floating potential $\eta_f = -e\Phi_f/(k_B T_e)$, and the relations (2.15) and (2.16) one can transform the current balance into a very elegant expression [32]

$$e^{-\eta_f} = (\mu\Gamma)^{-1/2}(1 + \Gamma\eta_f) . \quad (2.17)$$

for the η_f , and thus Φ_f . Equation (2.17) cannot be solved analytically, but it can be solved with standard numerical methods, given that all parameters are known or can be estimated. After the floating potential Φ_f , the particle charge Q_p can be calculated with equation (2.13). Interestingly the OML-theory predicts that Q_p increases linearly with the particle diameter d_p . The floating potential given by equation (2.17) is independent of the particle size and only depends on the parameters of the plasma in which the particle is immersed.

One limitation of the OML-theory described above is that it assumes that the charge up of the nanoparticles has no influence on the plasma. For a single isolated particle or a small number of particles that are well separated this assumption will be valid. But, in discharges that are loaded with a large number of nanoparticles this assumption is violated. The description of the charging process would not be self-consistent in this case. If a large number of electrons stick to the particles, the free electron density n_e will be reduced. Thus, the electron current towards the particles should decrease. To describe the charging of the nanoparticles self-consistently, the reduction of n_e has to be taken into account. If one used the OML-theory described above for discharges that are loaded with a large number of nanoparticles one would overestimate Q_p .

One obtains a better description of the charging of large nanoparticle ensembles if one includes the so-called Havnes effect. It describes the perturbation of the plasma by the charge up of the nanoparticle ensemble. The perturbation is described by a self-consistent change of the plasma potential of the perturbed part of the discharge. The perturbed potential Φ_c is sometimes named cloud potential [32]. The normalised cloud potential $\eta_c = -e\Phi_c/(k_B T_e)$ is defined in the same way as the normalised floating potential. The particle charge

$$Q_p = 2\pi\epsilon_0 d_p \left(1 + \frac{d_p}{2\lambda_D} \right) (\Phi_f - \Phi_c) . \quad (2.18)$$

is then defined by the difference between Φ_f and Φ_c . In addition to describing the perturbation of the plasma potential, an additional constraint on the particle charge Q_p is added. The quasineutrality condition of the plasma has also to be maintained in the nanoparticle loaded parts of the discharge. This condition is fulfilled if

$$en_i - en_e + Q_p = 0 \quad (2.19)$$

holds. It is assumed that the ions carry a single positive elementary charge and that Q_p is negative. With the quasineutrality condition and the current balance condition one obtains a set of two coupled equations that define η_f and η_c . Under the assumption of a fixed ion density n_i one obtains the following relations [32]

$$0 = e^{-\eta_c} - 1 + P(\eta_f - \eta_c) \quad (2.20)$$

$$0 = (\mu\Gamma)^{-1/2}[1 + \Gamma(\eta_f - \eta_c)] - e^{-\eta_f}. \quad (2.21)$$

The Havnes parameter P [48] is a measure of the discharge's perturbation by the nanoparticle ensemble. It can be interpreted as the number of particles in an electron Debye sphere [32] and can be expressed as

$$P = 2\pi\epsilon_0 d_p \frac{k_b T_e n_p}{e^2 n_e} \quad (2.22)$$

with the nanoparticle number density n_p . At a low Havnes parameter, i.e. $P \ll 1$, η_c vanishes and Q_p is equal to the value predicted by the simpler version of the OML theory. For larger Havnes parameters Q_p is lower than predicted by the simpler version of the OML theory.

2.4 In-situ diagnostics

2.4.1 Impedance Probe

Impedance or current-voltage probes are a commonly used discharge diagnostic. They are often found in industrial applications. After installation they are non-invasive and they can be directly integrated into the electrode system. Unlike other diagnostics like Langmuir probes or infrared absorption spectroscopy they do not require additional ports. Special care should be taken if an impedance probe is installed on a plasma reactor. If the probe is not perfectly matched to the system, it will most likely affect the power coupling into the discharge. Thus, results obtained before and after installation of the probe might not be directly comparable. In general, the impedance probe is installed in between the matching network and the driven electrode of the discharge (cf. figure 2.6). The probe itself contains two pick-up probes. In very simple impedance probes these pick-up probes would only measure the 1st harmonic of the RF-current and -voltage, respectively. In more advanced probes the current and voltage waveforms are measured. The probe electronics determine the contribution from each harmonic by Fourier transformation and thus provide not only information about the 1st

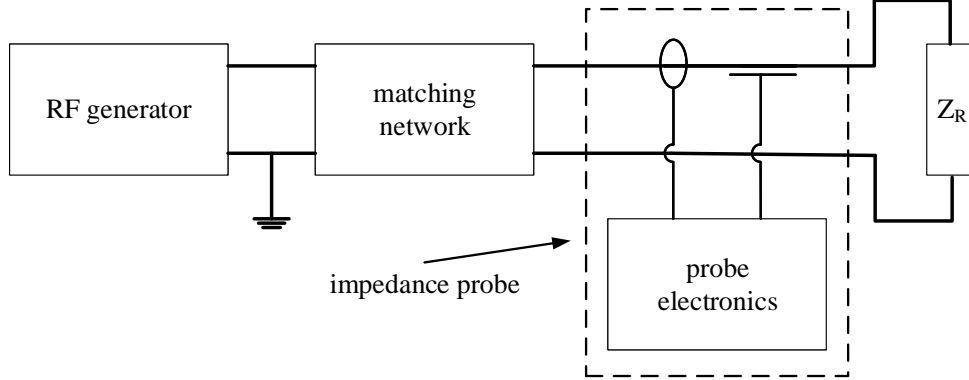


Figure 2.6: Sketch of the usual installation configuration of an impedance probe. The probe is placed in between the matching network and the driven electrode. Inside the impedance probe two pick-up probes measure the current and voltage waveform, respectively. The measured signals are processed inside the electronics of the probe.

but also the higher harmonics of the driving frequency. Commercial as well as self-constructed probes have been used [49–52]. Although operating these probes is relatively simple, the analysis of the information they provide is not as straightforward. The impedance probe can only provide information about the reactor impedance Z_R , which is basically the impedance downstream of the impedance probe. It contains not only contributions from the impedance of the discharge Z_d , which itself contains parasitic elements, but also contributions from the electrode and the transmission lines between the probe and the electrode. If one would like to correlate the measurements of the impedance probe directly with Z_d one has to perform calibration measurements develop a complete equivalent circuit for Z_R [53, 54]. But, even without this more advanced approach does the impedance probe provide useful information. Given that the contribution of the parasitic elements is more or less unaffected by changes of the discharge parameters, Z_R and Z_d should follow the same trends.

2.4.2 Optical Emission Spectroscopy

Optical emission spectroscopy (OES) is a well known plasma diagnostics that uses the light emitted from plasmas to acquire information about the properties of the plasma. Unless the neutral gas temperature T_n is very high, the emission spectra are line spectra. The emission lines correspond to the

radiative decay of metastable states. Low temperature plasmas, which are of interest for this work, have, in general, a low degree of ionisation. Therefore, the emission spectra are dominated by the emission associated with metastable states of neutral gas species. Because only the electrons have sufficient kinetic energy in low temperature plasmas, the neutral gas species are excited into their metastable states by electron impact excitation. Figure 2.7 illustrates possible paths for excitation and radiative decay of electron energy states in a neutral atom. Electron impact excitation can occur from

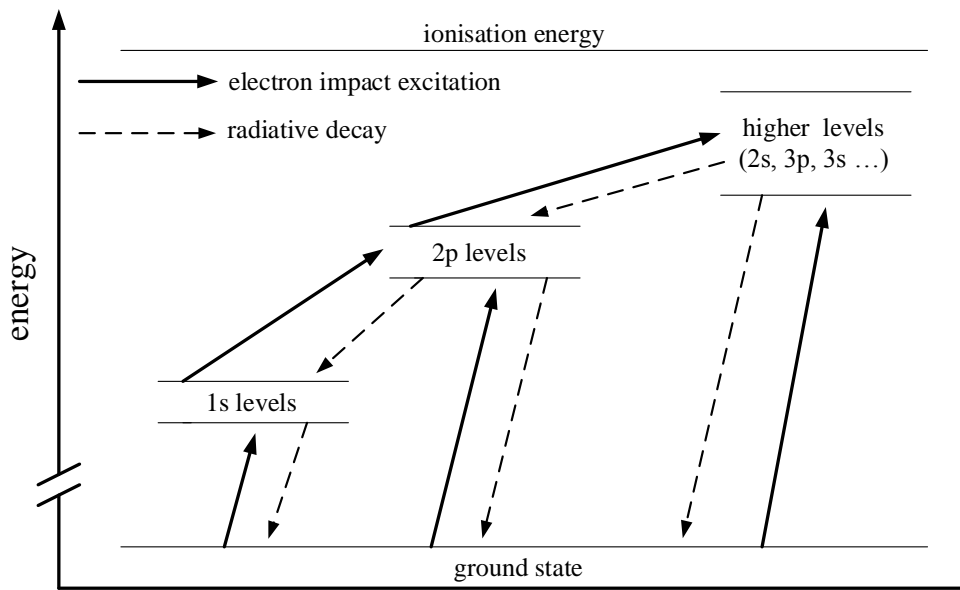


Figure 2.7: Illustration of possible paths for the excitation and radiative decay of electron energy states in a neutral atom. The energy levels of the different states are named after the Paschen notation.

the ground state or metastable states with lower energy. The same is true for the radiative decay of these states. Either the states decay into the ground state or cascade into lower lying metastable states. However, not all transitions that are in principle possible are equally important for emission spectroscopy. Some of the transitions are electric-dipole or spin forbidden and have far smaller transition rates than the transitions that are electric-dipole and spin allowed. These forbidden transitions are typically not of interest for optical emission spectroscopy, because their associated emission lines will be very weak compared to the emission lines corresponding to the

allowed transitions. Depopulation of the excited states by collisions with other species has not been taken into account in figure 2.7. In conjunction with the assumption that electron impact excitation is the dominant excitation mechanism, this is known as the so called corona model [55]. It is the most commonly used model for evaluating the emission spectra of low temperature plasmas.

One key advantage of OES is that it is absolutely non-invasive. Another advantage is its experimental simplicity. It only requires a spectrometer and optical access to the plasma. Unfortunately, there is no free lunch and an unambiguous interpretation of the emission spectra, especially a quantitative interpretation, is often challenging. Basically, one obtains two sets of information from the emission spectra. Firstly, one obtains the intensity and the position of the emission lines. This information can, for example, be used to determine the concentration of the different species in the plasma, cf. for example [56, 57]. However, for a quantitative analysis detailed information about the different excitation paths and the electron energy distribution function (EEDF) are required. It is also possible to infer information about the EEDF from this information by using more sophisticated approaches [58]. Secondly, one obtains information about the line shape of the emission lines. Especially the broadening of the emission lines contains valuable information about the plasma. For reliably extracting this information one needs spectrometers with very high resolution. Apart from the natural broadening of the lines, which is a consequence of the finite life time of the excited states, various other broadening effects contribute to the broadening of the emission lines. For example, the contribution from Doppler broadening could be used to estimate T_n [59], the contribution from Stark broadening could be used to estimate the electrical field strength [60]. One can of course combine both sets of information and compare simulated spectra with the recorded spectra, or at least the relevant parts of the spectra, to obtain information about the plasma [61]. Even if such a detailed analysis of the recorded emission spectra is unfeasible because the used spectrometer has an insufficient resolution or not enough a-priori information is available, OES can still be a very useful diagnostic, especially if it is used as part of a multidagnostic approach. An increase of the emission intensity indicates an increase of the degree of excitation of the plasma. In combination with the information provided by the other diagnostics this information could be used to identify the root cause for the increased degree of excitation. More thorough discussions of OES can be found in standard textbooks or reviews [55, 62].

2.4.3 Mass Spectrometry

Mass spectrometers are diagnostic tools that have been developed to analyse the composition of gases and vapourised liquids and solids. In general, each mass spectrometer consists of three parts. Firstly, an ion source in which the gases or vapours are ionised. Larger molecules, especially complex organic molecules, can dissociate into smaller fragments in the ion source. Secondly, an analyser into which the ionised species are transferred. In the analyser the ionised species are sorted according to their mass-to-charge ratio m/z . Thirdly a detector that records the amount of ionised species transmitted through the analyser at a specific m/z ratio. The detector signal, which is usually an ion current, is a measure for the concentration of the species with the corresponding m/z ratio. The different variants of mass spectrometers, like sector field mass spectrometers, quadrupole mass spectrometers, and time-of-flight mass spectrometers, that have been developed differ only in the construction of these three parts. Because a quadrupole mass spectrometer has been used in the experiments described in this work, only the operating principle of this type of mass spectrometer is briefly explained below. For more detailed information about the different types of mass spectrometers the reader is advised to refer to standard textbooks [63, 64].

The ion source of a typical quadrupole mass spectrometer uses electron impact ionisation. The electrons are generated by a heated filament accelerated inside the ion source. As the name suggests the analyser of the quadrupole is based on an electric quadrupole. More precisely the quadrupole consists of four rods that are connected to a high frequency generator as shown in figure 2.8. The ratio between the DC-voltage V_{DC} and the RF-voltage V_{RF} defines which species with a certain m/z -ratio can pass through the analyser. The ions drift through the analyser along its central axis. Additionally they are deflected by the quadrupole field in the analyser. The superposition of both motions result in a helical trajectory of the ions. However, only trajectories of ionised species with specific m/z -ratios are stable at a given voltage ratio. All other species move on unstable trajectories and will collide with the rods of the quadrupole analyser before they have passed through the analyser. The detector at the end of the analyser is usually a Faraday cup or some sort of electron multiplier.

2.4.4 Multipole Resonance Probe

The multipole resonance probe is a variety of active plasma resonance spectroscopy. It may also be referred to as plasma absorption probe. These probes have been recently criticised as being inferior to Langmuir probes,

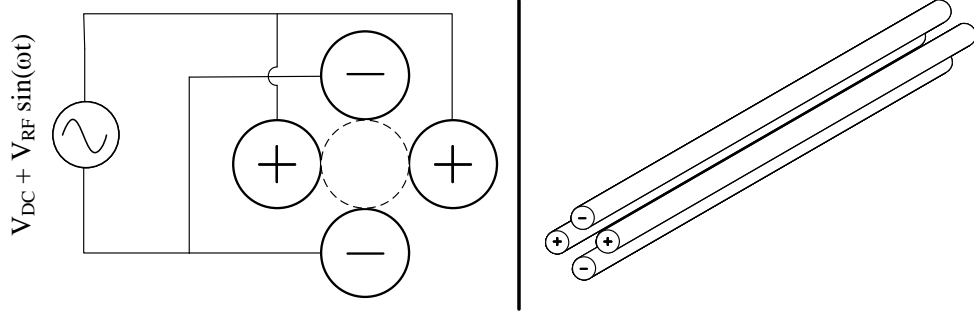


Figure 2.8: The sketch on the left-hand side shows a front view of the quadrupole analyser in a quadrupole mass spectrometer. The four rods are arranged around the central axis of the analyser and are connected to a high frequency generator. The sketch on the right-hand side shows an isometric projection of the rod system.

because of unrealistic assumptions in their underlying theories [65]. But, it has to be taken into account that the Langmuir probe has been developed almost a century ago [66] and has itself been the subject of intense research and a long development process. Therefore, one should not expect the MRP to have the same degree of maturity as the Langmuir probe. For an in-depth discussion of the MRP the reader should consult the original publications [67, 68]. A brief description of the operating principle of the probe is given below.

An MRP with a simple design can consist of two conducting hemispheres that are separated by a thin dielectric layer [68]. A dielectric shield surrounding the probe isolates it from the conducting plasma. Because the MRP is driven at high frequencies, it is unaffected by the dielectric shield and the deposition of insulating layers onto the probe. This is a major advantage compared to Langmuir probes and makes it, in general, very useful for analysing reactive plasmas, like the one investigated in this work. The two hemispheres form a spherical dipole antenna. The basic idea behind the MRP is to immerse the probe into the plasma and analyse the resonance spectrum of the MRP with a network analyser. If the MRP is driven close to the electron plasma frequency ω_{pe} , the position of the resonance peaks can be related to ω_{pe} and subsequently to the free electron density n_e . If the probe is driven symmetrically, the resonance spectrum can be described by the lumped element equivalent circuit model in figure 2.9 [67]. In the existing models for the MRP [67, 68] the relative permittivity $\epsilon_{r,p}$ of the

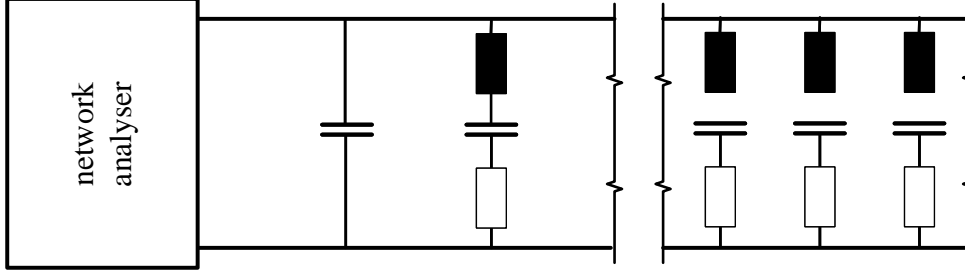


Figure 2.9: Lumped element equivalent circuit model of the MRP. It consists of an infinite number of series resonance circuits, which describe the multi-pole resonances of the probe, connected in parallel. The vacuum coupling is described by a capacitor connected in parallel to the resonance circuits. The resonance spectrum of the complete circuit is analysed with a network analyser.

plasma is modeled with the cold plasma approximation as

$$\epsilon_{r,p} = 1 - \frac{\omega_{p,e}^2}{\omega(\omega - i\nu_e^m)}. \quad (2.23)$$

The angular driving frequency of the probe is represented by ω . As momentum loss collisions are included in the cold plasma approximation, one can also obtain information about the electron collision frequency for momentum loss ν_e^m . The broadening of the resonance peaks is a measure for ν_e^m . At the moment a major limitation of the MRP is the size of the probe. Having a diameter of several millimeters it is substantially larger than Langmuir probes. This increases the invasive character of the MRP. But, this is simply an engineering and not a fundamental problem and will probably be solved in the future.

2.4.5 UV/Vis-transmission Spectroscopy

UV/Vis transmission spectroscopy is a well established technique in the field of materials science. For example, it has been used to investigate the optical properties of plasmonic absorbers [69] and metal-polymer nanocomposites [70, 71], and to determine the size of metallic nanoparticles [72–74]. The basic concept of UV/Vis transmission spectroscopy is illustrated in figure 2.10. An experimental setup for UV/Vis transmission spectroscopy is quite simple. It consists only of three parts: the specimen, a continuum light

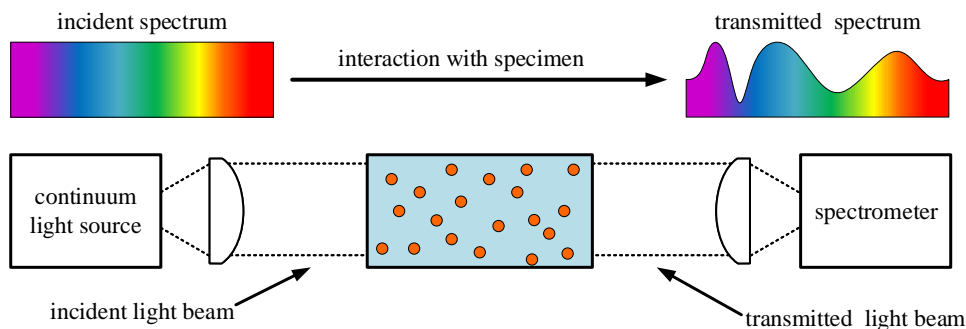


Figure 2.10: Illustration of the basic concept of UV/Vis transmission spectroscopy. A light beam emitted by a continuum light source, which covers the complete UV/Vis spectrum or only parts of it, is passed through the specimen. The transmitted light beam is analysed by a spectrometer to obtain the transmitted spectrum.

source, and a spectrometer. The specimen could be a colloidal solution in a cuvette, a thin film stack on a transparent substrate, or a discharge in a vacuum chamber with suitable windows. The light source in UV/Vis transmission spectroscopy setups is usually a broadband source that covers most the UV/Vis spectrum. However, for investigating certain specimens light sources with a limited wavelength range might be sufficient. A very common light source is a combination of a tungsten halogen lamp, which covers the visible part of the spectrum and a deuterium gas-discharge lamp, which covers the UV part of the spectrum. The light source can be combined with optics to control the size of the illuminated area and couple the light more efficiently into the spectrometer on the other side of the specimen. But, in principal the transmission spectroscopy setup could be operated without these optics. Admittedly, the setup would be very inefficient. Thus, by and large, UV/Vis transmission spectroscopy setups use collimation optics to couple the light of out of the source and into the spectrometer. The spectrometer only has to fulfill two prerequisites. Firstly, it has to be able to analyse the transmitted spectrum in the required wavelength range and range, and secondly its integration time needs to be low enough, if dynamic processes within the specimen are to be investigated. In general, the features in the transmitted spectra are relatively broad so that low-cost compact spectrometers can be used. This stands in contrast to the resolution required by spectrometers for the detailed analysis of optical emission spectra (cf. subsection 2.4.2), whose primary features are very sharp emission lines.

Depending on the investigated specimen there are different ways of interpreting the recorded spectra. The following discussion is restricted to the aspects that are relevant for this work. For more general information about the interpretation of UV/Vis transmission spectroscopy data the interested reader can, for example, refer to [75].

If nanoparticles dispersed in some matrix, i.e. an Ar – C₂H₂ discharge in this work, are to be investigated, one usually does not analyse the transmitted spectrum directly but the transmission spectrum. The transmission spectrum, i.e. the transmission T as a function of the wavelength λ ,

$$T(\lambda) = \frac{I_T(\lambda)}{I_0(\lambda)} \quad (2.24)$$

is obtained by dividing the transmitted spectrum $I_T(\lambda)$ by the incident spectrum $I_0(\lambda)$. The transmitted intensity

$$I_T = I_0 - I_E \quad (2.25)$$

can also be expressed as the difference between the incident intensity I_0 and the intensity I_E lost by extinction, i.e. the combination of absorption and scattering. Thus, one can rewrite (2.24) as

$$T(\lambda) = 1 - \frac{I_E(\lambda)}{I_0(\lambda)}. \quad (2.26)$$

The extinction within the specimen follows the Beer-Lambert law, given that multiple scattering can be neglected. The intensity lost by extinction is given by

$$I_E = I_0 (1 - \exp[-\tau]) . \quad (2.27)$$

The exponent in equation (2.27) is referred to as optical depth. It is a dimensionless number and is a measure for the extinction inside the specimen. For $\tau = 0$ the specimen is completely transparent, whereas it is completely opaque for $\tau = \infty$. If one removes the contribution of the matrix to the extinction by performing a reference measurement with a specimen that only consists of the matrix, the optical depth only contains the contribution from the nanoparticles and can be written as the product of the extinction cross section σ_{ext} and the line integrated nanoparticle number density n_p^{lin}

$$\tau = \sigma_{\text{ext}} n_p^{\text{lin}} . \quad (2.28)$$

By combining (2.26), (2.27) and (2.28) one obtains a compact expression for the transmission spectrum

$$T(\lambda) = \exp[-\tau] = \exp\left[-\sigma_{\text{ext}}(\lambda) n_p^{\text{lin}}\right] . \quad (2.29)$$

If the complex refractive index $n = n' - i n''$ of the nanoparticles is known one could calculate σ_{ext} , cf. for example [72] and the references therein. Because UV/Vis transmission spectroscopy is a line integrating technique it is not possible to determine the nanoparticle number density n_p from a single transmission spectrum without a-priori knowledge. If the spatial distribution of the nanoparticle number density $n_p(x)$ is known a-priori, one can use the formal definition

$$n_p^{\text{lin}} = \int_0^L dx n_p(x) \quad (2.30)$$

to fit (2.29) to the recorded transmission spectra and obtain information about $n_p(x)$. In the trivial case of $n_p(x) = \text{const.}$, n_p^{lin} is simply given by the product of n_p and the thickness L of the specimen along the path of the light beam. But, even if $n_p(x)$ itself is not known a-priori one can obtain information about the spatial distribution of the nanoparticles in the specimen with UV/Vis transmission spectroscopy. For, example if it is a-priori known that $n_p(x)$ is rotationally symmetric one could record several transmission spectra at different distances from the rotational symmetry axis of the specimen and use the Radon transform to reconstruct $n_p(x)$ from the transmission spectra. This approach can even be extended to 3d distributions [76].

2.4.6 Small Angle X-ray Scattering

In contrast to the other in-situ diagnostics reviewed so far, small angle X-ray scattering is not commonly used as a discharge diagnostic. A regular low temperature discharge would be almost completely transparent for the X-ray beam. However, if nanoparticles are dispersed inside the discharge, the situation is completely different. SAXS is a well established technique for investigating such colloidal systems [77–79]. It is also extensively used in the study of large biomolecules [80–82]

The interested reader can find a thorough analysis of SAXS in the book by *Feigin et al.* [83]. In the following only the basic concepts of SAXS, which are relevant for this work, are outlined. SAXS works in the same way as scattering of photons in the visible range of the electromagnetic spectrum. The incident electromagnetic waves excite the electrons of the specimen, which in turn emit electromagnetic waves of the same frequency. The major difference is the wavelength of the electromagnetic radiation. Typically SAXS experiments are performed with photon energies in the range of 7 keV to 16 keV. This corresponds to a wavelength range of 0.18 nm to 0.08 nm. Because the wavelength of the X-ray radiation is so small, SAXS can, in principal, be used to investigate very small structures, like freshly nucleated nanoparticles in a reactive plasma. In this case one can think of the individual nanoparticles

as small antennas. The superposition of the electromagnetic waves emitted from the excited electrons in the nanoparticle defines the directivity of the electromagnetic waves emitted from the nanoparticle. One can easily imagine that a spherical particle will emit electromagnetic waves with a different directivity than a cubic particle. Thus, the shape of the nanoparticles will affect the recorded scattering pattern. In addition, one usually does not investigate a system that contains only one isolated particle but a complete particle ensemble. The total scattering pattern is a superposition of the emission from each nanoparticle. Not only the shape of the nanoparticles but also their distribution will affect the scattering pattern. If the X-ray beam is transmitted through an isotropic specimen, i.e. a nanoparticle loaded low pressure discharge in this work, the scattering pattern is rotationally symmetric around the transmitted beam. Thus, the scattering pattern can be described by a 1d function $I_S(q)$. It is the intensity of the scattered light I_S , also referred to as scattering intensity, as a function of the scattering vector q . The scattering vector $q = |\vec{q}|$ is actually the length of the scattering vector, but to keep the notation simple it is simply called scattering vector.

If one performs a rigorous mathematical derivation (cf. [83]) one can obtain the following relation for the scattering intensity

$$I_S(q) = \langle N_p \rangle \langle F^2(\vec{q}) \rangle - K \langle N_p \rangle^2 \quad (2.31)$$

that includes the average number $\langle N_p \rangle$ of particles in the probed volume and the orientation averaged form factor $\langle F^2(\vec{q}) \rangle$ of the particles. As its name suggests the form factor describes the contribution of the particle shape to the scattering pattern. The variable K is not a simple factor but a rather complicated function that describes the effect of interparticle interference on the scattering pattern. For dilute systems the factor $K \langle N_p \rangle^2$ vanishes and the scattering pattern can be described as a linear superposition

$$I_S(q) = \langle N_p \rangle \langle F^2(\vec{q}) \rangle \quad (2.32)$$

of the scattering from $\langle N_p \rangle$ independent particles. This behaviour can be explained as follows. Only the phases of the electromagnetic waves emitted by particles that are in close proximity will have a well defined relationship. If the particles have the right distance to each other the emitted waves will interfere constructively or destructively resulting in an interference pattern. The nanoparticles emit at least partially coherent waves. However, if the separation of the nanoparticles is large, as in a dilute system, the phase difference between the emitted waves will be randomly distributed and no interference is observed. The emitted waves are incoherent. In that case the intensity of the emitted waves are added up instead of their amplitudes.

If one performs a Taylor series expansion around $q = 0$ and cuts the expansion after the 2nd term [83], the scattering intensity can be expressed as

$$I_S(q) = I_S(q)|_{q=0} \exp \left[-q^2 \frac{R_g^2}{3} \right]. \quad (2.33)$$

The scattering intensity is only a function of the scattering vector, the radius of gyration R_g , and the scattering intensity $I_S(q)|_{q=0}$ at $q = 0$. Equation (2.33) is the so-called Guinier approximation [83]. A convenient way of extracting R_g from the scattering pattern is to take the natural logarithm of equation (2.33)

$$\ln[I_S(q)] = \underbrace{\ln[I_S(q)|_{q=0}]}_Y - q^2 \underbrace{\frac{R_g^2}{3}}_s \quad (2.34)$$

and plot $\ln[I_S(q)]$ as a function of q^2 . This is the so-called Guinier plot. The radius of gyration is then given by the slope s of a straight line fitted to the data. The relations between the size of simple bodies and the radius of gyration are well known. The diameter

$$d_p = 2 \left(\frac{5}{3} \right)^{1/2} R_G \quad (2.35)$$

of a spherical particle is proportional to R_g . The y-intercept Y of the Guinier plot provides information about $I_S(q)|_{q=0}$. It is related to the electron density ρ_p^e inside the particle by

$$I_S(q)|_{q=0} = \left| \int_V dV \rho_p^e \right|^2. \quad (2.36)$$

For particles of simple shape one can solve the integral in (2.36) analytically. For a spherical particle with diameter d_p one obtains

$$I_S(q)|_{q=0} = \frac{\pi^2}{36} \rho_p^{e2} d_p^6. \quad (2.37)$$

The y-intercept in the Guinier plot also contains information about d_p , but one would need to know ρ_p^e to determine d_p . Moreover, $I_S(q)|_{q=0}$ can, in general, not be measured because this part of the scattering pattern is blocked by a beamstop to avoid damage to the detector by the intense direct beam. To obtain $I_S(q)|_{q=0}$, one would need to extrapolate the data by fitting a straight line to it. At that point d_p could already be obtained from the slope of the fit. Nevertheless, equation (2.37) is useful because it shows that the scattering intensity depends strongly on the particle size. If d_p is reduced

by a factor 10 the maximum scattering intensity decreases by a factor 10^6 . This is one of the reasons why SAXS measurements are primarily performed at synchrotron sources. It is possible to perform SAXS measurements with laboratory sources, but the required integration times are typically too long to study dynamic processes.

2.5 Ex-situ diagnostics

2.5.1 Scanning Electron Microscopy

Scanning electron microscopy (SEM) is one of the most versatile and commonly used techniques for studying the nano- and microstructure of materials. The construction of a scanning electron microscope is similar to a cathode ray tube. Electrons are generated by thermionic or field emission sources and accelerated towards the specimen. Typical acceleration voltages are of the order of 10s of kV. On their way to the specimen the electrons pass through an optical column in which electromagnetic lenses focus the electron beam to sizes down to a few nanometers. The optical column also contains the deflection system for scanning the electron beam across the specimen surface. As the electron source, the optical column, and the specimen chamber are evacuated the majority of electrons reach the specimen without being scattered. SEM images are generated by scanning the electron beam across the specimen surface and recording the intensity of different signals, i.e. photons and electrons of different energy, originating from various interactions between the incident electrons, which are referred to as primary electrons, and the specimen. It is the large variety of different signals that can be recorded by the SEM that make it such a versatile technique. Each signal can be used to generate images with different contrasts. For detailed discussions of the SEM-technique the interested reader may consult standard text books [84, 85]. A short discussion of the most important electron-specimen interactions and the associated contrasts will be given below.

An important concept for the discussion of the various electron-specimen interactions is the so called interaction volume. It is the volume in which the electrons interact with the specimen and from which information in the form of electrons or photons can escape from the specimen. A sketch of a typical interaction volume is depicted in figure 2.11. The size of the interaction volume, or more precisely the volume from which the information used for generating the contrast escapes, defines the spatial resolution. Unlike in optical microscopy the spatial resolution is not limited by the wavelength of the electrons and is much higher than in optical microscopes. Features below

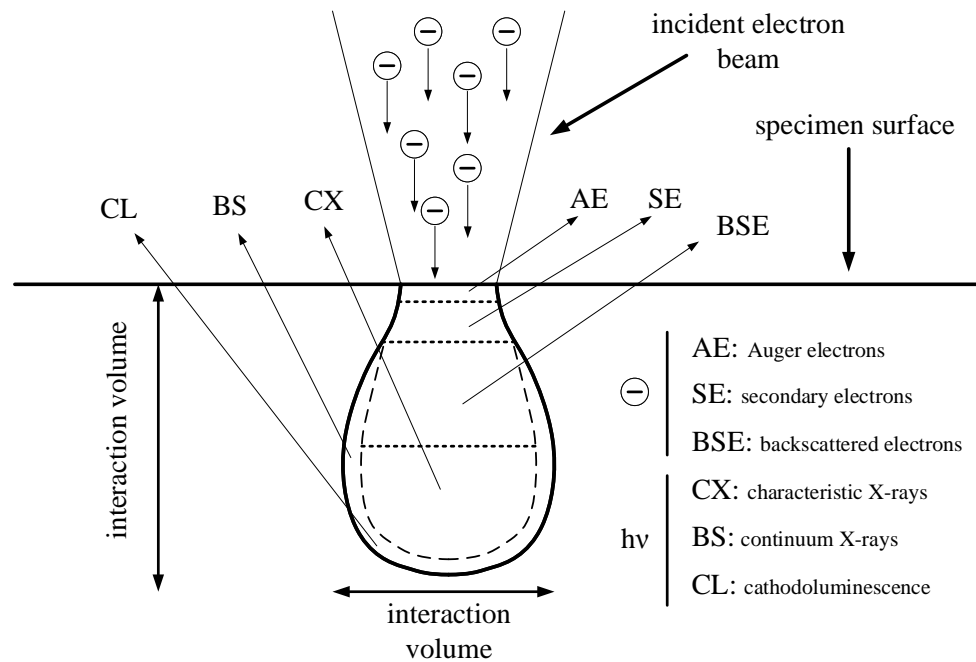


Figure 2.11: Sketch of a typical interaction volume describing the interaction between a specimen and an incident beam of high energy electrons.

10 nm can be resolved with state of the art SEMs.

The signal with the highest surface sensitivity originates from Auger electrons. The mean free path of the Auger electrons is small so that only Auger electrons generated close to the specimen surface can escape and can be analysed with a suitable detector. Another signal with high surface sensitivity originates from secondary electrons. The energy of the secondary electrons is low, i.e. less than 50 eV, and so is their mean free path. They are primarily created by inelastic interactions between the primary electrons and the specimen. But, a certain proportion of the secondary electrons are generated by inelastic interactions between backscattered electrons and the specimen. The contrast of SEM images recorded with the secondary electron signal is dominated by the topography of the specimen surface. If surfaces are inclined to the primary electron beam, the interaction volume is enlarged compared to normal incidence so that these inclined surfaces appear brighter in the images. But, the secondary electrons also provide some contrast related to the chemical composition of the specimen, because the secondary electron yield is a material dependent quantity. However, by and large stronger contrast between areas with different chemical composition can be obtained with the

backscattered electron signal. Backscattered electrons are primary electrons that have been scattered multiple times so that they leave the specimen. Because the electrons are more or less scattered elastically by Rutherford scattering the energy of the backscattered electrons lies in the keV range and their mean free path is larger than that of secondary electrons. As the deflection of the electrons by Rutherford scattering depends on the atomic number of the cores by which they are scattered, the backscattered electron yield is sensitive to the chemical composition of the specimen. Nevertheless backscattered electrons do also provide contrast related to the topography of the specimen.

In addition to electrons that escape from the specimen, photons that escape from the specimen can also be used to generate SEM images. Characteristic X-rays emitted from the specimen can be analysed with a spectrometer to create composition maps of the specimen. This is referred to as energy dispersive X-ray spectroscopy (EDX). Unlike the composition contrast provided by the aforementioned electron signals, EDX can be used to obtain absolute concentrations of the elements in the specimen. Because the characteristic X-rays can escape from a large part of the interaction volume the spatial resolution is lower compared to the electron based signals. Moreover, in general EDX does not provide information about the topography of the specimen. In the case of non-metallic specimens one can also record the cathodoluminescence from the specimen. The cathodoluminescence is not caused directly by the primary electrons as their kinetic energy is far too high. It is caused by the low energy secondary electrons generated in the interaction volume.

2.5.2 Transmission Electron Microscopy

Transmission electron microscopy is another very versatile technique that uses various interactions between high energy electrons and a specimen to gain information about the specimen. State of the art TEMs can achieve atomic resolution. TEMs are similar in design to SEMs but there are certain differences between the two microscope types. The optical column of a TEM is more complex and contains more lenses for focusing and collimating the electron beam and for correcting different aberrations. Moreover, the specimen is placed at a different position inside the microscope. Whereas it is placed in special specimen chamber at the end of the optical column in an SEM, it is placed inside the optical column of a TEM. As the name of the technique suggests the electrons are transmitted through the specimen in a TEM. In principal a TEM does not need a deflection system like an SEM, but many TEMs are nowadays equipped with deflection systems. The TEM is then operated as a scanning transmission electron microscope (STEM). This

increases the versatility of the TEM-technique. The interested reader may once more refer to standard textbooks for a more detailed discussion of the TEM-technique [86, 87]. Electron-specimen interactions that are relevant for this work are shortly discussed below.

In the so called bright-field imaging mode the specimen is illuminated by a collimated electron beam. Some of the high energy electrons are elastically scattered by the specimen and are deflected. These deflected electrons are blocked by an aperture placed behind the specimen. Only undeflected electrons can pass through the aperture and reach the 2d detector at the end of the optical column. Areas of the specimen in which a larger amount of electrons is deflected appear darker in the recorded TEM images. Because the amount of electrons that are deflected is defined by the product ρd of the specimen density ρ and the specimen thickness d , this contrast is referred to as mass-thickness contrast. Thus, this contrast is not only sensitive to the composition of the specimen but also to its thickness. The contribution of the specimen thickness has to be taken into account if the specimen has a non uniform thickness. This is of special importance if one does not investigate closed films but structures with non-uniform thickness, for example nanoparticles. This is illustrated in figure 2.12. For the incident electron beam the

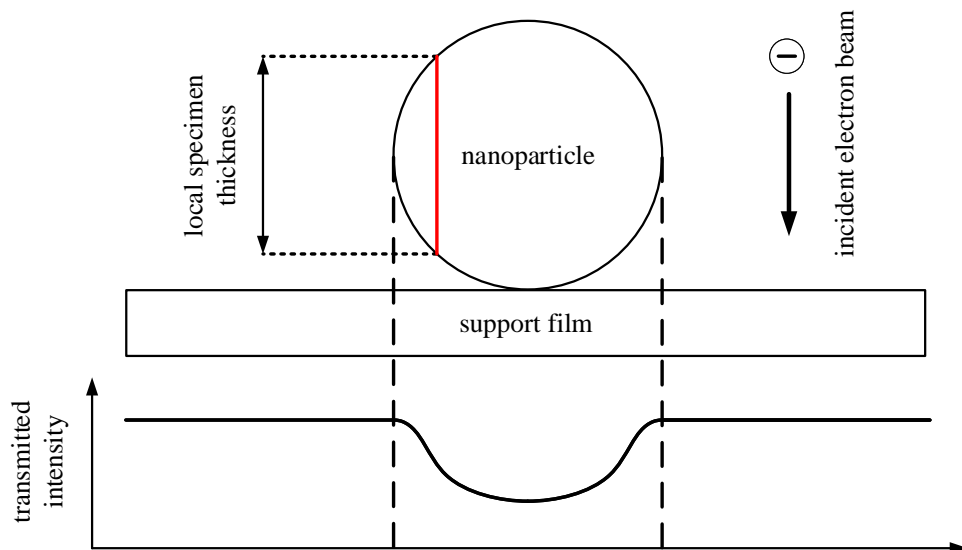


Figure 2.12: Illustration of the mass-thickness contrast of a spherical nanoparticle on a support film. The sketch shows a cut through the nanoparticle and the support film.

thickness of the specimen, a nanoparticle in this case, is non-uniform. More

electrons passing through the particle close to the central axis of the particle are deflected than electrons passing through the particle close to the 'edge' of the particle. Thus it may appear that the particle has an inhomogeneous density, i.e. composition. If the image is not properly focused it may even appear that the particle is a core-shell particle. Even if it is known that the particle has a homogeneous composition the weak contrast at the 'edge' of the particle can be problematic. It may result in an underestimation of the particle size. This effect is exacerbated if the particle diameter is comparable to the thickness of the support film and the density of the particle is comparable to that of the support film. In that case the contrast between the particle 'edge' and the support film will be especially low. Such a weak contrast has, for example, to be expected for small carbonaceous nanoparticles deposited on amorphous carbon support films, which are studied in this work.

Like in an SEM one can combine TEM with spectroscopic methods to obtain information about the composition of the specimen. In contrast to the bright-field imaging mode these imaging modes are based on inelastic interactions between the incident electrons and the specimen. In principal these spectroscopic imaging modes could be used with conventional illumination conditions, i.e. a collimated electron beam with a relatively large diameter. But, in general the spectroscopic imaging modes are used in conjunction with STEM to generate composition maps or probe the composition of the specimen locally. If a collimated beam were used, one would obtain information about the average composition of the specimen. The focused electron beam used in STEM provides a high spatial resolution. The most commonly used spectroscopic methods are EDX and electron energy loss spectroscopy (EELS). The EDX works in the same way as in an SEM; characteristic X-rays emitted from the specimen are analysed by a suitable detector. In a sense EELS is complementary to EDX. Instead of analysing the characteristic X-rays generated in inelastic interactions between the electrons and the specimens, EELS analyses the energy loss of the transmitted electrons. But, EELS spectra contain additional information. For example, they also contain information about plasmon losses of the transmitted electrons.

Chapter 3

Experimental Setups

3.1 The 'Pequod'-Reactor

3.1.1 Reactor Vessel

The main design objective of the 'Pequod'-reactor was to combine a highly mobile reactor that can accommodate a variety of conventional and unconventional plasma diagnostics. An image of the reactor can be seen in figure 3.1. The plasma reactor itself is based on a stainless steel cylinder with an inner diameter of 200 mm and an inner height of 160 mm. The reactor is large enough so that a multitude of different ports can be attached to it. Yet, it is still so small that it can be easily transported to other research facilities. Most importantly, it is small enough so that it can be installed at the P03-beamline [88] of the PETRA III synchrotron at the DESY research facility.

In total, there are 16 ports available on 'Pequod'-reactor to install vacuum equipment, plasma diagnostics, electrodes, and auxiliary components. Figure 3.2 shows crosssections through the 'Pequod'-reactor along one of its symmetry planes. Most ports of the reactor are aligned onto the centre point of the reactor (CP). Only the four CF40 ports located at the bottom of the reactor are aligned onto the secondary alignment point (PP). It is located approximately 32 mm above CP on the rotational symmetry axis (R-axis) of the cylindrical reactor. The decision for this particular arrangement was a compromise between manufacturability and the spatial restrictions imposed by the heavy-load goniometer available at the P03-beamline. These four ports are intended to be used for the pumping system of the reactor. One must expect that the neutral drag force resulting from the gas stream between the gas inlet and the pump ports of the reactor influences the distribution of the nanoparticles dispersed inside the discharge and in worst case might

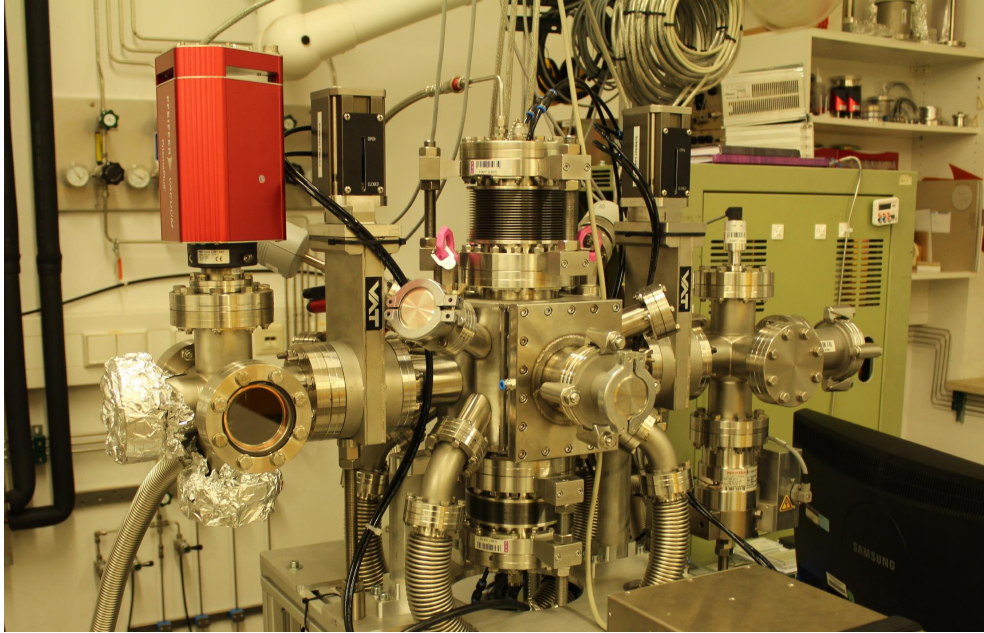


Figure 3.1: Image of the 'Pequod'-reactor.

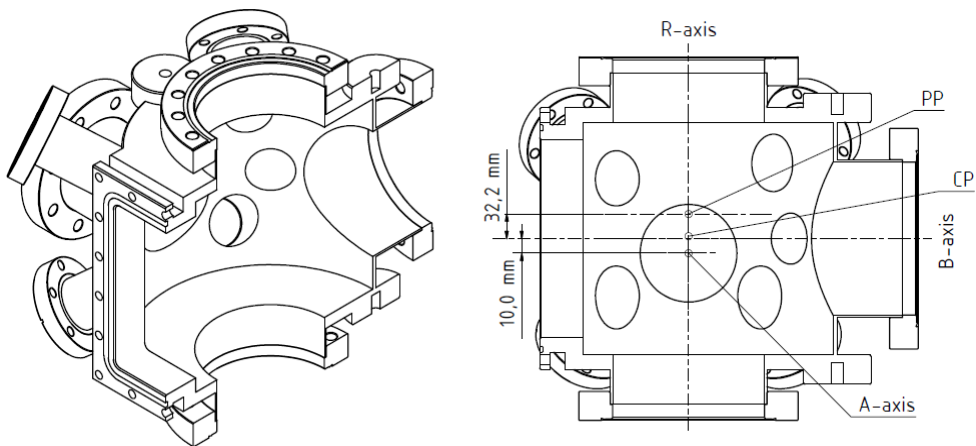


Figure 3.2: 3d and 2d crosssections of the 'Pequod'-reactor. The positions of the centre Point (CP), the secondary alignment point (PP), the rotational symmetry axis (R-axis), the beam axis (B-axis), and the auxiliary axis (A-axis) are indicated.

result in an inhomogeneous distribution of the particles. Thus, it would be favourable if the gas stream was rotationally symmetric. The Gaseous Electronics Conference (GEC) Reference Cell solves this problem by using a gas inlet located on the rotational symmetry axis of the cell in combination with an annular gap on the bottom of the cell that has four CF 40 ports equally distributed along its circumference. [89]. Due to the spatial restrictions imposed by the heavy-load goniometer this solution could not be transferred to the 'Pequod'-reactor. The four CF40 pump ports are instead directly connected to the bottom of the reactor and are not equally distributed along its circumference but at angles of 120 deg and 60 deg, respectively. However, the gas inlet is located on the rotational symmetry axis of the reactor. The only other ports that are not aligned onto the center point are the two CF63 ports defining the auxiliary axis (A-axis). It lies perpendicular to the beam axis (B-axis) and intersects the R-axis 10 mm below CP.

Another uncommon feature of the 'Pequod'-reactor is the large rectangular vacuum port that is defining the B-axis together with a CF100 port on the backside of the reactor. In fact, the 'Pequod'-reactor is not a perfect cylinder. The rectangular port intersects the cylinder at a distance of approximately 73 mm from the centre point and forms a flat face. The rectangular port has an open width of 100 mm and an open height of 136 mm. It is sealed by a fluoropolymer O-ring. Such a large rectangular port was incorporated into the design to allow for the installation of a large rectangular Kapton®-window for grazing-incidence small-angle X-ray scattering experiments. Compared to circular windows with the same area, rectangular windows provide a more efficient coverage of the rectangular X-ray detectors, provided that nothing else, i.e. a flight tube, limits the detector area that can be covered. For all other diagnostics that are the subject of this work a CF100 window had been sufficient.

Figure 3.3 shows a crosssection through the 'Pequod'-reactor at the height of the centre point. The positions at which the particle collection system and the majority of the discharge diagnostics have been attached to the reactor are also indicated in figure 3.3. A detailed description of the particle collection system and the discharge diagnostics will be given in section 3.2 and 3.3, respectively.

3.1.2 Gas Supply and Vacuum System

A schematic drawing of the reactor's (P) vacuum and gas supply system is shown in figure 3.4. It also includes, for the sake of completeness, the vacuum systems of the massspectrometer (M) and collector (C) module. All three systems are connected to the same multistage roots pump (ACP 15, Pfeiffer

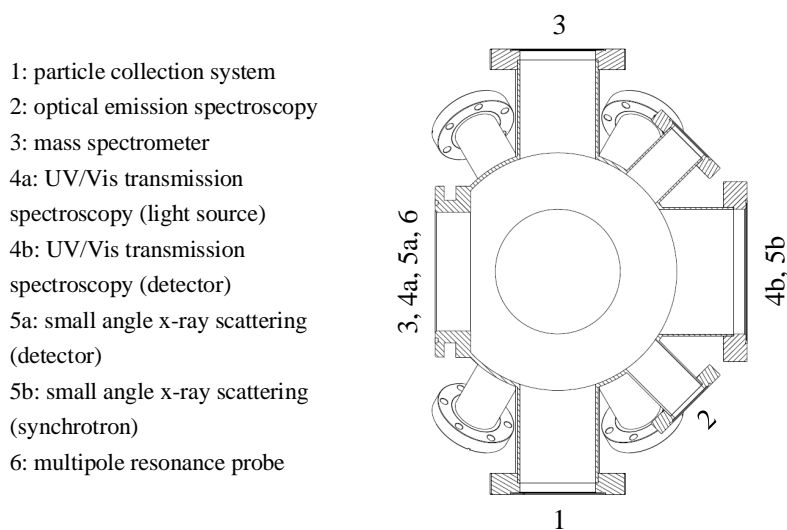


Figure 3.3: 2d crosssection through the 'Pequod'-reactor at the height of the centre point. The positions at which the particle collection system and the majority of the discharge diagnostics have been attached are indicated by labels at the corresponding ports.

Vacuum). To prevent the agglomeration of particles inside the pump and to dilute the waste gas from the reactor, the foreline pump is purged with 10 slm nitrogen (purity 99,999 %) during process runs. The high vacuum in the 'Pequod'-reactor is generated by a turbomolecular pump (HiPace® 60P, Pfeiffer Vacuum). This particular pump has a higher resilience against contamination by particles because it lacks a Holweck-stage. Therefore, it is a true turbomolecular pump and does not belong to the class of turbodrag pumps, which are more common nowadays because they can reach lower base pressures. Like the foreline pump, the turbopump is purged with approximately 9 sccm nitrogen. Another gas inlet at the turbopump allows to vent the complete system with nitrogen. For both purposes nitrogen with a purity of 99,999 % is used. With its current vacuum system the 'Pequod'-reactor is able to reach an ultimate pressure of $p_u \approx 3 \times 10^{-4}$ Pa. During a process run the base pressure p_b in the reactor is limited to $p_b \approx 2 \times 10^{-2}$ Pa by increased backstreaming resulting from the purging of the pumps. The base und ultimate pressure of the reactor are measured by a full-range cold cathode gauge (PKR270, Pfeiffer Vacuum). To minimize contamination of the gauge, it is switched off during the process runs. The process pressure inside the reactor is monitored by three different gauges. Two of them are capacitive gauges (CMR 364, Pfeiffer Vacuum & 626B Baratron®, MKS Instruments). The

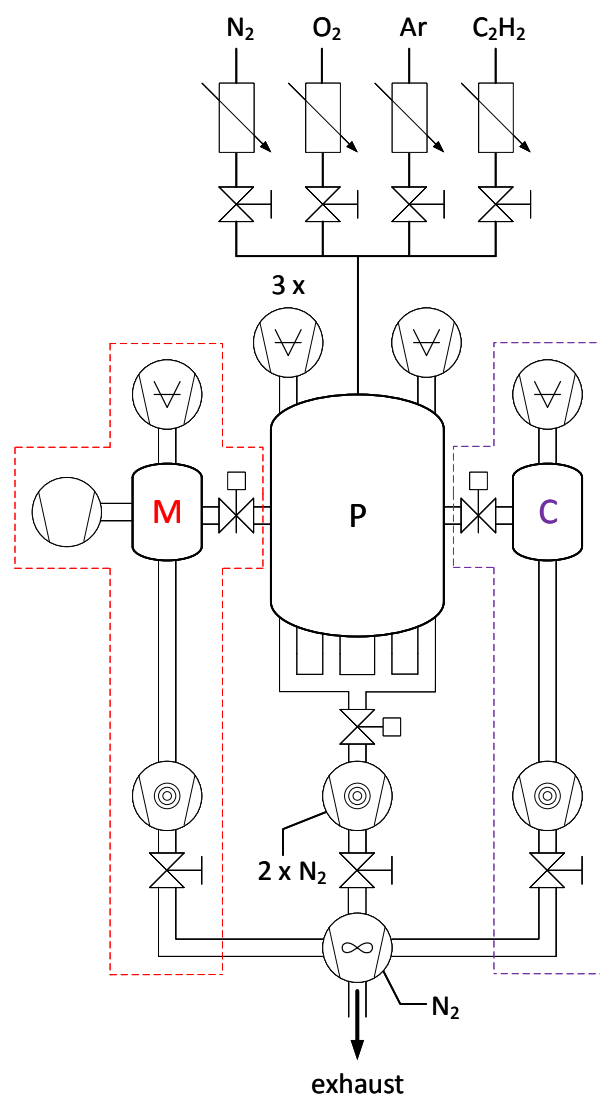


Figure 3.4: Schematic drawing of the vacuum and gas supply system of the 'Pequod'-reactor (P). The vacuum systems of the collector module (C) and the mass spectrometer module (M) are also included.

Baratron® is connected to a butterfly valve (253B, *MKS Instruments*) in front of the turbopump forming a closed control loop, which is used to keep the absolute process pressure in the reactor constant during a process run. In addition, the process pressure is monitored by a Pirani gauge (TPR 280, *Pfeiffer Vacuum*). In its current configuration four gases (N_2 , O_2 , Ar, and C_2H_2) can be simultaneously admitted into the 'Pequod'-reactor. The mass flow of each gas into the reactor is controlled by a mass flow controller (MF 1, *MKS Instruments* for N_2 , O_2 , and Ar & MCV, *Alicat* for C_2H_2). Additional shut-off valves between the reactor and the flow controllers block the residual gas flow from the reactors into the reactor if they are not in use. All gas lines in the gas supply system of the reactor are made from stainless steel. All connections in the gas supply system are either stainless steel compression fittings (Swagelok®, *Swagelok*), fittings with stainless steel gasket face seals (VCR®, *Swagelok*), or fast couplings (QC4, *Swagelok*).

3.1.3 Electrode System

The planar cylindrical electrodes and the gas inlet system can be installed on the two CF100 ports lying on the rotational symmetry axis of the reactor. The two installation configurations are depicted in figure 3.5. In the single-electrode configuration only the bottom electrode is mounted. The process gases are injected into the reactor trough a showerhead-type gas inlet. It is a hollow stainless steel disk with an outer diameter of 70 mm. The gas exits the showerhead through holes on its front face. The holes are arranged in a square pattern. In the twin-electrode configuration the showerhead-type gas inlet is replaced by an electrode of the same construction as the bottom electrode. In this configuration the process gases enter the reactor through the annular gap between the powered part of the electrode, which will henceforth be referred to as cathode, and the ground shield. The cup-like ground shield has an outer diameter of 86 mm. The cathode has an outer diameter of 80 mm and is cooled by water circulating through it at a flow rate of 4-6 liter per minute. The annular gap between the cathode and the ground shield has a width of 1 mm. The showerhead-type gas inlet and the electrodes can be moved individually by large membrane bellows. The membrane bellows permit a shift of 50 mm each. This increases the versatility of the reactor, because it allows one to vary the electrode gap as well as to shift the complete electrode configuration along the rotational symmetry axis of the reactor. In the single-electrode configuration the electrode gap can be adjusted from 0 mm to 45 mm. In the twin-electrode configuration the electrode gap can be adjusted from 0 mm to 35 mm. The electrode system can be operated in two electrical configurations, an asymmetric configuration

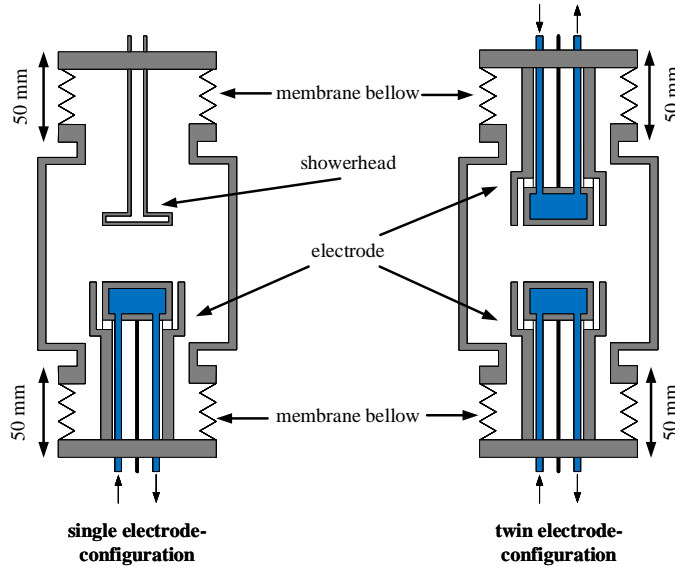


Figure 3.5: Schematic drawing of the two possible electrode installation configurations. In the single electrode configuration the upper electrode is replaced by a showerhead, which serves as the gas inlet. In the twin electrode configuration two identical electrodes are installed on the 'Pequod'-reactor.

and a symmetric push-pull configuration (cf. figure 3.6). In the asymmetric configuration the cathode of the top electrode or the showerhead-type gas inlet are grounded. Like the ground shields of the electrodes they are connected to ground potential via their mechanical connections to the vacuum chamber. The cathode of the bottom electrode is driven by an RF-generator (RFG100, *Coaxial Power Systems*) operating at 13.56 MHz. An automatic L-type matching network (AMN150, *Coaxial Power Systems*) between the RF-generator and the electrode system minimizes the amount of power reflected back to the RF-generator. The resulting discharges are asymmetric (cf. subsection 2.1). The push-pull configuration in conjunction with the twin-electrode configuration can be used to generate symmetric discharges. This is achieved by driving both cathodes with a phase shift of π . The phase shifted drive is generated by a balun placed after the matching network. The balun consists of two air coils stacked into each other on a common support. The coil on the output side of the balun has a grounded midpoint connection. This generates two drive signals of equal amplitude and a phase shift of π at the output terminals.

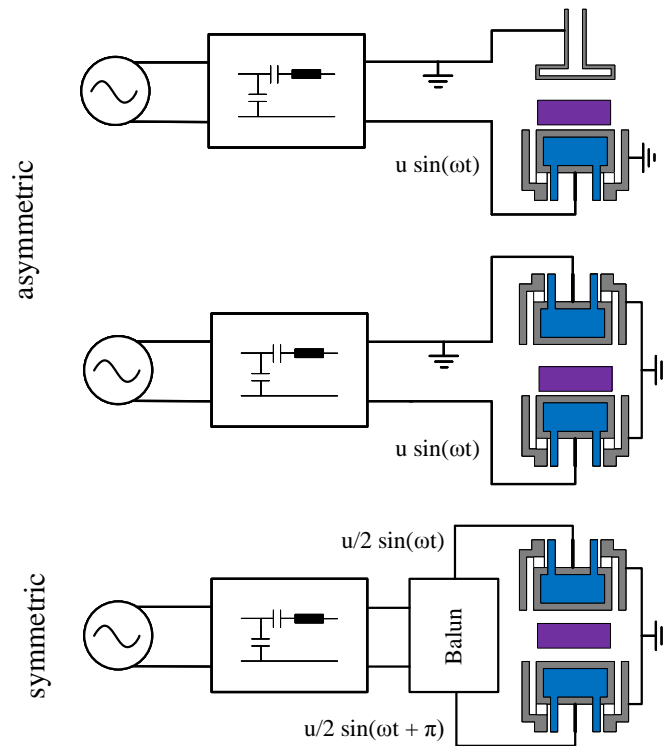


Figure 3.6: Schematic drawing of the electrical configurations in which the electrode system can be operated. Without the balun (B) the generated discharges are asymmetric. Only the push-pull configuration with the balun results in a truly symmetric discharge. In all configurations, an automatic L-type matching network is placed between the RF-generator and the 'Pequod'-reactor.

3.2 Particle Collector Module

The particle collector module uses the same collection scheme as the one described in [49]. A schematic drawing of the collector module can be found in figure 3.7. It is based on a small vacuum chamber (CF63 6-way cross)

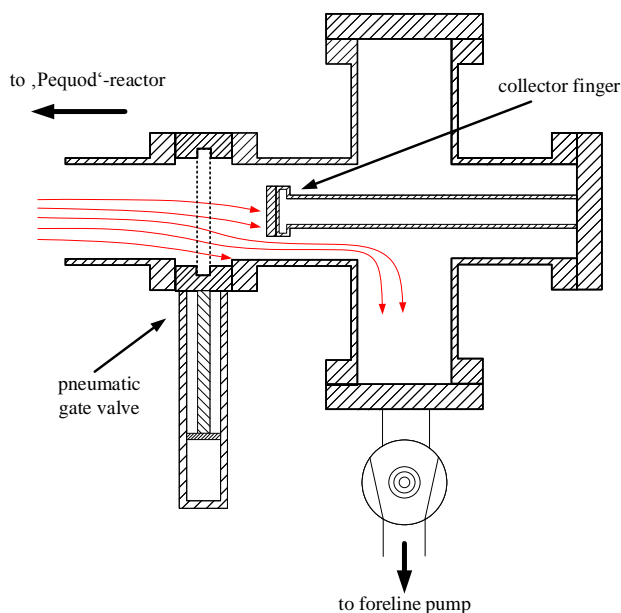


Figure 3.7: Schematic drawing of the particle collector module attached to the 'Pequod'-reactor. The red lines indicate possible trajectories of particles that have been dragged into the collection module. The particles are either deposited on the walls of the module or on the collector finger, or are dragged into the pumping system of the module.

that has been connected to one of the ports on the A-axis of the 'Pequod'-reactor' (cf. figure 3.2) and can be isolated from it by a pneumatically actuated gate valve. The collector module has its own turbomolecular pump (HiPace® 60P, Pfeiffer Vacuum) and can be isolated from the foreline pump it shares with the 'Pequod'-reactor. This allows one to vent and evacuate the collection system independently of the 'Pequod'-reactor. This load-lock functionality provides a high throughput. The pressure inside the collection system can be monitored with a Pirani gauge (TPR270, Pfeiffer vacuum). The substrates for collecting the particles are glued onto the front plate of the collection finger with vacuum compatible adhesive tape. The shaft of the collection finger is hollow so that it could be retrofitted with a system for cooling or heating of its front plate.

In general, the collection of nanoparticles from the 'Pequod'-reactor with this collector module was conducted according to the following protocol. Before the discharge in the reactor is ignited, a fresh substrate is mounted onto the collection finger and the collector module is evacuated to a pressure smaller than 5×10^{-2} Pa. After that, the discharge in the reactor can be ignited. The signal that starts the RF-generator serves as a reference for the collection process. The gate valve between the reactor and the collection system is opened at a preset time after this reference signal. The gate valve is opened completely and is closed directly afterwards. This whole process takes approximately 2 s. During this time period nanoparticles are dragged out of the reactor into the collector system. The red lines in figure 3.7 indicate possible particle trajectories. The particles can precipitate onto the collector finger or the walls of the collector system or they are dragged into the pumping system of the collector system. The pumping system of the collector system is then isolated from the pumping system of the reactor and is subsequently vented to remove the substrate with the collected particles and prepare the system for the next collection experiment. The preparation for the next collection experiment includes a cleaning process for the reactor. During the cleaning process the gate valve between the collector module and the reactor is automatically opened and closed 5 times with an interval of 20 s. Throughout the cleaning process a pure Ar discharge is running in the reactor at a pressure of 8 Pa and an RF power of 10 W. The cleaning process should remove any residual particles, which do not stick to the inner walls, from the reactor or the collector module.

3.3 Discharge Diagnostics

3.3.1 Impedance Probe

An impedance probe (Octive Poly, *Impedans Ltd*) has been directly attached to the Type N input connector of the bottom electrode. The impedance probe was used to measure the RF-voltage amplitude, the RF-current amplitude, the phase angle between RF-current and -voltage, and the impedance of the discharge. The probe was configured such that this data set was acquired simultaneously for the first five harmonics (13.56 MHz, 27.12 MHz, 40.68 MHz, 54.24 MHz, and 67.80 MHz) of the operating frequency of the RF generator. For all experiments described in this work the sample time of the probe was set to 200 ms.

3.3.2 Optical Emission Spectroscopy

The optical emission of the discharge was detected and analyzed with a fibre-coupled spectrometer (STS-VIS, *Ocean Optics*). The spectrometer is optimized for operation in the visible range and covers the wavelength range from 350 nm to 800 nm. The width of the entrance slit is 25 μm resulting in an optical resolution of 1.5 nm. A solarization-resistant optical fibre with a core diameter of 400 μm (QP400-2-SR-BX, *Ocean Optics*) was used to guide the light emitted from the discharge to the spectrometer. The field of view of the fibre was increased by a collimating lens (74-UV-MP, *Ocean Optics*), which was directly attached to its input connector. The collimating lens was centred on the symmetry axis of a fused silica viewport (VPZL-275Q, *Kurt J. Lesker*), which was mounted on a CF 40 port on the circumference of the 'Pequod'-reactor (cf. figure 3.3). The integration time of the spectrometer was set to 200 ms for all experiments described in this work

3.3.3 Quadrupole Mass Spectrometer

A simple quadrupole mass spectrometer (PrismaPlus®, *Pfeiffer vacuum*) was used for obtaining basic information about the plasma chemistry during particle formation. Because the spectrometer has a detection limit of $m/z = 100$ only molecules with a relatively low molecular weight are detectable. The mass spectrometer is part of a separate module, which was attached to the 'Pequod'-reactor (cf. figure 3.3). Like the particle collection system the mass spectrometer module is based on a CF63 6-way cross. The module is evacuated to a base pressure of $p_b \approx 1 \times 10^{-5}$ Pa by a turbomolecular pump (HiPace 80, *Pfeiffer Vacuum*), which also provides differential pumping dur-

ing the operation of the mass spectrometer. The pressure inside the module is monitored with a full-range cold cathode gauge (PKR270, *Pfeifer Vacuum*). As the mass spectrometer module can be isolated from the 'Pequod'-reactor and the foreline pump it shares with the reactor by valves, both systems can be vented and evacuated independently of each other. In addition to the reduction provided by the differential pumping of the mass spectrometer module a further pressure reduction between the mass spectrometer and the 'Pequod'-reactor was achieved by inserting an orifice between the two systems. The orifice has a diameter of 0.4 mm and a thickness of 0.5 mm. The orifice was placed directly after the gate valve separating the spectrometer module from the 'Pequod'-reactor to minimize the volume trapped between the gate valve and the orifice. With this configuration a pressure of approximately 8×10^{-4} Pa could be maintained in the mass spectrometer module at a process pressure of 8 Pa inside the 'Pequod'-reactor. All measurements of the time evolution of ion currents described in this work were performed with an integration time of 200 ms for each ion current.

3.3.4 Multipole Resonance Probe

The multipole resonance probe (MRP) that has been used in this work is similar in design to the probe described in [68]. The outer diameter of the quartz tube that surrounds the hemispherical dipole probe has an outer diameter of 10 mm. The probe was mounted on the rectangular port of the 'Pequod'-reactor and was centred on the B-axis (cf. figure 3.2 and 3.3). The position of the probe on the B-axis can be adjusted with a stepper motor. If not mentioned otherwise, the probe was positioned at a distance of approximately 30 mm from the centre point of the reactor on the side of the rectangular port. The resonance spectrum of the probe is recorded with a network analyzer (ZVL6, *Rohde & Schwarz*). The resonance spectra have been recorded with an integration time of 500 ms.

3.3.5 UV/Vis-transmission Spectroscopy

The setup for transmission spectroscopy consists of a fibre-coupled light source and a fibre-couple spectrometer. The spectrometer (STS-UV, *Ocean Optics*) is optimized for use in the UV range and covers the wavelength range from 190 nm to 650 nm. The output of the light source is generated by a tungsten halogen and a balanced deuterium lamp (DH-2000-BAL, *Ocean Optics*). To avoid excessive degradation of the optical fibres by the UV light, solarization-resistant fibres with a core diameter of 400 μm (QP400-2-SR-BX, *Ocean Optics*) are used. Collimating optics attached to both fibres are

used to couple the light in and out of the fibres and to minimize the divergence of the beam that passes through the discharge. A combination of a plano-convex lens with a focal length of 35.1 mm (LA4052, *Thorlabs*) and a positive meniscus lens with a focal length of 100 mm (LE4173, *Thorlabs*) is used in the collimating optics. Both lenses have a diameter of 25.4 mm and are made from fused silica. To align both optics, the lenses as well as the fibres are mounted on adjustable stages within a cage system. The cage systems provide a rough centring of the optics on the B-axis of the 'Pequod'-reactor. The diameter of the collimated beam was approximately 12 mm at the centre of the reactor. The diameter of the beam was determined by projecting it onto a fluorescent detector card (VRC2, *Thorlabs*) at different distances. The transmission spectra shown in this work have been recorded with an integration time of 200 ms.

3.3.6 Small Angle X-ray Scattering

Investigations of the particle growth process by SAXS were performed at the P03 beamline [88] at the DESY synchrotron facility. A schematic drawing in figure 3.8 illustrates how the 'Pequod'-reactor was incorporated into the beamline. The 'Pequod'-reactor itself was mounted on a heavy load goniometer, which provided the ability to adjust the position of the reactor with respect to the X-ray beam precisely. The frame coupling the goniometer and the reactor was designed in such a way that the X-ray beam should lie on the B-axis of the reactor (cf. figure 3.2). To minimize parasitic scattering from the ambient atmosphere the entrance window of the reactor was placed directly behind the front-end of the beamline and an evacuated flight tube was installed between the 'Pequod'-reactor and the 2d X-ray detector Pilatus 1M, *Dectris*). Because the flight tube is not flexible enough, it was necessary to install a flexible membrane bellow between the reactor and the flight tube to retain the positioning capabilities of the goniometer. Furthermore, an intermediate X-ray window between the reactor and the flight tube isolates their pumping systems so that the conditions inside the reactor, e.g. the gas flow, are not affected. Except for the exit window of the front end, which is made from silicon nitride, all X-ray windows are made from Kapton® film. The entrance window of the reactor, the intermediate window and the exit windows at the end of the flight tube have thicknesses of 25 μm , 75 μm , and 125 μm , respectively. The open diameters of the entrance window and the intermediate window are 20 mm and 66 mm, respectively. An image of the entrance and intermediate windows can be found in figure 3.9. The distance between the centre of the reactor and the X-ray detector (SDD) was determined with a calibration sample (collagen). By matching the recorded

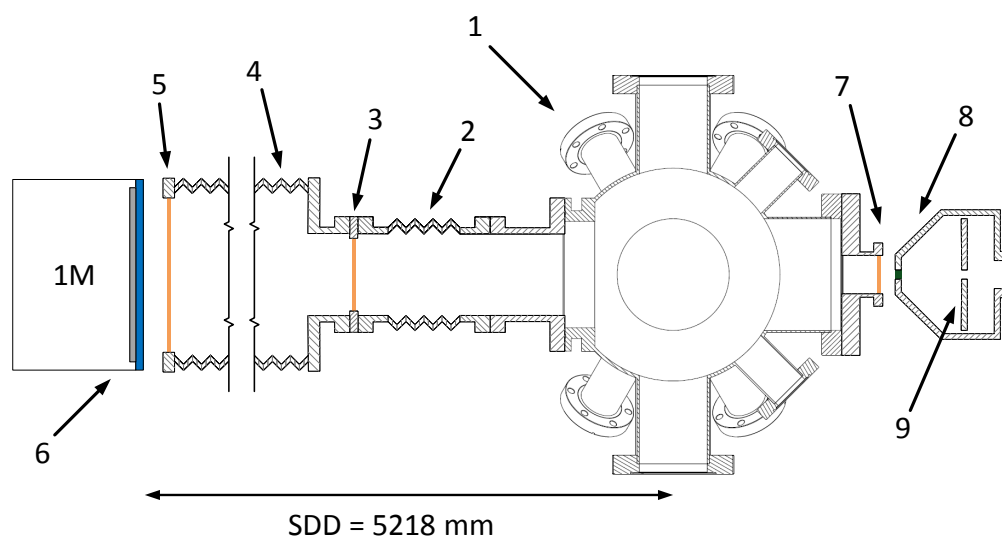


Figure 3.8: Schematic drawing of the SAXS setup at the P03 beamline. The 'Pequod'-reactor (1) is connected to the flight tube of the beamline (4) with a flexible membrane bellow (2). A Kapton® window (3) separates the 'Pequod'-reactor from the pumping system of the flight tube. Another Kapton® window (5) at the end of the flight tube in front of the 2d X-ray detector (6) serves as the exit window. The Kapton® entrance window (7) is placed directly behind the front-end of the P03 beamline (8). The front-end has a silicon nitride exit window and contains conditioning and guard slits (9) for the X-ray beam. The distance from the centre of the reactor to the detector (SDD) is 5218 mm.

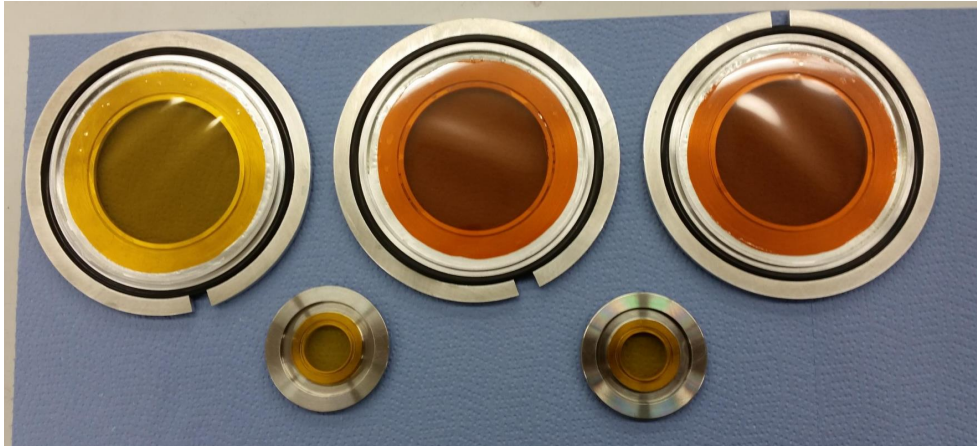


Figure 3.9: Image of different Kapton® windows. The small entrance windows have a Kapton® film thickness of $25\ \mu\text{m}$ (yellow film) and an open diameter of . The larger intermediate windows have a film thickness of $75\ \mu\text{m}$ (orange film) and an open diameter of . The intermediate window with a film thickness of $25\ \mu\text{m}$ ruptured during an evacuation test.

diffraction pattern to the expected pattern a value of $\text{SDD} = 5218\ \text{mm}$ was obtained. The size of the X-ray beam is defined by the conditioning and guard slits inside the front-end. The beam size is not larger than $40\ \mu\text{m} \times 20\ \mu\text{m}$. All scattering experiments were performed with an electron energy of $13\ \text{keV}$, which corresponds to a wavelength of $0.095\ \text{nm}$.

3.4 Electron Microscopes

A field emission SEM with an in-lens detector (GeminiSEM®[®], *Zeiss*) was used to study the surface structure, size, and size distribution of collected nanoparticles. In general, the microscope was operated with an acceleration voltage of 5 kV and a working distance of 3.4 mm to generate images with magnifications in the range of 10k \times to 200k \times . No additional coating was applied to the particles prior to their investigation by SEM.

TEM investigations of collected nanoparticles were carried out with two different microscopes. Morphological characterisation of the particles with bright-field imaging was performed at an acceleration voltage of 200 kV in a TEM with a LaB₆ source (JEM-2100, *JEOL*). For bright-field imaging the particles were collected on TEM grids with an amorphous carbon coating (S160-3, *Plano*) or on Si₃N₄-membranes (NTSN100A10Q33, *Plano*). Chemical characterisation of collected particles with EELS was performed in another microscope (Tecnai F30, *FEI*). In contrast to the JEM-2100, the Tecnai F30 is equipped with a field emission source and is operated at an acceleration voltage of 300 kV. To obtain information about the chemical composition within a single particle the microscope was operated in STEM-mode. Because the amorphous carbon coating on TEM grids would interfere with the chemical characterisation of the hydrocarbon-based particles only particles collected on Si₃N₄-membranes were used for EELS measurements.

Chapter 4

Results

4.1 Cyclic Behaviour of the Discharge

As mentioned earlier in section 1 the formation of nanoparticles in reactive plasmas follows different modes depending on the process parameters and the configuration of the discharge. To compare the results with those obtained previously in a different plasma reactor [49, 90], an asymmetric configuration, replacing the top electrode with the showerhead, was chosen. The position of the bottom electrode and the showerhead with respect to the height of the centre point of the reactor is depicted in figure 4.1. The process parameters had to fulfill four basic requirements:

- Reliable formation of nanoparticles
- Substantial change of discharge parameters during the formation of the nanoparticles
- Stable operation of the discharge during the formation of nanoparticles
- Comparable to process parameters used in previous experiments [49, 90, 91]

From the process parameters fulfilling these requirements the set in table 4.1 was chosen. If not mentioned otherwise all experiments described in this work were performed with these process parameters. Therefore, this set is henceforth referred to as 'standard process parameters'.

Running the discharge at this particular set of process parameters results in the formation of nanoparticles (cf. figure 4.2) and a periodic change of discharge parameters. As the change of discharge parameters results from the interaction with the nanoparticle ensemble dispersed in the discharge the

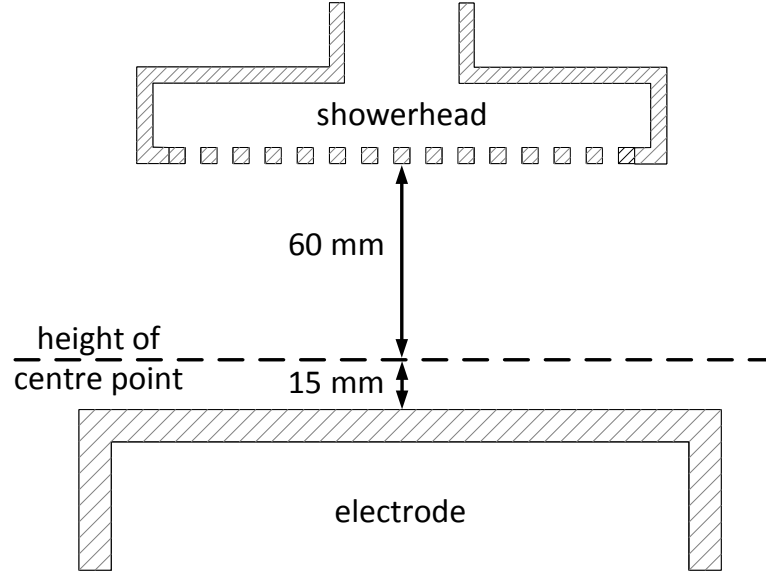


Figure 4.1: Schematic drawing of the position of the showerhead and the electrode with respect to the height of the centre point of the 'Pequod'-reactor (cf. figure 3.2). For simplicity the groundshield of the electrode is not included in the drawing.

ensemble should display a periodic behaviour as well. An example of the aforementioned periodic changes can be found in figure 4.3. Although any of the discharge parameters could have been used as a reference to describe the periodic behaviour of the discharge, the phase angle ϕ_{RF} between the 1st harmonics of RF-current and- voltage was chosen as a reference, because it has been recorded for all experiments, it is unaffected by the symmetry of the discharge, and it has been used in previous works (cf. for example [49, 52, 95–97]) to identify different phases of the particle formation process. The discharge cycle is therefore solely defined on the basis of the time evolution

Table 4.1: Standard process parameters

Parameter	Symbol	Value
Absolute pressure	p	8 Pa
RF-power	P_{RF}	10 W
Ar-flux	Q_{Ar}	10 sccm
C ₂ H ₂ – flux	$Q_{\text{C}_2\text{H}_2}$	1 sccm

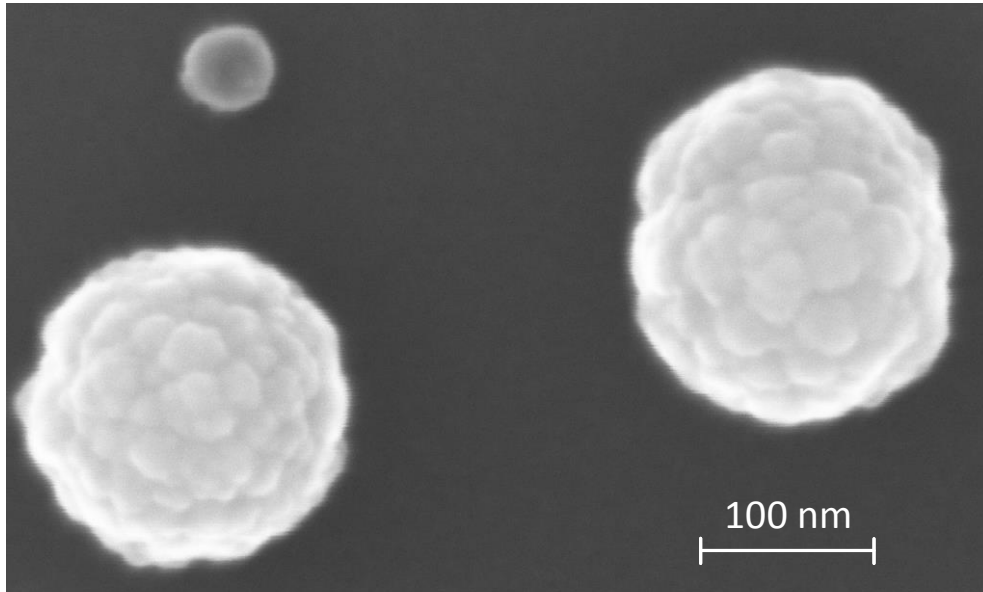


Figure 4.2: SEM micrograph of nanoparticles collected from a discharge run at the standard process parameters (cf. table 4.1). The larger particles have the typical cauliflower shape [92–94].

of the phase angle. A schematic drawing illustrating the definition of the discharge cycle can be found in figure 4.4.

Although the time evolution of each discharge parameter is similar in every discharge cycle the 1st cycle differs for many parameters from the subsequent cycles in one or the other aspect. In the case of ϕ_{RF} , its decrease is more pronounced in the 1st cycle (cf. figure 4.3). That raises the question whether the nanoparticle formation in the 1st and subsequent cycles is similar. As ϕ_{RF} approaches the same value as for the pristine (devoid of nanoparticles) discharge at the end of each cycle one may assume that all nanoparticles have left the discharge and the conditions of the pristine discharge have been restored. But UV/Vis transmission spectra and the collection of nanoparticles disprove this assumption. Figure 4.5 shows the time evolution of the transmission through the discharge around the end of the 1st discharge cycle for three selected wavelengths. For a pristine discharge the UV/Vis-transmission is 100 % over the detectable spectral range. Absorption by hydrocarbon molecules that form in the plasma should only have a negligible effect on the transmission spectrum. At a wavelength of 230 nm the photoabsorption crosssection $\sigma_{\text{ph,a}}$ of acetylene is of the order of 10^{-26} m^2 and decreases with increasing wavelength [98]. For an acetylene

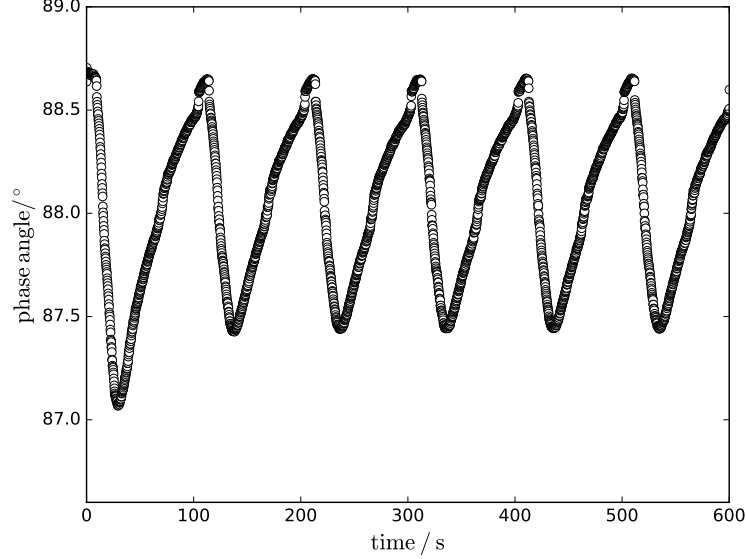
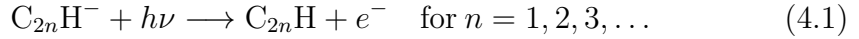


Figure 4.3: Time evolution of the phase angle ϕ_{RF} between the 1st harmonics of RF-current and- voltage during a process run with the standard process parameters. The discharge was ignited at $t = 0$ s.

number density of $2.5 \times 10^{20} \text{ m}^{-3}$, corresponding roughly to a pressure of 1 Pa of an ideal gas at 300 K, and a reactor diameter of 200 mm one would expect a decrease of the transmission by less than $5 \times 10^{-5} \%$. The statistical fluctuations of the light source's intensity will have a much bigger effect than the absorption by acetylene. Even if some of the produced hydrocarbon molecules have larger crosssections, their number densities are expected to be substantially lower than that of acetylene [42, 43]. However, absorption of photons in photodetachment reactions with hydrocarbon anions



may affect the transmission spectra. Up to $n = 3$ the crosssection for photodetachment $\sigma_{\text{ph,d}}$ is of the order of 10^{-21} m^2 at a photon energy of 5 eV, which corresponds approximately to a wavelength of 250 nm; $\sigma_{\text{ph,d}}$ decreases rapidly with increasing wavelength [99, 100]. The photodetachment crosssection $\sigma_{\text{ph,d}}$ is substantially larger than the photoabsorption crosssections $\sigma_{\text{ph,a}}$, because the electron affinity of anions is, in general, lower than the ionization and dissociation energies of neutral species. If the number density of the anions were as high as the number density of acetylene, photodetachment would indeed affect the transmission spectra. But, based on the simulations

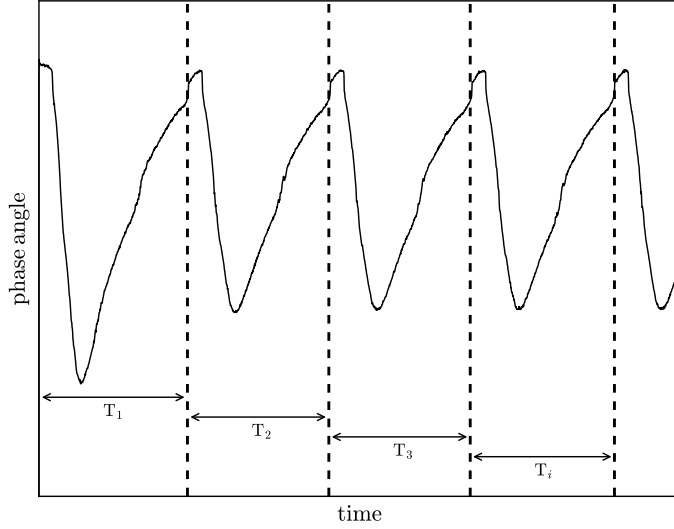


Figure 4.4: Schematic drawing illustrating the definition of the discharge cycle based on the time evolution of the phase angle ϕ_{RF} .

of *DeBleecker et al.*, the number density of anions is expected to be smaller than that of acetylene by a factor of 10^5 [42, 43]. Making the same approximations as in the previous calculation, the decrease of the transmission by photodetachment is similarly small. The observed decrease in transmission is solely originating from absorption or scattering by the nanoparticle ensemble in the discharge.

As can be seen from figure 4.5, the transmission doesn't reach 100 % for any of the wavelengths at the end of the 1st discharge cycle. The transmission T_{532} at 532 nm and the transmission T_{633} at 633 nm reach 100 % some seconds after the end of the 1st discharge cycle. The transmission T_{250} at 250 nm remains below 100 %. Although a step-like change of the transmission can be observed at the end of the 1st discharge cycle, it doesn't seem to be the case that all nanoparticles leave the discharge at this particular time point. The slow increase of the transmission indicates that a significant portion of the nanoparticle ensemble leaves the discharge only gradually over an extended period of time. This interpretation is confirmed by collecting particles from the discharge directly after the end of the 1st discharge cycle. A representative SEM-image can be found in figure 4.6. If indeed all nanoparticles had left the discharge at the end of the 1st discharge cycle, only small particles that have formed in the 2nd discharge cycle should have been

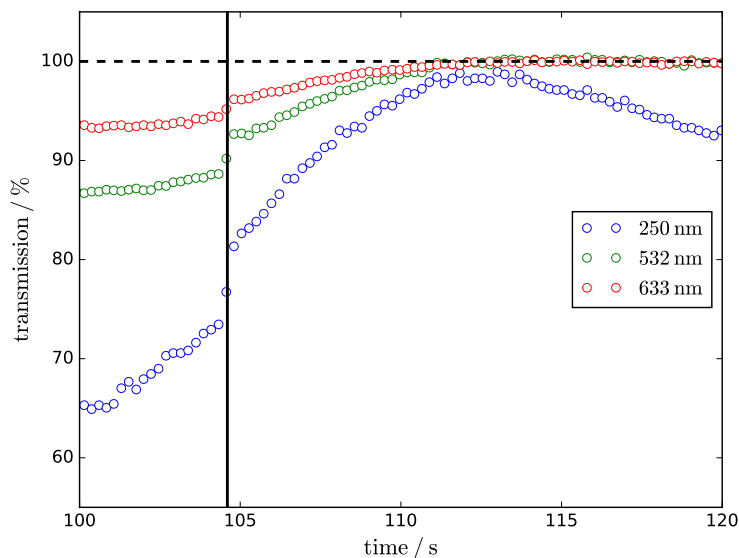


Figure 4.5: Time evolution of the transmission of light with wavelengths of 250 nm, 532 nm, and 633 nm through the discharge. The solid vertical line indicates the end of the 1st discharge cycle. The dashed horizontal line indicates 100 % transmission

collected. However, the size distribution of the collected particles appears to be trimodal. It includes large particles, particles of intermediate size, and small particles. Both the large particles and the particles of intermediate size can not have formed in the 2nd discharge cycle as this would require very large growth rates of up to 100 nm/s. These particles must have formed in the 1st discharge cycle and remained trapped in the discharge. As has been reported previously [49], the large cauliflower shaped particles can also be found much later in other discharge cycles. Whether the small particles that can be seen in figure 4.6 have formed in the 1st or 2nd discharge cycle remains unclear.

That the 1st discharge cycle differs from subsequent cycles (cf. figure 4.3) suggests that the particle formation in the 2nd discharge cycle is affected by the larger particles. As will be shown in section 4.6, large particles grow by surface deposition of hydrocarbon species formed in the discharge. They act as a kind of internal getter pump reducing the number density of these hydrocarbon species. If this reduction is significant the nucleation rate of nanoparticles should be reduced. It has indeed been shown that nanoparticles only nucleate in areas of the discharge with a sufficiently low number

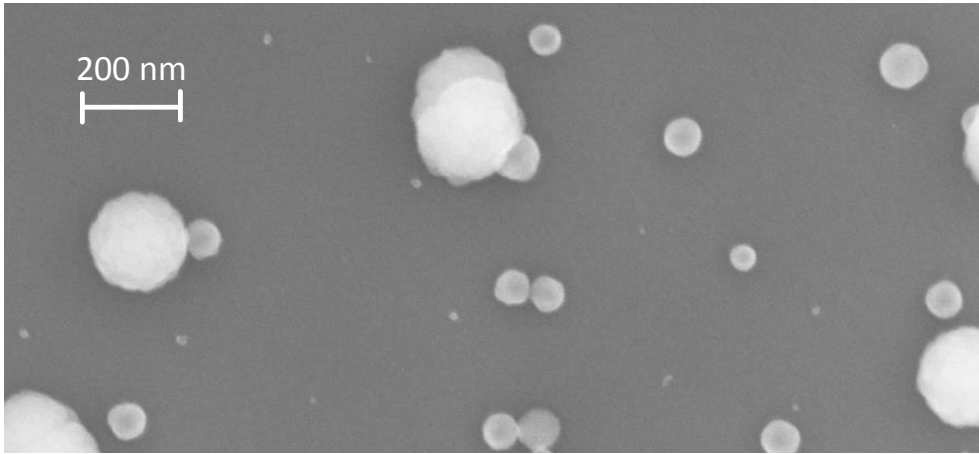


Figure 4.6: SEM-image of nanoparticles collected 2.4 s after the end of the 1st discharge cycle of a discharge run at the standard process parameters.

density of nanoparticles, like voids, i.e. particle free volumes inside the discharge [101–103]. A reduced nucleation rate leads to a lower number density of nanoparticles in the discharge. Discharge parameters that are sensitive to the number density of nanoparticles should show a reduced response to the nanoparticle ensemble. However, the situation might be more complicated. If one considers the time evolution of the transmission through the discharge in the different discharge cycles, it seems that it does not indicate a reduction of the number density of nanoparticles. A representative data set is shown in figure 4.7. As mentioned earlier, the transmission at 250 nm does not reach 100 % transmission in the 2nd or subsequent discharge cycles. This differentiates them from the 1st discharge cycle. But, in all discharge cycles the same minimal transmission is observed. This is unexpected for a reduced number density of nanoparticles. A possible explanation is that, in contrast to the phase angle, which is a global quantity of the discharge, the transmission through the discharge is a locally probed, line integrated quantity. This indicates that the difference between the 1st and the subsequent discharge cycles might not only be caused by a different number density of nanoparticles but also by a different spatial distribution of the particles in the discharge. The following simplified scenario shall serve as an illustration for this interpretation. Figure 4.8 shows two different spatial distributions of nanoparticles in the discharge. In the first configuration the nanoparticle ensemble is homogeneously distributed throughout the whole cylindrical plasma bulk. In the second configuration a cylindrical void has formed inside the bulk. The

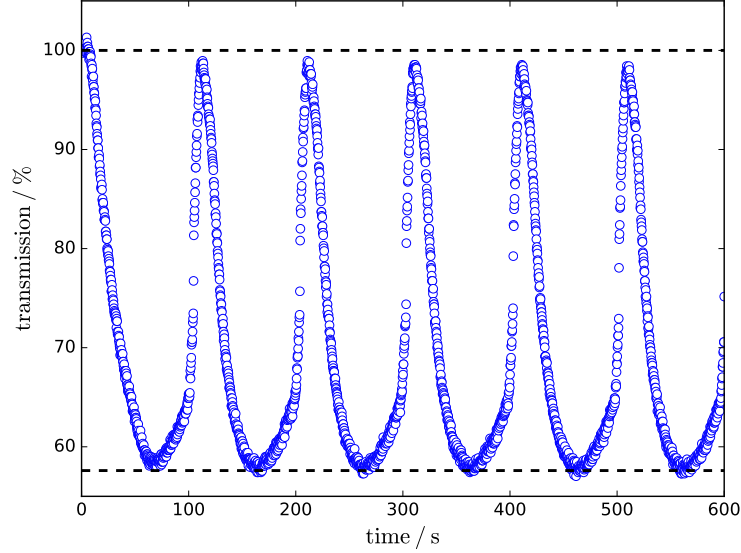


Figure 4.7: Time evolution of the transmission of light with a wavelength of 250 nm through the discharge. The dashed horizontal lines indicate 100 % transmission and the minimal transmission during the 1st discharge cycle. the discharge was ignited at $t = 0$ s

nanoparticle ensemble forms a shell around the void. If the number density of particles in the shell has the right value, the different spatial distributions of the particles are indistinguishable by measuring the transmission through the discharge because it is a line integrated quantity. However, the electrical characteristics of the discharge, which affect the phase angle, could nevertheless be different in both configuration. In the first system, the resistivity of the plasma bulk is high but homogeneous so that the plasma bulk can be described by a single resistor. In the second configuration, the resistivity of the plasma bulk is inhomogeneous. In a very simple approximation, it could be described by three resistors connected in series. Two resistors with a high resistance represent the particle-loaded shell and a resistor with low resistance is representing the void. The resistance of the void is expected to be lower because the free electron density is not reduced by nanoparticles, which has been verified in previous reports, cf. for example [104–106]. In general, the resistances of the plasma bulks in both configurations will be different even if the spatial distributions of the nanoparticle ensembles are indistinguishable by transmission measurements. For example, the configuration with a void could have a lower resistance because the Havnes-effect (cf. subsection

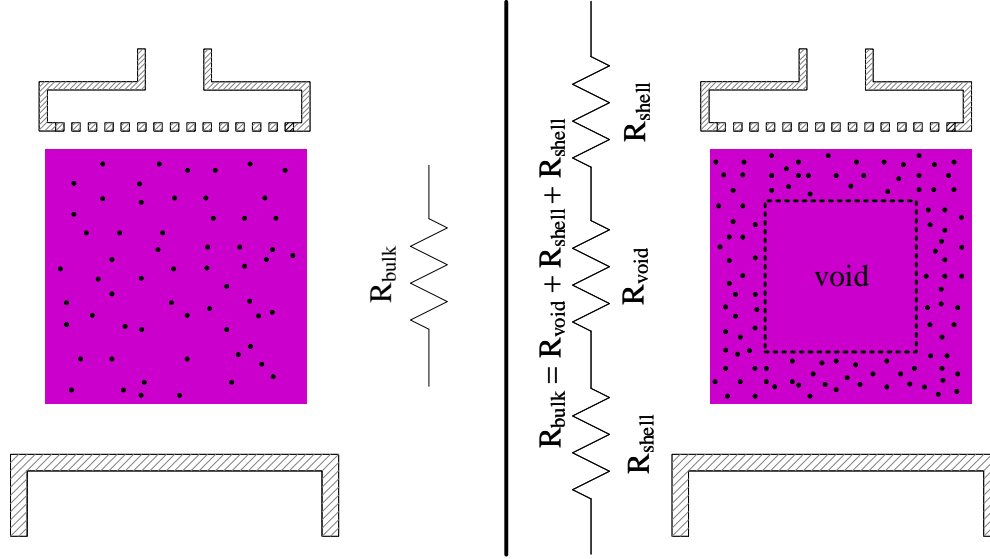


Figure 4.8: Schematic drawing of two different spatial distributions of nanoparticles inside the discharge. Equivalent circuits that could be used to describe the resistance of the plasma bulk are also shown.

2.3) limits the resistivity of the shell to a value close to the resistivity of the plasma bulk in the first configuration. In this case, the configuration with the void should be more capacitive, i.e. have a phase angle closer to 90° , than the configuration without. Whether this or another scenario can explain the observed differences between the 1st and subsequent discharge cycles needs to be investigated in future experiments. But, the apparent contradiction between the transmission measurements and the measurements of the phase angle perfectly illustrates why it is necessary to use a multidagnostic approach to investigate these systems. Interpretations solely based on either data set will likely be wrong or at least incomplete. Even the combination of both data sets does not provide an unambiguous interpretation of the differences between the 1st and subsequent discharge cycles. A reduction of the ambiguity can only be achieved by adding information from other diagnostics. For example, the 'Pequod'-reactor does not have a diagnostic that can directly detect the formation of a void. But, this information would be indeed very valuable for verifying the scenario described above.

Although it remains unclear how the presence of nanoparticles formed in the 1st discharge cycle affects the particle formation in subsequent cycles and the behaviour of the discharge, they undoubtedly have an effect. This becomes clear if one performs the particle collection process (cf. section

3.2) manually several times without switching off the discharge. The time evolution of the phase angle and the transmission at 250 nm during such an experiment can be found in figure 4.9. There is no difference between the 1st and the subsequent discharge cycles if the particle collection process is performed in each discharge cycle. The particle collection process appears to be as effective in removing the nanoparticles from the discharge as switching off the discharge. After the collection process the transmission at 250 nm

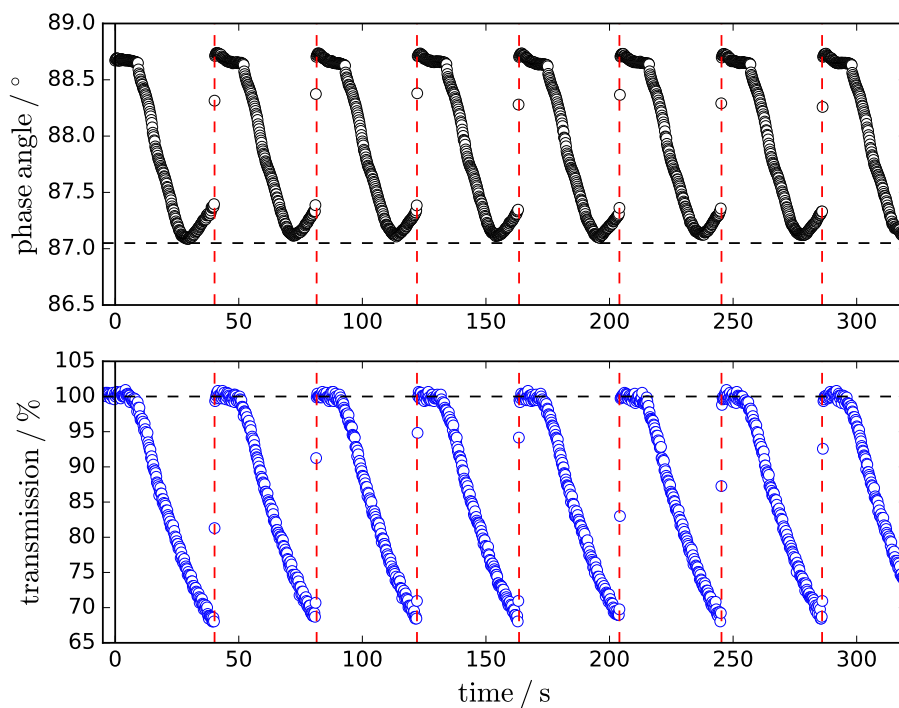


Figure 4.9: Time evolution of the phase angle and the transmission at 250 nm during an experiment in which particles were collected multiple times. The particle collection process was triggered manually after the phase angle had reached its minimal value. The solid black line marks the ignition of the discharge. The dashed lines indicate a transmission of 100 % and the minimal value of the phase angle during the 1st discharge cycle. The dashed red lines mark the time at which the particles were collected.

reaches a value of 100 % and the phase angle always reaches the same minimal value as in the 1st discharge cycle, which starts with the ignition of a pristine discharge. That one can apparently restore the discharge to its pristine state without switching off the discharge is an interesting finding, which could be

used for the deposition of nanoparticles. If it turns out that the particle formation process has a similar stability, which would need to be proven experimentally, one could collect nanoparticles at different times during their growth and create a particle ensemble with a very broad size distribution in a single process run. Broad size distributions are advantageous in applications that benefit from a high filling factor, cf. for example [107, 108].

4.2 Investigation of the 1st Discharge Cycle

A detailed study of the particle formation was only performed for the 1st discharge cycle. By considering only the 1st cycle the influence of particles formed in previous cycles, as mentioned in the preceding section, can be avoided. The formation process has been investigated by collecting nanoparticles from the discharge at different times during the 1st discharge cycle and determining their mean diameter from SEM-images. To correlate the time evolution of the mean particle diameter with that of the discharge parameters the 1st discharge cycle has been divided into 3 different phases (cf. figure 4.10).

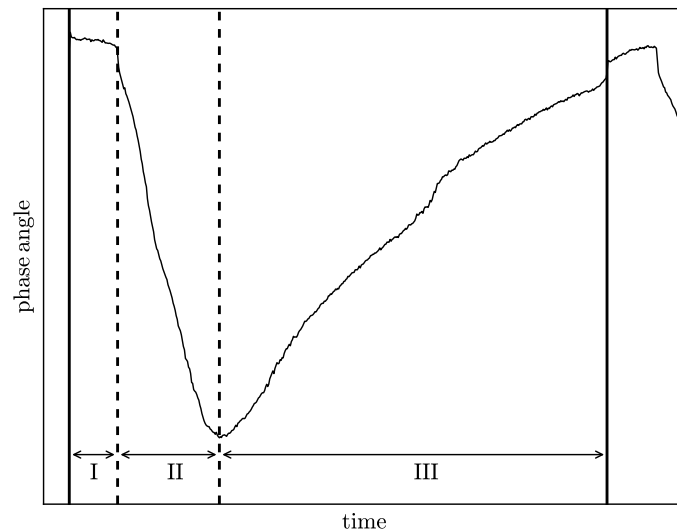


Figure 4.10: Schematic drawing depicting the definition of the different phases of the 1st discharge cycle. The solid black lines indicate the ignition of the discharge and the end of the discharge cycle. The dashed vertical lines indicate the boundaries between the different phases.

The point at which the particles were collected was defined by presetting the time t_c that elapses between the start of the RF generator and the opening of the gate valve of the particle collector module. Because the collection process interrupts the particle formation it is not possible to determine the length of the 1st discharge cycle T_1 , and depending on the value of t_c , the endpoints t_I and t_{II} of phase I and II, respectively from these experiments. To determine these values, reference experiments have been performed.

In the reference experiments the particle collection was intentionally performed in the 2nd discharge cycle so that T_1 , t_I , and t_{II} could be determined from the phase angle's time evolution. To monitor a possible drift of these values the reference experiments were performed in between a large set of collection experiments performed in the 1st discharge cycle. Figure 4.11 shows T_1 , t_I and t_{II} as functions of the cumulative process time, which denotes the time for which Ar – C₂H₂ discharges have been running in the reactor since the start of this particular set of experiments. It appears that the drift of all three parameters is small compared to their standard deviation. For further discussions of the results their drift is neglected. However, it should be pointed out that the reactor had been operated with Ar – C₂H₂ discharges for a considerable amount of time before the reference experiments were performed. The inner surface of the reactor was already coated by C-H based films. Experiments performed in freshly cleaned reactors lacking this passivated inner surface may indeed display a significant drift of T_1 .

For small values of the collection time the size distributions of collected particles are monomodal. But at the end of the 1st discharge cycle small particles are collected as well, resulting in a bimodal size distribution. From all the discharge parameters monitored during the discharge cycle only the mass spectrometer ion current corresponding to an m/z ratio of 50 I_{50} provides a feature at the end of the discharge cycles that may indicate the formation of a second particle generation. In contrast to this, *van de Wetering et al.* have reported that the coagulation of a second particle generation inside a void in the discharge results in a sudden change of the phase angle [95]. The feature observed in the time evolution of I_{50} is a transient shoulder that appears approximately 90 s after ignition (cf. figure 4.13). It is indeed the case that the size distributions of particles that were collected a few seconds before the onset of the shoulder are monomodal whereas they are bimodal if they were collected after the shoulder. Two representative SEM-images of such particle ensembles can be found in figure 4.12. Although the exact point at which this second generation of particles is formed remains to be identified the shoulder in the time evolution of I_{50} is nevertheless a useful fingerprint for this process.

Taking into account the transient nature of the shoulder and other reports [101–103] one can explain the formation of the second generation as follows. At first a void forms inside the discharge. The number densities of hydrocarbon species, especially radicals, increase because their consumption by surface deposition onto nanoparticles is strongly reduced inside the void. This explains the increase of I_{50} . The C₄H₂ molecule, which has one of the highest number densities in such Ar – C₂H₂ discharges [41–43, 109], is supposedly the main contributor to I_{50} . In addition, it has been reported that

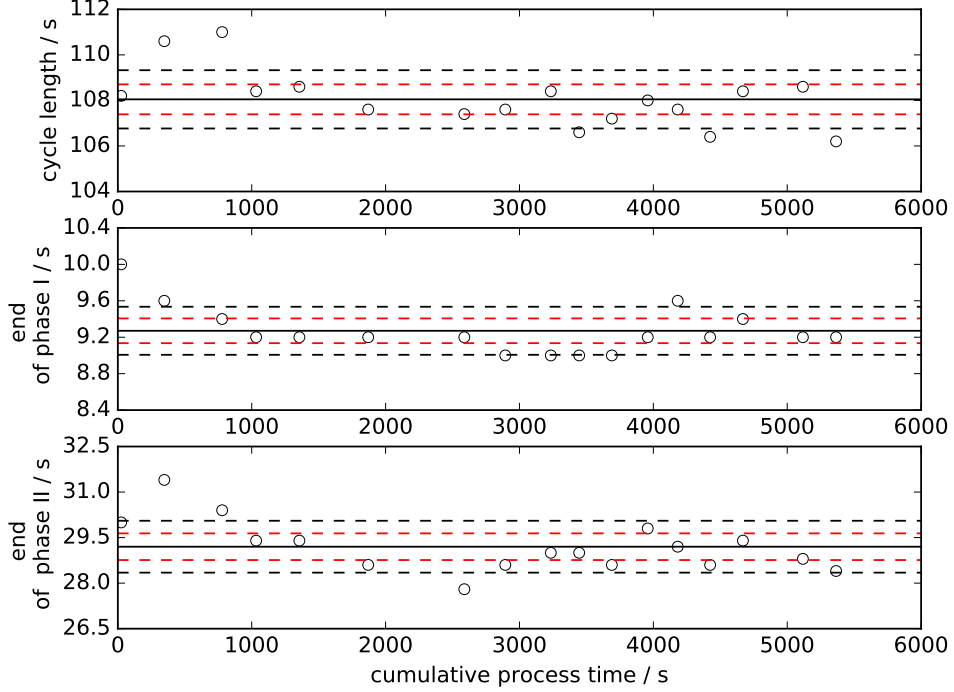


Figure 4.11: Scatter plot of the length of the 1st discharge cycle T_1 and the endpoints t_I and t_{II} of phase I and II, respectively as a function of the cumulative process time. The solid lines indicate the mean values. The black dashed lines mark the 1σ standard deviation and the red dashed lines mark the $\alpha = 0.05$ confidence interval of the mean values.

the free electron density n_e inside the void is higher than in the particle-loaded discharge surrounding it [104–106]. The presence of a high density of hydrocarbon species and electrons results in a high density of negative ions like C_4H^- . As negative ions are efficiently trapped inside the discharge they are believed to be important precursors for the formation of nanoparticles [42, 110–114]. Due to the increased precursor density a new particle generation forms inside the void. As soon as surface deposition onto these particles becomes significant the number density of hydrocarbon species and therefore I_{50} decreases again. As soon as the nanoparticles get permanently charged the electron density inside the void decreases as well. The lack of precursor molecules suppresses further nucleation events. The formation of this second generation also explains the presence of particles of intermediate size at the beginning of the 2nd discharge cycle. The existence of a void

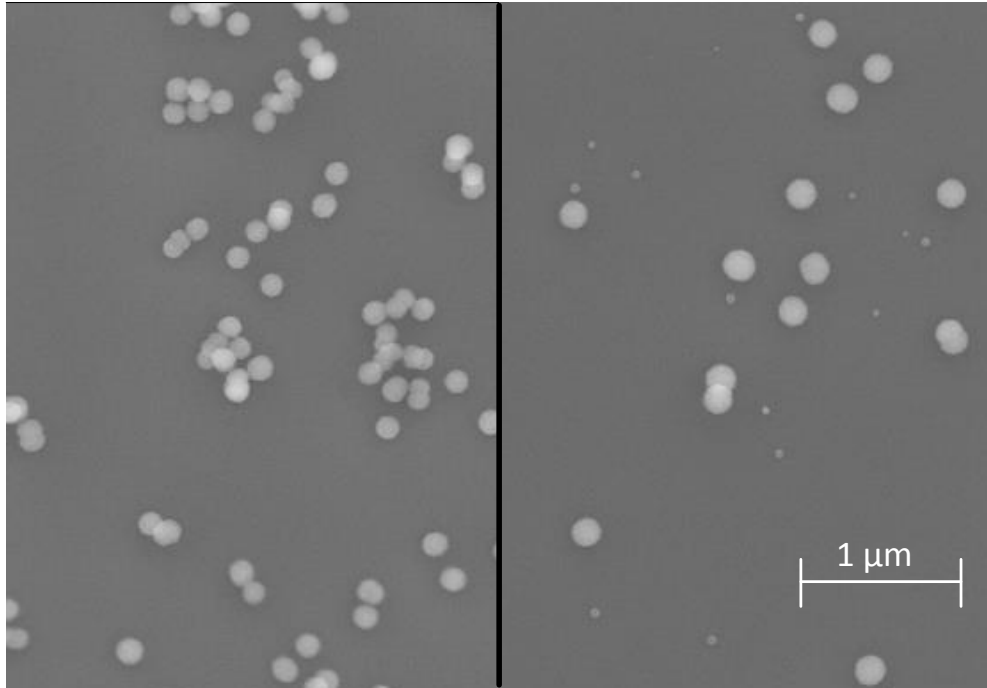


Figure 4.12: SEM-image of nanoparticles collected before (LHS) and after (RHS) the appearance of the shoulder in the time evolution of the mass spectrometer ion current I_{50} corresponding to an m/z ratio of 50 (cf. figure 4.13).

could be verified by passing a laser fan through the discharge and detecting the scattered laser light (cf. for example [103, 115–117]).

The formation of this 2nd particle generation has not been investigated in more detail. As has been pointed out above, I_{50} is the only discharge parameter that shows any significant discontinuity indicating the formation of the 2nd particle generation. The other discharge parameters appear to be unaffected. Although the discharge parameters are inevitably altered by this 2nd particle generation as well, the response of the discharge parameters is probably small compared to the response towards any change of the 1st particle generation. The diameter of the 1st generation particles shown in figure 4.12 is approximately 4.5 times larger than the diameter of the 2nd generation particles. Their areas and volumes differ by factors of approximately 20 and 90, respectively. For comparison, the Earth's diameter is only 3.7 times larger than the Moon's. That the number density of 2nd generation particles is so high that it compensates the size difference is quite

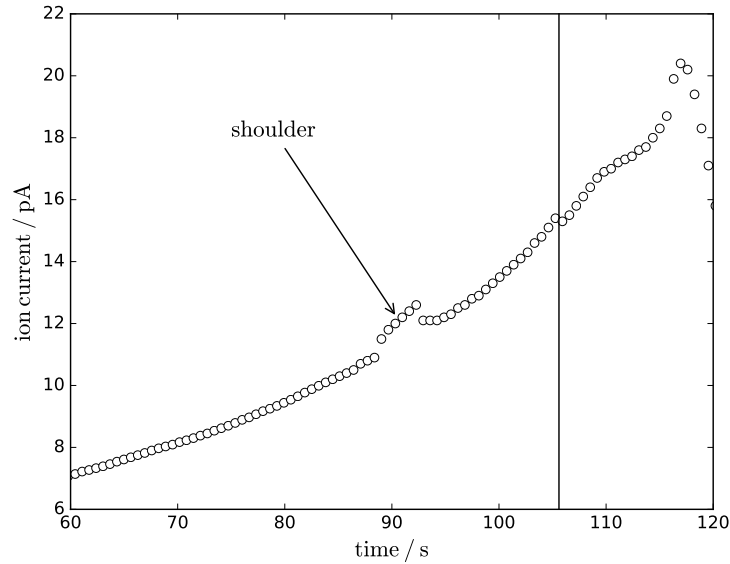


Figure 4.13: Time evolution of the mass spectrometer ion current I_{50} corresponding to an m/z ratio of 50 at the end of the 1st discharge cycle. The solid vertical line indicates the end of the 1st discharge cycle.

unrealistic. In section 4.6 it will be shown that the particle growth of the 1st generation particles is unaffected by the formation of the 2nd particle generation. Furthermore, most of the recorded discharge parameters are volume or line integrated quantities. It is not possible to infer any information about the conditions in the void, in which the 2nd generation particles presumably form, from them. This makes it difficult to compare the formation of the 1st and 2nd particle generation. Therefore, the subsequent discussion of the particle formation is restricted to the 1st particle generation. Nevertheless, the formation of a 2nd particle generation during the 1st discharge cycle already indicates that there is no strict correlation between the cyclic behaviour of the discharge and the formation of nanoparticles.

4.3 Onset of Particle Formation (Phase I)

4.3.1 Collection of Small Nanoparticles

The time evolution of the mean diameter $\langle d_p \rangle$ of the 1st nanoparticle generation formed in the 1st discharge cycle is depicted in figure 4.14. This graph

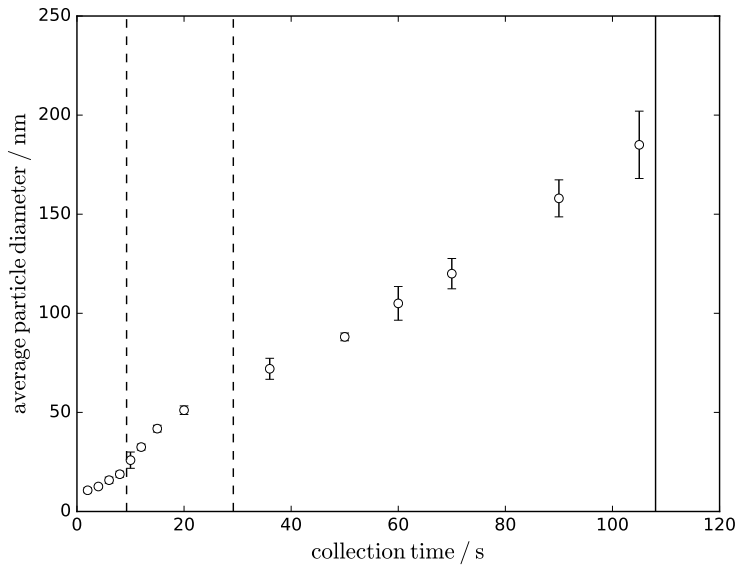


Figure 4.14: Plot of the mean diameter $\langle d_p \rangle$ of 1st generation particles formed in the 1st discharge cycle as a function of the collection time t_c . The dashed vertical lines mark the end of phase I and II, respectively. The solid vertical line marks the end of the 1st discharge cycle.

is of fundamental importance for the following discussion. For the reasons mentioned at the end of the preceding paragraph, it only contains information about the mean diameter $\langle d_p \rangle$ of 1st generation particles formed in the 1st discharge cycle. The 2nd particle generation that forms at the end of the 1st discharge cycle is not taken into account. The diameters of collected particles were determined by averaging the long and short axis of ellipses manually matched to individual particles on SEM images. Particles lacking a spherical shape because they are part of agglomerates were excluded from the size analysis. Each data point in figure 4.14 contains information from at least three different experiments and is the average of at least 50 particles. The particles were collected in process runs that have been performed in between the reference experiments that provided the data for figure 4.11. The markers in figure 4.14 indicating the end of the 1st discharge cycle and

the transition between the different phases represent the mean values shown in figure 4.11. A detailed discussion of the particle growth based on the data depicted in figure 4.14 is deferred to section 4.6.

The smallest particle diameters that could be reliably detected in this way lie in the range of 8-10 nm, depending on the quality of the images. Two factors contribute to this limit. The first factor is the fundamental resolution limit of the SEM given by the size of the interaction volume for secondary electrons (cf. section 2.5.1). The second factor that limits the detectable size is beam damage caused by the high electron current density at the required magnification. Typically the area scanned by the electron beam will start to blacken if the exposure time is too long. This is probably due to the deposition of residual hydrocarbon molecules, which have been dissociated by the intense electron beam. At lower base pressures in the microscope this effect is less pronounced. Sometimes this parasitic film deposition is so severe that the nanoparticles will start to grow if irradiated by the electron beam. This means that $\langle d_p \rangle$ is probably overestimating the real size of particles collected at 2 s and 4 s. Switching to TEM for measuring the size of the smallest particles did not provide any advantage. Although a TEM provides a much higher resolution than an SEM this is not necessarily true for the contrast between the particles and the background. Small particles were hardly detectable with the available TEM (cf. section 3.4).

One of the most important conclusions that can be drawn from figure 4.14 is that the formation of nanoparticles starts very early in the discharge cycle. Already 2 s after the ignition of the discharge nanoparticles with a mean diameter $\langle d_p \rangle = 11$ nm can be collected from the discharge. This is in agreement with the well-known model developed by *Bouchoule et al.* for Ar – SiH₄ discharges [39]. However, it predicts that such large nanoparticles could already be observed after the fast coagulation phenomenon at around 200 ms if the neutral gas temperature T_n is close to room temperature. This discrepancy may be a result of different discharge parameters and the different plasma chemistry in Ar – C₂H₂ discharges. Unfortunately, the experiments performed in this study cannot provide any information about the very first steps of particle formation. The only conclusion one can draw is that $\langle d_p \rangle$ grows rapidly in the first 2 s after the ignition of the discharge. Although the performed experiments are unable to provide information about the very first steps of the particle formation, they show that any experiment aiming at providing such information will be challenging. Not only will it be necessary to measure the diameter of carbonaceous nanoparticles smaller than 10 nm, but it will be necessary to do so with a time resolution well below 500 ms. In its current state the neutral drag based collection system does not have such a high time resolution. The transmission data in figure 4.9 show that it

takes approximately 400 ms to remove the majority of the particles from the discharge. The opening time of the gate valve could be the limiting factor. The DN63CF gate valve of the collector module has an opening time of approximately 1 s. If the opening time is indeed the limiting factor, the time resolution could be increased by installing a gate valve specifically designed for a fast opening time. An opening time of less than 6 ms for a DN40CF based gate valve has already been demonstrated [118]. Moreover, such a high time resolution will also require a precise synchronization of these measurements with the ignition of the discharge. Measuring the size of nanoparticles smaller than 10 nm could be done with a TEM. However, as has been mentioned above, detecting very small particles proved to be very difficult with the available TEM due to a lack of contrast between the particles and the substrates. The mass thickness, i.e. the product of thickness and density, of small particles is comparable to that of the supporting films. The amorphous carbon films have a thickness of 10 nm to 15 nm and their density should be comparable to that of the collected particles. The Si_3N_4 -membranes have a thickness of 10 nm and a higher density than the collected particles. The scattering contrast cannot be expected to be large. In addition, one has to take into account that the thickness of the particles is not constant in this context but decreases with increasing distance from the centre of the particle (cf. section 2.5.2). This exacerbates the weakness of the contrast. Atomic force microscopy (AFM) could be used as an alternative to TEM.

4.3.2 Schottky-emission from hot nanoparticles

Although the model by *Bouchoule et al.* is consistent with the formation of comparably large nanoparticles shortly after the ignition of the discharge it can not explain the time evolution of the discharge parameters. The model predicts that shortly after the fast coagulation phenomenon the nanoparticles formed by coagulation rapidly reduce the free electron density n_e in the discharge by charging up, thus leading to a change of other discharge parameters. This rapid change of discharge parameters is referred to as $\alpha - \gamma'$ transition [39]. However, the system under investigation does not display this specific behaviour. Neither the phase angle ϕ_{RF} , the voltage amplitude \hat{v}_1 of the fundamental at 13.56 MHz, the impedance z_{D} of the discharge, nor the intensity $I_{750.9}$ of the emission line at 750.9 nm do change drastically during the entire phase I of the discharge cycle. The time evolution of ϕ_{RF} and is depicted in figure 4.15. Although the discharge parameters show slight changes during phase I these changes are much smaller and much slower than the changes that are observed at the beginning of phase II. Such results have been reported before [49, 91] and are quite surprising. Following the well

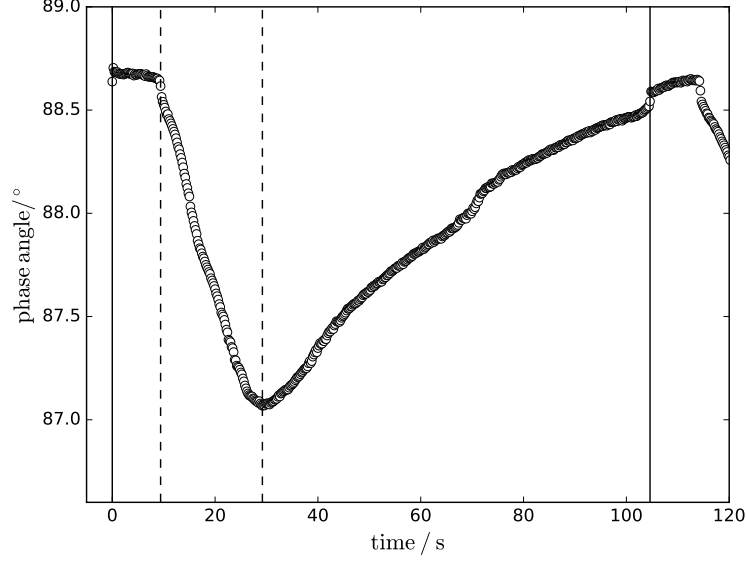


Figure 4.15: Time evolution of the phase angle ϕ_{RF} between the 1st harmonics of the RF-current and -voltage during the 1st discharge cycle. The dashed vertical lines indicate the end of phase I and II, respectively. The solid black lines mark the ignition of the discharge at $t = 0$ s and the end of the 1st discharge cycle, respectively.

accepted line of argument that the change of discharge parameters is caused by a reduction of the free electron density n_e which is in turn caused by the charge up of the nanoparticle ensemble one comes to the conclusion that the nanoparticles do not reduce n_e significantly during phase I. To verify this conclusion the time evolution of n_e has been determined with a multipole resonance probe (MRP) (cf. subsection 3.3.4). A representative measurement is depicted in figure 4.16. As can be seen from figure 4.16 the MRP measurements do indicate a decrease of n_e during phase I. However, it remains unclear whether this decrease of n_e is solely caused by the nanoparticle ensemble or whether the discharge is still stabilizing. One needs to take into account that the matching network was not pre-matched during the MRP measurements. This means that there is a much longer delay between ignition of the discharge and stabilization of the discharge parameters. For example, ϕ_{RF} reaches stable values within 400 ms after ignition (cf. figure 4.15) with pre-matching. Without pre-matching the discharge needs approximately 5 s to stabilize. This can explain why n_e shows relatively strong fluctuations directly after the ignition. Furthermore, this raises the question

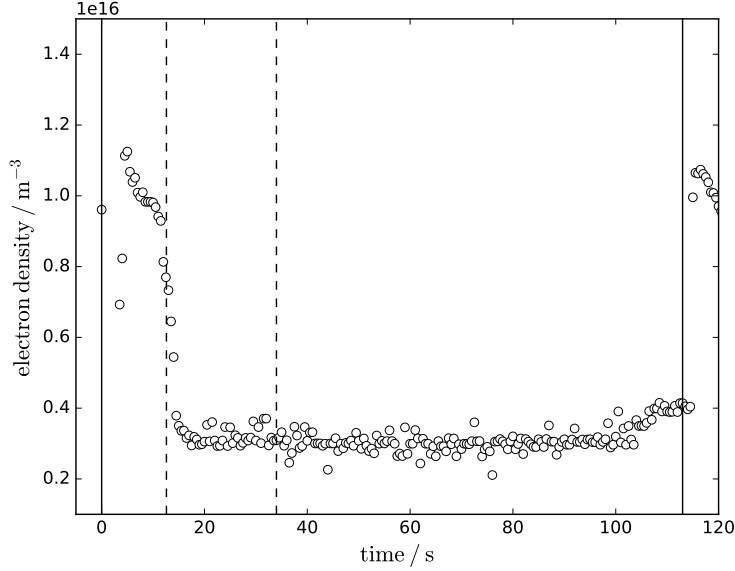


Figure 4.16: Time evolution of the free electron density n_e during the 1st discharge cycle as measured by a multipole resonance probe (MRP). The dashed vertical lines indicate the end of phase I and II, respectively. The solid black lines mark the ignition of the discharge at $t = 0$ s and the end of the 1st discharge cycle, respectively.

whether the observed decrease of ϕ_{RF} is only an artifact. But even in case of a pre-matched network discharge parameters related to the plasma chemistry do not reach stable values during phase I. Figure 4.17 shows the time evolution of the process pressure p_{Pi} as measured by a Pirani gauge. In contrast to the absolute pressure p_{abs} inside the plasma reactor, which is held constant at $p_{\text{abs}} = 8$ Pa by the butterfly valve, p_{Pi} continuously decreases during phase I. As the Pirani gauge is sensitive to changes in the process gas composition one can conclude that the composition of the process gas does not stabilize in phase I. In fact, it does not stabilize throughout the entire discharge cycle. Taking into account that the discharge does not stabilize entirely in phase I it seems likely that the observed decrease of n_e is not entirely caused by the nanoparticle ensemble. Furthermore, microwave interferometry measurements performed in the 'Pequod'-reactor do not indicate that there is a significant reduction of n_e during phase I [91]. Although these measurements were carried out with a different electrode and process parameters, the observed cyclic behaviour of the discharge parameters is quite similar. Summing up all the arguments given above one can conclude that even if n_e

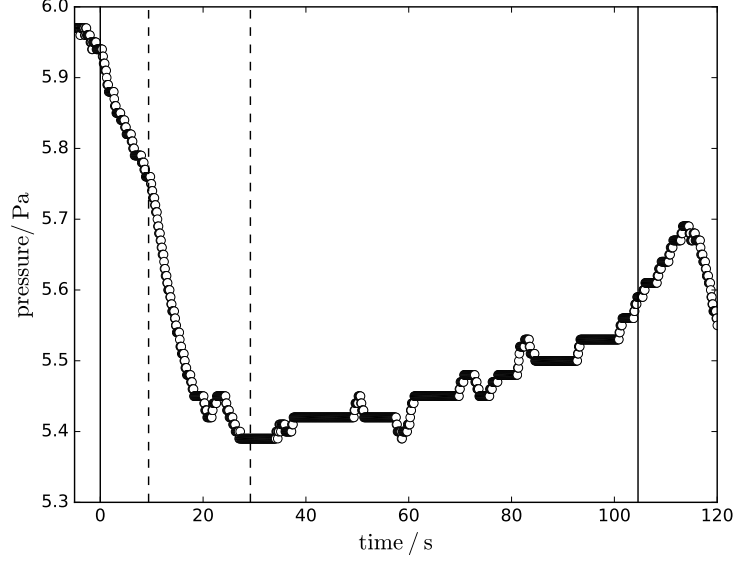


Figure 4.17: Time evolution of the process pressure p_{Pi} as measured by a Pirani gauge during the 1st discharge cycle. The dashed vertical lines indicate the end of phase I and II, respectively. The solid black lines mark the ignition of the discharge at $t = 0$ s and the end of the 1st discharge cycle, respectively.

decreases during phase I it is not dominated by the charging of nanoparticles forming in the discharge. Besides, one can also conclude that the charging of nanoparticles becomes dominant at the transition from phase I to phase II.

However, the latter conclusion is in conflict with the available data if one assumes that the charging of nanoparticles is described by the OML-theory (cf. section 2.3). The charge Q_p of a particle with diameter d_p at floating potential Φ_f is given by (2.13). But, for the discharge parameters of interest the Debye-length λ_D is of the order of several μm . Thus, (2.13) reduces to

$$Q_p \approx 2\pi\epsilon_0 d_p \Phi_f. \quad (4.2)$$

The OML-theory predicts that the floating potential is independent of d_p . The charge of the particle is a linear function of d_p . Therefore, the fast decrease of n_e at the transition between phase I and II requires a fast increase of the particle diameter, the number of particles, or both quantities. But, there is no experimental evidence that either increases significantly. As can be seen from figure 4.14 $\langle d_{1,1} \rangle$ increases steadily in this transition region. Moreover, at the transition between phase I and II the collected nanoparticles have mean diameters of $\langle d_{1,1} \rangle \approx 20$ nm. For the discharge parameters given

in table 4.2 a particle of such size can acquire a maximum charge, i. e. $P \ll 1$, of $49e$ (cf. section 2.3). The charging of the nanoparticle ensemble is not limited by the particle size. The collection experiments do not provide any information about the number of particles N_p dispersed in the discharge. But, a fast increase of N_p appears implausible. There is no model that would explain the spontaneous formation of nanoparticles with a diameter of $\langle d_{1,1} \rangle \approx 20$ nm. Of course, one could assume that a second particle generation with a very large number of small particles forms. This should result in a bimodal size distribution of the collected nanoparticles. But, this is not observed. If N_p does not increase and the charge per particle Q_p is not limited by its size there must be a mechanism limiting Q_p that is not included in the OML-theory. It is well known that the temperature T_p of nanoparticles growing in low pressure discharges can be substantially larger than the temperature T_n of the neutral gas [119–121]. These high particle temperatures have already been used to explain the core-shell structure of nanoparticles growing in Ar – C₂H₂ discharges [122, 123]. *Bronholdt et al.* developed a physisorption inspired model for the charging of particles that takes into account the particle temperature T_p [124, 125]. They also found a reasonable agreement between their model and experiments investigating the charging of microparticles [45]. Inspired by this approach the OML-theory presented in section 2.3 will be extended to include the particle temperature T_p . The following derivation does not include the Havnes effect, i.e. $P \ll 1$. Including it would only complicate the derived equations and would not provide any further insights into the effect of T_p . Following the approach by *Bronholdt et al.* the current balance towards the particle is extended by a current

$$I_d = Q_p \frac{k_B T_p}{h} \exp\left(-\frac{E_s}{k_B T_p}\right) \quad (4.3)$$

that describes the desorption of electrons from the particle. k_B and h are Boltzmann and Planck constant, respectively. The desorption current is based on the absolute reaction rate theory [126]. It is assumed that all electrons making up the charge Q_p need to overcome the energy barrier E_s to desorb from the particle. Furthermore, it is assumed that the electrons adsorbed onto the particle are in thermal equilibrium with it. In addition, it is assumed that all electrons and ions initially stick to the particle. The total current

$$I = I_e - I_d - I_i$$

towards the particle is then given by the sum of the desorption current I_d , the electron current I_e and the ion current I_i . The reader may now rightfully ask why the desorption of ions is not taken into account. Ions may desorb as

well from the particle before they are neutralized by an electron. But, due to the higher mobility of the electrons one can assume that the potential Φ of the particle is always negative with respect to the surrounding plasma. Thus, as soon as an ion desorbs from the particle it experiences an attractive force towards the particle. An ion would need to have a kinetic energy $E_{\text{kin}} \sim k_B T_p > |e\Phi|$ in order to leave the Debye-sphere around the particle. As $|e\Phi|$ is expected to be on the order of a few eV the probability of such a scenario is extremely small for reasonable values of T_p . The opposite is true for electrons as soon as they desorb they will be repelled by the negative particle potential Φ . In that sense the particle behaves similar to a negatively biased thermionic emitter in an electron gun. At the floating potential¹ Φ_f^D the total current towards the particle must vanish ($I(\Phi)_{\Phi=\Phi_f^D} = 0$). Taking the electron current

$$I_e = \frac{en_e \pi d_p^2}{4} \left(\frac{k_B T_e}{2\pi m_e} \right)^{1/2} \exp\left(\frac{e\Phi}{k_B T_e} \right) \quad (4.4)$$

and the ion current

$$I_i = \frac{en_e \pi d_p^2}{4} \left(\frac{k_B T_i}{2\pi m_i} \right)^{1/2} \left[1 - \frac{e\Phi}{k_B T_i} \right] \quad (4.5)$$

from the OML-theory the equilibrium condition for the floating potential is given by

$$\begin{aligned} \frac{en_e \pi d_p^2}{4} \left(\frac{k_B T_i}{2\pi m_i} \right)^{1/2} \left[1 - \frac{e\Phi_f^D}{k_B T_i} \right] = \\ \frac{en_e \pi d_p^2}{4} \left(\frac{k_B T_e}{2\pi m_e} \right)^{1/2} \exp\left(\frac{e\Phi_f^D}{k_B T_e} \right) - q_d \frac{k_B T_p}{h} \exp\left(-\frac{E_s}{k_B T_p} \right). \end{aligned}$$

Inserting relation (4.2) one finds, after a few rearrangements, a final expression

$$\begin{aligned} \left(\frac{k_B T_i}{2\pi m_i} \right)^{1/2} \left[1 - \frac{e\Phi_f^D}{k_B T_i} \right] = \\ \left(\frac{k_B T_e}{2\pi m_e} \right)^{1/2} \exp\left(\frac{e\Phi_f^D}{k_B T_e} \right) - \frac{8\epsilon_0 k_B T_p}{en_e h d_p} \Phi_f^D \exp\left(-\frac{E_s}{k_B T_p} \right) \end{aligned} \quad (4.6)$$

defining the floating potential. Although relation (4.6) certainly lacks the elegance of (2.17) it can be solved in the same. However, this requires the

¹The superscripts D, S and OML are added to the floating potential to discriminate between floating potentials derived from different models.

knowledge of the particle temperature T_p , the particle diameter d_p , and the adsorption energy E_s . While information about d_p can be gained from figure 4.14, neither T_p nor E_s are accessible with the experimental setup in its current state. Nevertheless one can gain some insight by simulations. Although 'simulations' sounds certainly more fancy than the actual simulations are. The 'simulations' just calculate the floating potential based on the model developed above by solving equation (4.6) with a standard numerical method. Figure 4.18 shows the results of these simulations. The floating potential Φ_f^D is normalized by the floating potential Φ_f^{OML} as defined by the OML-theory. For the simulations the discharge parameters given in table 4.2 were used. For the free electron density a value of $n_e \approx 1.34 \times 10^{16} \text{ m}^{-3}$ was assumed.

Table 4.2: Estimated discharge parameters for the simulation of the floating potential.

Parameter	Symbol	Value
ion temperature	T_i	0.026 eV
ion mass	m_i	40 u
electron temperature	T_e	3 eV
free electron density	n_e	$1.3 \times 10^{16} \text{ m}^{-3}$

This is equal to the mean free electron density of a pure Ar-discharge run at a pressure of 8 Pa and an RF-power of 10 W in the 'Pequod'-reactor. Figure 4.18 contains a lot of important information. In the case of a small adsorption energy E_s the floating potential will be very small, even at room temperature. This means that the particle does not charge up at all. Electrons desorb much faster from the particle than it takes to replenish the charge by the electron current from the discharge. If the electrons adsorb strongly to the particle Φ_f^D is equal to the floating potential predicted by the OML-theory for any reasonable particle temperature T_p . Desorption of such strongly bound electrons is an unimportant process. For the given parameters this requires $E_s \approx 2 \text{ eV}$. This appears plausible. The work function W of most materials lies in the range of a few eV. The work function of a:C-H films prepared by ion beam deposition is of the order of 4 eV but can increase to that of graphite ($W \approx 4.7 \text{ eV}$) upon annealing at high temperatures [127]. If the particle temperature were so large that these strongly bound electrons would desorb, thermionic emission would need to be taken into account as well, provided that the particle does not decompose at such high temperatures. This means that for the given parameters the adsorption energy should lie in the range of $E_s \approx 0.5 - 1.2 \text{ eV}$ to influence the floating

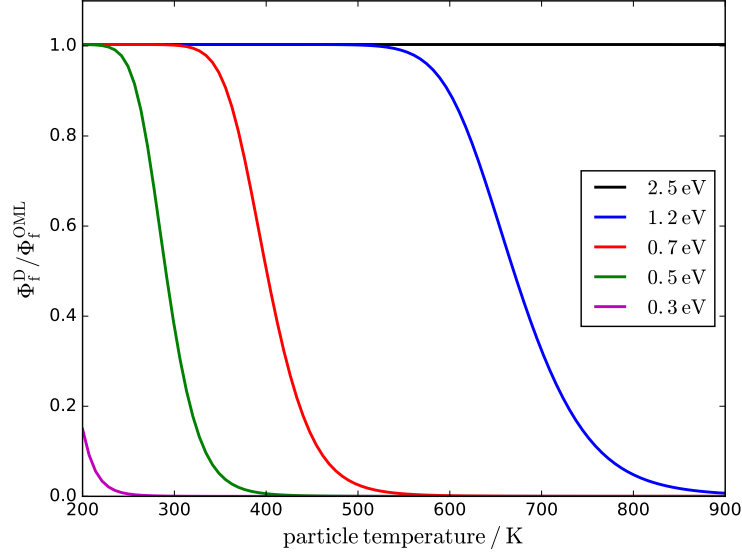


Figure 4.18: Plot of the floating potential Φ_f^D (cf. (4.6)) normalized by the floating potential Φ_f^{OML} as defined by the OML-theory as a function of the particle temperature T_p . The curves were calculated with the discharge parameters from table 4.2 and an electron density of $n_e \approx 1.34 \times 10^{16} \text{ m}^{-3}$ for a particle with diameter $d_p = 20 \text{ nm}$.

potential of the particle in a way that is compatible with the experimental data. That said, there is another effect that needs to be taken into account for small particles. Treating the particle again as a spherical capacitor, the magnitude E of the electrical field strength at its surface is given by

$$E = \frac{Q_p}{\pi \epsilon_0 d_p^2}.$$

Inserting the relation (4.2) between particle charge q_p and its floating potential Φ_f yields

$$E = \frac{2\Phi_f}{d_p}. \quad (4.7)$$

The OML-theory predicts that the floating potential is independent of the size of the particle. For the discharge parameters given in table 4.2 the floating potential amounts to $\Phi_f^{\text{OML}} \approx -7 \text{ V}$. For a particle with diameter $d_p = 20 \text{ nm}$ this translates into a field strength of $E \approx -7 \times 10^8 \text{ V/m}$. Such high field strengths are also used in high performance Schottky emission sources for state of the art electron microscopes. Thus, the lowering of the

adsorption energy E_s by the Schottky effect should be taken into account in the calculation of the desorption current. According to the theory of Schottky emission sources [86] the amount ΔW by which an energy barrier is reduced by an electrical field strength of magnitude $|E|$ is given by

$$\Delta W = \left(\frac{e^3 |E|}{4\pi\epsilon_0} \right)^{1/2}. \quad (4.8)$$

Inserting the relation between the particle potential Φ and the electrical field strength at the surface of the particle gives

$$\Delta W = \left(\frac{e^3 |\Phi|}{2\pi\epsilon_0 d_p} \right)^{1/2}. \quad (4.9)$$

Taking this reduction of the adsorption energy into account reaction (4.6) transforms into

$$\begin{aligned} \frac{8\epsilon_0 k_B T_p}{en_e h d_p} \Phi_f^S \exp\left(-\frac{E_s}{k_B T_p}\right) \exp\left(\left[-\frac{e^3 |\Phi_f^S|}{2\pi\epsilon_0 d_p}\right]^{1/2}\right) = \\ \left(\frac{k_B T_e}{2\pi m_e}\right)^{1/2} \exp\left(\frac{e\Phi_f^S}{k_B T_e}\right) - \left(\frac{k_B T_i}{2\pi m_i}\right)^{1/2} \left[1 - \frac{e\Phi_f^S}{k_B T_i}\right]. \end{aligned} \quad (4.10)$$

This relation self-consistently takes into account that the adsorption energy is lowered by the electrical field strength at the surface of the particle. Compared to (4.6) no new variables have been added. This means one can directly compare the results of simulations based on (4.6) and (4.10). Figure 4.19 shows the results for the simulation of the floating potential Φ_f^S . As expected, the Schottky effect shifts the region in which Φ_f^S is considerably reduced compared to the OML-theory to lower temperatures. Additionally, it substantially broadens the temperature range over which Φ_f^S changes. By including the Schottky effect the Φ_f^S is self-limiting its increase. A decrease of the desorption current by a decrease of the particle temperature T_p is compensated by a lowering of the threshold for desorption by the increasing electrical field strength which is in turn caused by an increase of Φ_f^S . The lowering of the threshold for desorption is also dependent on the diameter d_p of the particle. Simulations covering the influence of d_p on the floating potential for a particle temperature $T_p = 400$ K are summarized in figure 4.20. For a given temperature the floating potential increases as expected with increasing diameter. This increase with the particle diameter is stronger for larger adsorption energies E_s . However, the diameter range in which the floating potential is reduced shifts to lower values with increasing E_s . So,

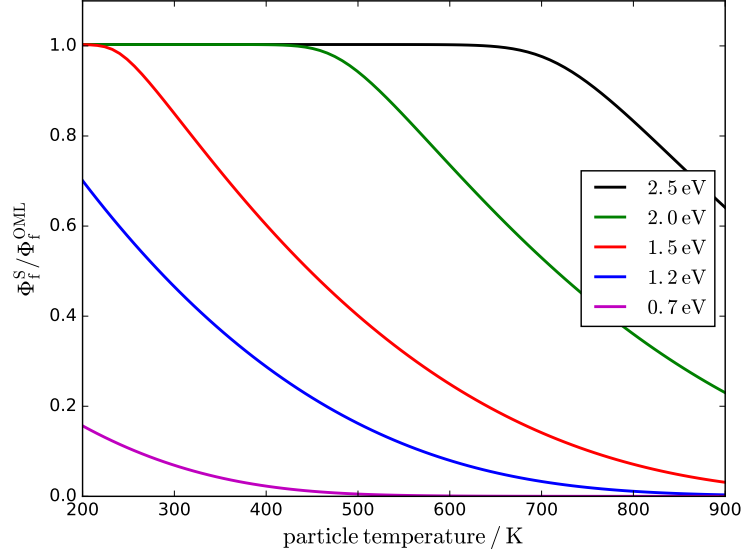


Figure 4.19: Plot of the floating potential Φ_f^S (cf. (4.10)) normalized by the floating potential Φ_f^{OML} as defined by the OML-theory as a function of the particle temperature T_p . The curves were calculated with the discharge parameters from table 4.2 and an electron density of $n_e \approx 1.34 \times 10^{16} \text{ m}^{-3}$ for a particle with diameter $d_p = 20 \text{ nm}$.

even if one includes the Schottky effect, the floating potential Φ_f is not affected by desorption of electrons if they strongly adsorb onto the particle. The simulations suggest (cf. figure 4.19 and 4.20) that for the given parameters this is the case for $E_s > 2.5 \text{ eV}$. This is already approaching the work functions W of emitters used in electron guns, like LaB_6 and ZrO (both 2.7 eV) [86]. This means that the electrical field strength E at the surface of a particle with such strongly adsorbed electrons is not reduced ($\Phi_f \approx \Phi_f^{\text{OML}}$) at low temperatures. This raises the question whether field emission needs to be taken into account. Field-emission sources in state of the art electron microscopes are operated at field strengths $|E| \approx 5 \times 10^9 \text{ V/m}$ [86]. A reasonable incorporation of field emission into the OML-theory is, unfortunately, beyond the scope of this work. Nonetheless, the effect on the floating potential should be similar to that of Schottky emission. The floating potential will be lower than predicted by the OML-theory and it will be a function of the particle diameter and the temperature, if a temperature dependent model of field emission is chosen. The model presented above has another crucial shortcoming. It is assumed that all quantities are continuous. How-

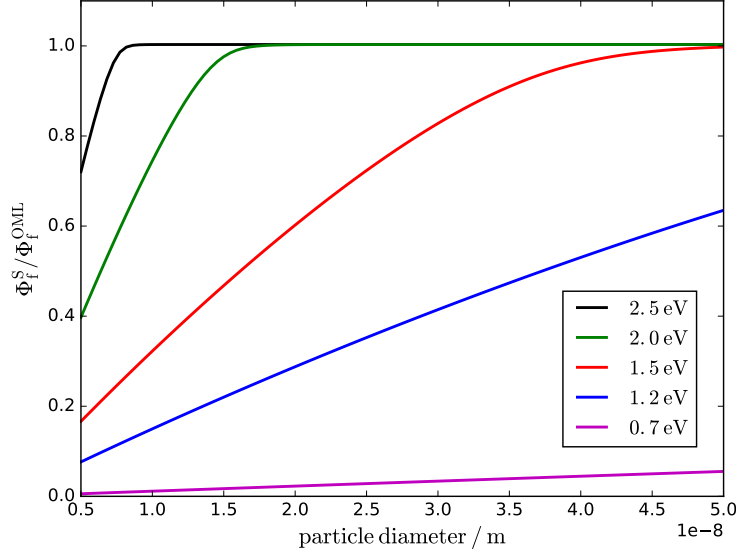


Figure 4.20: Plot of the floating potential Φ_f^S (cf. (4.10)) normalized by the floating potential Φ_f^{OML} as defined by the OML-theory as a function of the particle diameter d_p . The curves were calculated with the discharge parameters from table 4.2 and an electron density of $n_e \approx 1.34 \times 10^{16} \text{ m}^{-3}$ for a particle temperature $T_p = 400 \text{ K}$.

ever, this is not true. The currents flowing to and from the particle consist of charged particles, namely electrons and ions, that only carry a discrete number of elementary charges. Thus, the charge of the particle is also a discrete quantity. It can only change by a multiple of the elementary charge e . For a particle with a charge of several thousands of elementary charges this discreteness may not be very important. But for nanoparticles it is important. The number of charges per particle is small and thus a discrete change by one elementary charge will change the total charge of the particle significantly. As mentioned earlier, a particle with a diameter of 20 nm has only a charge of $Q_p \approx 49 e$, according to the OML-theory. A precise description of the charging process should therefore treat it as the discrete stochastic process that it is. Such a stochastic description of the charging process in dusty plasmas can be found in [128] by the interested reader.

Despite all the shortcomings of the model it provides a higher compatibility with the experimental data than the OML-theory. With a floating potential that is both dependent on the particle temperature T_p and the

diameter of the particle d_p the charge of the particle

$$Q_p \approx 2\pi\epsilon_0 d_p \Phi_f^S(d_p, T_p) \quad (4.11)$$

has become a non-linear function of d_p and T_p . Given that the adsorption energy E_s falls in the correct energy range this could explain the insignificant charging of particles during phase I and their rapid charging at the transition between phase I and II. A decrease of the particle temperature at the transition between phase I and II would support this interpretation.

As mentioned earlier, a measurement of T_p is not possible with the experimental setup. Thus, only indirect evidence for a high particle temperature can be provided. The shape of the collected nanoparticles suggests that the particle temperature is substantially larger than room temperature. As can be seen from SEM images the shape of collected nanoparticles can deviate from that of a perfect sphere. A representative SEM image is shown in figure 4.21. The shape of collected nanoparticles does not change on time

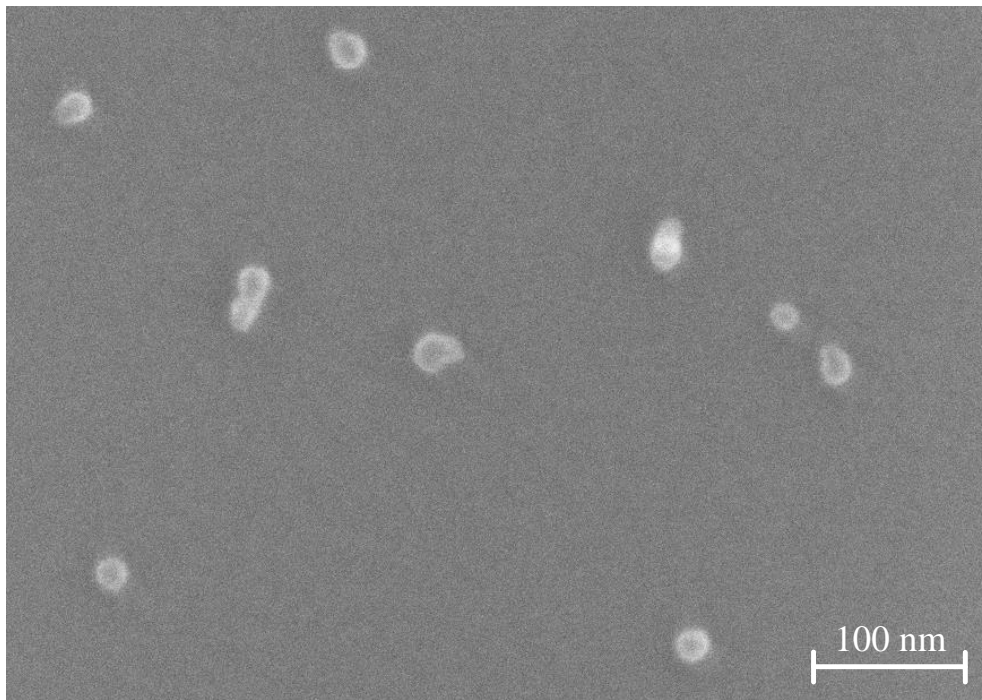


Figure 4.21: SEM image of nanoparticles collected 6 s after ignition from a discharge run at the standard process parameters.

scales that are relevant for their growth in the discharge. No change of the

particle shape can be detected during SEM-measurements, which take approximately 15 min for one sample. This is much longer than the length of one discharge cycle (≈ 100 s). This implies that, at room temperature, that mass transport by diffusion is so low that the particle is unable to reach its equilibrium shape, which is presumably a sphere. This is not unexpected because of the strong covalent bonds between the carbon atoms forming the particles. In fact, with a diffusion constant $D_0 \approx 10^{-4} \text{m}^2/\text{s}$ and an activation energy $E_a \approx 7$ eV [129] the self diffusion of carbon in graphite is negligibly small at room temperature. However, one has to take into account that the much faster surface diffusion is more important for nanoparticles due to the high surface-to-volume ratio. For example, the activation energy for bulk self diffusion in silicon is approximately 4.75 eV [130] whereas it is only approximately 0.67 eV for surface self diffusion on (001)-planes [131]. But, even if one takes into account a faster surface diffusion the diffusivity of the carbon atoms should be comparably low at room temperature due to the strong covalent bond between them. Furthermore, one needs to remember that the particles are subject to a constant flux of molecules to their surface. Thus, surface diffusion can only take place during a time scale that is comparable to the formation time of one monolayer. This means that particles growing in the discharge would be unable to coalesce if the particle temperature were close to room temperature. This does not seem to be true. Some of the particles shown in figure 4.21 are spherical whereas others have a more elongated shape. As surface deposition onto the particles is isotropic in the discharge, such an elongated shape can only be the result of agglomeration of particles. But, the agglomerates would consist of single particles if coalescence of the particles were prohibited by a low diffusivity. Nevertheless, the elongated particles appear to be the result of coalescence. For high resolution images of the coalescence of nanoparticles the interested reader may, for example, refer to [132]. This means that the particle temperature must be substantially larger than room temperature. Indeed, it must be so large that the coalescence can take place within a few seconds. Unfortunately, one can not draw any conclusions about the absolute value of T_p or its evolution during the discharge cycle from the arguments given above. Nonetheless, one can get an idea about the particle temperature from other experiments. An in-situ investigation of nanoparticles formed in a similar discharges with ellipsometry by *Hong et al.* showed that the optical properties of the particles at the beginning of their growth ($d_p \leq 50$ nm) are similar to that of graphite [122]. Similar results were obtained by *Kovacevic et al.* in a NEXAFS-study. Small particles ($d_p \leq 10$ nm) show a higher degree of sp^2 hybridization of the carbon atoms than larger particles [123]. According to annealing studies of a:C-H films, these films start to display graphite like properties if annealed above

900 K [133]. Thus, one can conjecture that the temperature of the smallest nanoparticles investigated in this work is at least 900 K. An attempt to verify the presence of a graphite like core inside the collected nanoparticles with EELS have been unsuccessful. Beam damage (cf. figure 4.22) rendered an analysis of the EELS data meaningless. However, EELS measurements with a specialized low-voltage TEM might be feasible [134]. One could even try to use tomographic measurements to obtain a 3D map of the ratio between σ - and π -bonds in the particles [135].

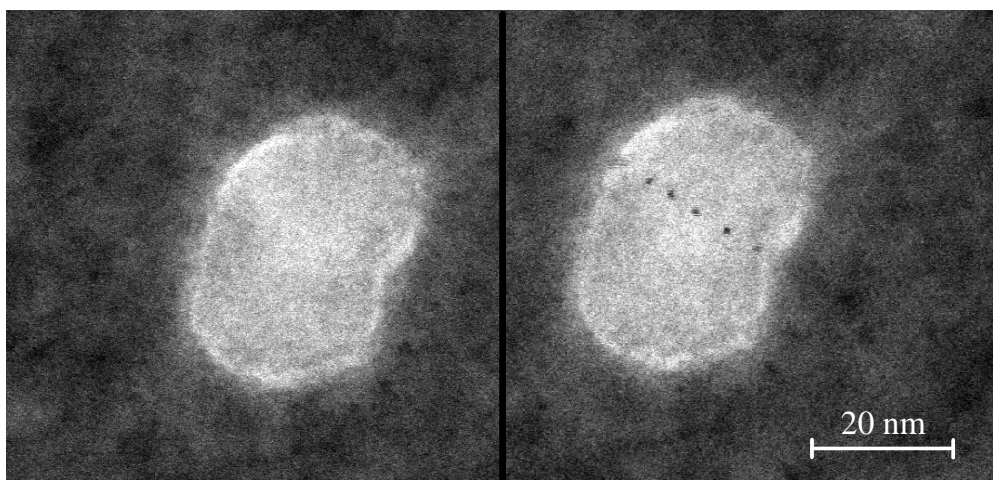


Figure 4.22: STEM images of a collected nanoparticle prior (LHS) and after EELS measurements at different positions (RHS). The formation of dark spots on the particle is the result of beam damage caused by the EELS measurements.

An experimental determination of the particle temperature is a formidable experimental challenge. As the particle temperature can not be measured directly, one can only determine the temperature by measuring a temperature dependent property of the particle. It has been demonstrated that the temperature of nanoparticles growing in reactive plasmas can be determined by measuring their thermal radiation. But, this required to heat the particles externally by a laser pulse to temperatures of 3000 K [136] or even evaporate the particles [137]. Such temperatures are presumably not reached by the particles if they are solely heated by the discharge. At least, there is no evidence in the recorded emission spectra suggesting otherwise. A more promising approach is the use of the temperature dependent emission from phosphor particles presented by *Maurer et al.* [138–140]. But, this approach needs to be extended from micro- to nanoparticles. Stability of the phos-

phor particles should not be an issue. Phosphors used for the investigation of thermal barrier coatings have demonstrated a reasonable performance at temperatures of up to 1200 K [141, 142]. An ex-situ production of such phosphor nanoparticles is certainly feasible. But, dispersing the nanoparticles in the discharge may be difficult if the particles form tightly bonded agglomerates. An in-situ production of the phosphor nanoparticles could circumvent this problem. One possibility would be to replace the showerhead by a gas aggregation cluster source [143, 144]. The phosphor nanoparticles formed in the cluster source would be directly injected into an RF discharge sustained by the lower electrode. Admittedly, the temperature of the phosphor particles may deviate from the temperature of the carbonaceous particles. But, one would at least get more detailed information of the net energy flux to such small particles. As any experimental approach will be challenging, simulations of the energy fluxes to and from the particles might be a more straightforward approach.

4.3.3 Detection of small nanoparticles

It has been reported that the amplitudes of the higher harmonics of RF-current or-voltage are a useful indicator for the onset of particle formation [50, 145]. *Boufendi et al.* reported the detection of particles with 3 nm diameter in an Ar – SiH₄ discharge by monitoring the time evolution of the 2nd harmonic of the RF-current. Monitoring the higher harmonics provided an earlier detection of nanoparticles than the phase angle ϕ_{RF} between the 1st harmonics of RF-current and- voltage [50]. Transferring this approach to the discharge investigated in this work has not been successful. The time evolution of the harmonics up to the 5th were recorded by the IV-probe. Although all recorded harmonics show changes during phase I, these changes are much smaller than the changes observed at the transition between phase I and II. Moreover, the changes are neither more significant than those of ϕ_{RF} nor can they be detected earlier. In addition, the amplitudes of the higher harmonics are much smaller than that of the 1st. The 1st harmonic (13.56 MHz) of the voltage amplitude reaches a maximum of $\hat{v}_1 \approx 140$ V. The 3rd harmonics (40.68 MHz) have the highest amplitudes of all recorded higher harmonics. The 3rd harmonic of the voltage amplitude reaches only a maximum value of $\hat{v}_3 \approx 1.3$ V. Detecting subtle changes of the higher harmonics is less reliable than for the 1st harmonic. It should be pointed out that in another study the 7th harmonic (94.92 MHz) of the voltage amplitude had the highest sensitivity of all harmonics to the presence of nanoparticles in the discharge [145]. Therefore, it cannot be ruled out that a harmonic higher than the 5th would be a better indicator for the onset of particle formation

than ϕ_{RF} in the case of the 'Pequod'-reactor.

The earliest detection of particles is provided by the UV/Vis-transmission spectroscopy. Figure 4.23 shows the time evolution of the transmission of light with wavelengths of 250 nm, 532 nm, and 633 nm through the discharge. The transmission at all wavelengths is approximately 100 % before

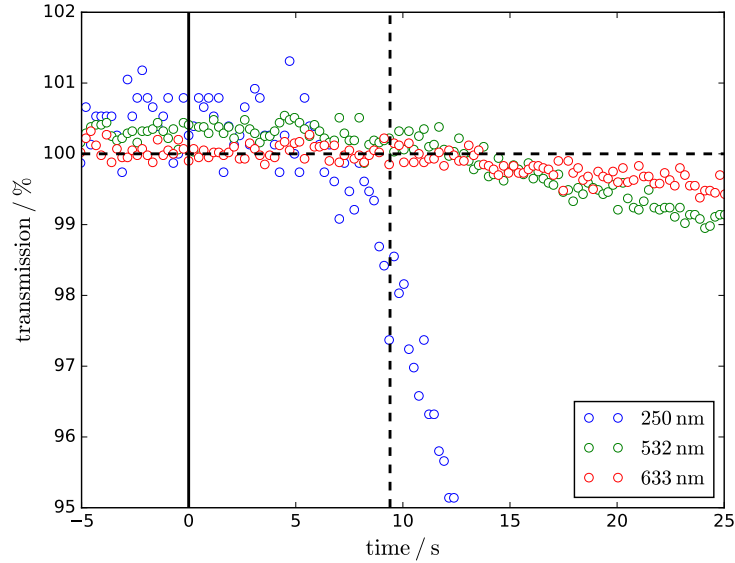


Figure 4.23: Time evolution of the transmission of light with wavelengths of 250 nm, 532 nm, and 633 nm through the discharge. The solid vertical line marks the ignition of the discharge at $t = 0$ s. The dashed vertical line marks the end of phase I. The dashed horizontal indicates a transmission of 100 %.

the ignition of the discharge. That the transmission at 250 nm and 532 nm is slightly higher than 100 % can be attributed to a small drift of the recorded spectra relative to the reference spectrum. Using the transmission T_{532} at 532 nm or the transmission T_{633} at 633 nm, particles are detectable approximately 13 s after the ignition of the discharge. At this point phase II of the discharge cycle has already begun. The particles growing in the discharge have mean diameters in the range of $35 \text{ nm} \leq \langle d_p \rangle \leq 45 \text{ nm}$ (cf. figure 4.14). The transmission in the UV-range is a more sensitive indicator of particle formation. Particles with mean diameters as small as $15 \text{ nm} \leq \langle d_p \rangle \leq 20 \text{ nm}$ can be detected approximately 7 s after the ignition of the discharge by using the transmission T_{250} at 250 nm.

Performing spectroscopic transmission measurements has of course the big advantage that one obtains a very robust database, which does not only

contain information about the size of the particles but also their distribution in the discharge. The prospects of this approach will be outlined in subsection 4.5. If only the presence of nanoparticles in the discharge needs to be detected, one could simply perform transmission measurements in a very narrow wavelength range. For example, replacing the broadband source of the spectrometer (cf. section 3.3.5) with a stable, high intensity UV-LED and the spectrometer with an avalanche photodetector should improve the sensitivity of the transmission measurements. If one replaces the light source, one should verify that the transmission measurements do not affect the particle formation. The time evolution of ϕ_{RF} does not suggest that this is the case with the transmission setup used in this work but it has been reported that irradiating a similar discharge with pulses from a UV laser drastically affected the particle formation [146]. In that case the transmission measurements would be invasive, which would eliminate one of its biggest advantages. By increasing the sensitivity of the transmission measurements it is probably possible to extend the detection limit to $d_p \leq 10$ nm [147]. This would put the transmission measurements on par with more sophisticated optical diagnostics like polarization-sensitive laser-light-scattering (PSLLS) [148] or laser induced particle explosive evaporation (LIPEE) [137]. But, it is unlikely that the transmission measurements will be able to detect particles that contain less than 200 Si atoms, which corresponds roughly to $d_p \leq 2$ nm, as has been demonstrated with a photoemission method [149].

4.4 Electron Depletion (Phase II)

4.4.1 Increase of the Degree of Excitation

As has been outlined in section 4.3.2, the strong changes of key discharge parameters at the onset of phase II is linked to a reduction of the free electron density n_e (cf. figure 4.16). Thus, it may appear somewhat contradictory that the emission intensity of the discharge increases simultaneously. Emission spectra recorded at the beginning and the end of phase II can be found in figure 4.24. Unfortunately, the resolution of the spectrometer is not better

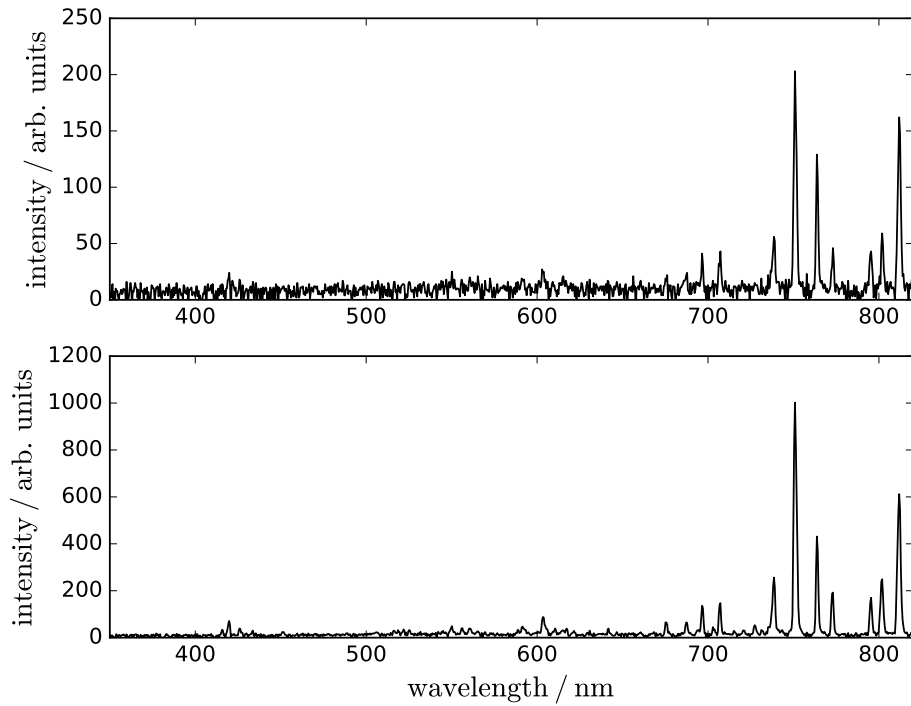


Figure 4.24: Emission spectra recorded at the beginning of phase II (upper graph) and at the end of phase II (lower graph).

than 1.5 nm (cf 3.3.2). Some of the observed emission lines could be the overlap of two adjacent lines. For example two emission lines of metastable Argon (ArI) are located at 772.38 nm ($2p_1 - 1s_5$) and 772.42 ($2p_2 - 1s_3$), respectively [150]. Nevertheless, table 4.3 summarises the attempt to assign the corresponding transition to each of the observed emission lines. If the observed emission line could be the overlap of several emission lines, the transition with the highest transition probability A_{ki} from the upper level

k to the lower level l was assigned to the observed line. Emission lines at wavelengths smaller than 697 nm are not included in table 4.3 because the time evolution of their intensity cannot be tracked throughout the entire discharge cycle due to a low signal-to-noise ration during phase I of the discharge cycle.

Table 4.3: Observed emission lines and the transitions assigned to them. The energy of the upper and lower level E_k and E_l , respectively, the transition probability A_{kl} from the upper to the lower level, and the emission lines associated with the transitions were taken from [150]. The Paschen notation for the transitions was adapted from [151].

wavelength		transition	A_{kl} s^{-1}	E_k eV	E_l eV
observed nm	assigned nm				
697.0	696.54	$2p_2 - 1s_5$	6.4×10^6	13.328	11.548
707.2	706.72	$2p_3 - 1s_5$	3.8×10^6	13.302	11.548
738.6	738.40	$2p_3 - 1s_4$	8.5×10^6	13.302	11.624
750.9	750.39	$2p_1 - 1s_2$	4.4×10^7	13.480	11.828
763.7	763.51	$2p_6 - 1s_5$	2.5×10^7	13.172	11.548
773.1	772.42	$2p_2 - 1s_3$	1.2×10^7	13.328	11.723
795.4	794.82	$2p_4 - 1s_3$	1.9×10^7	13.283	11.723
801.9	801.48	$2p_8 - 1s_5$	9.3×10^6	13.095	11.548
811.8	811.53	$2p_9 - 1s_5$	3.3×10^7	13.076	11.548

All of the observed emission lines originate from the relaxation of metastable Ar. The emission line observed at 750.9 nm has the highest intensity of all emission lines throughout the discharge cycles. Moreover, its intensity $I_{750.9}$ shows the most pronounced increase during phase II of the discharge cycles. The time evolution of the normalised intensity $I_{750.9,n}$ of the emission line observed at 750.9 nm can be found in figure 4.25. The intensity was normalised to the intensity directly after ignition. In addition to $I_{750.9,n}$ the time evolution of the normalised intensity of a few other emission lines selected from table 4.3 are shown in figure 4.25. The data of the other emission lines in table 4.3 show a similar behaviour as the data depicted in 4.25 and are not included for the sake of clarity. Whereas $I_{750.9,n}$ is almost constant during phase I, it rapidly increases during phase II and reaches its maximum at the end of phase II. During phase III $I_{750.9,n}$ decreases continuously. But there are subtle differences between the emission lines. This appears to be especially true for the time evolution of the normalised intensity $I_{763.7,n}$ of the

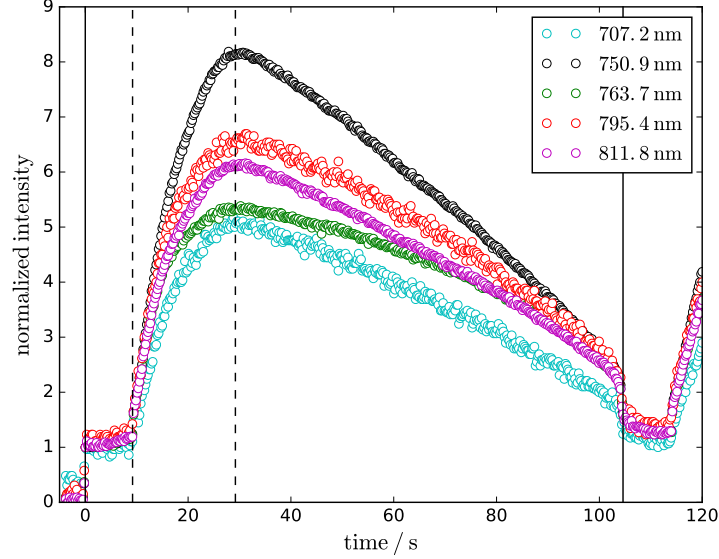


Figure 4.25: Time evolution of the normalised intensity of a few emission lines during the 1st discharge cycle. The intensity was normalised to the intensity directly after ignition. The dashed vertical lines indicate the end of phase I and II, respectively. The solid black lines mark the ignition of the discharge at $t = 0$ s and the end of the 1st discharge cycle, respectively.

emission line observed at 763.7 nm. Yet, it is not surprising that such subtle differences can be observed. It has been outlined in section 2.4.2 that for each metastable level different paths for population and depopulation exist. Each path will be affected in a different way by a change of the discharge parameters.

Neglecting these subtle differences, the increase of the intensity of the emission lines does indicate that the degree of excitation of the plasma increases during phase II. As mentioned earlier, this might not be expected because n_e decreases substantially at least at the beginning of phase II (cf. figure 4.16). But, it has been argued in other works that the reduction of n_e can be outweighed by an increase of the electron temperature T_e , cf. for example [52, 145, 152]. For example, if the electron energy distribution function (EEDF) can be described by a Maxwell-Boltzmann distribution, an increase of T_e from 3 eV to 3.5 eV raises the proportion of electrons with a kinetic energy sufficient to excite an Ar atom from the ground state to the $2p_1$ state (≈ 13.5 eV [150]) by a factor of 1.8. Unfortunately, it is difficult to access T_e experimentally and only a few measurements of T_e in nanoparti-

cle forming plasmas have been reported [153, 154]. Moreover, it is not even clear whether the EEDF of such plasmas is well described by simple distributions, like the Maxwell-Boltzmann distribution, that can be characterized by a single electron temperature [155].

Before an explanation for the increase of T_e will be presented it will be outlined why the measurements of n_e with the MRP are probably affected by an artifact in phase II. At beginning of phase II the electron density drops significantly (cf. figure 4.16), which has been interpreted as a rapid charging of the nanoparticle ensemble after reaching a critical size in section 4.3.2. Shortly after the beginning of phase II n_e reaches a constant value and stays at this level for most of the remaining part of the discharge cycle. A slight increase of n_e can only be observed at the end of phase III before it jumps back to a high value after the end of the discharge cycle. Qualitatively similar results were obtained in experiments, in which n_e was measured with microwave interferometry (MWI) by *Wegner et al.* [91]. During those experiments the 'Peqoud'-reactor was operated with a different electrode system but the time evolution of the self-bias voltage V_{SB} follows the same pattern as that of the phase angle ϕ_{RF} between the 1st harmonics of RF-current and voltage shown in figure 4.15. In another study [49] it has been shown that the time evolution of V_{SB} and ϕ_{RF} follows similar patterns, at least for parameters that are of interest for the discussion in this work. Furthermore, the light emission from the discharge was measured with a photodiode by *Wegner et al.*. The time evolution of the emission intensity is also similar to that shown in figure 4.25. In the work by *Wegner et al.* it has been argued that n_e drops below the detection limit shortly after the beginning of phase II and stays below the detection limit until the end of the discharge cycle. That would explain why discharge parameters like the self-bias voltage and the light emission change although n_e appears to stay constant. The constant level of n_e during the better part of phase II and III is an artifact caused by the detection limit of the MWI setup. The reader may now consider to reject this interpretation because measurements with an independent method, i.e. the MRP measurements, seem to confirm that n_e stays indeed constant after the initial drop at the beginning of phase II. But, there are two arguments for the conjecture that the MRP measurements are affected by an artifact as well. However, it is not the same artifact. According to the MRP measurements n_e drops to values in the range of $2 - 5 \times 10^{15} \text{ m}^{-3}$. These values lie well above the detection limit of the MRP, which is of the order of $5 \times 10^{14} \text{ m}^{-3}$. One argument for the interpretation as an artifact is the same as for the MWI measurements. A scenario in which important discharge parameters change (cf. figures 4.15, 4.17, and 4.25) although n_e stays constant seems to be quite unrealistic. The free electron density affects and is itself

affected by many parameters. It is especially unrealistic that this behaviour is observed for a wide range of process parameters. Figure 4.26 contains the data of three MRP measurements of n_e , which were performed at different RF-power levels. All other process parameters were equal to the standard process parameters (cf. table 4.1). Although the time evolution of n_e during

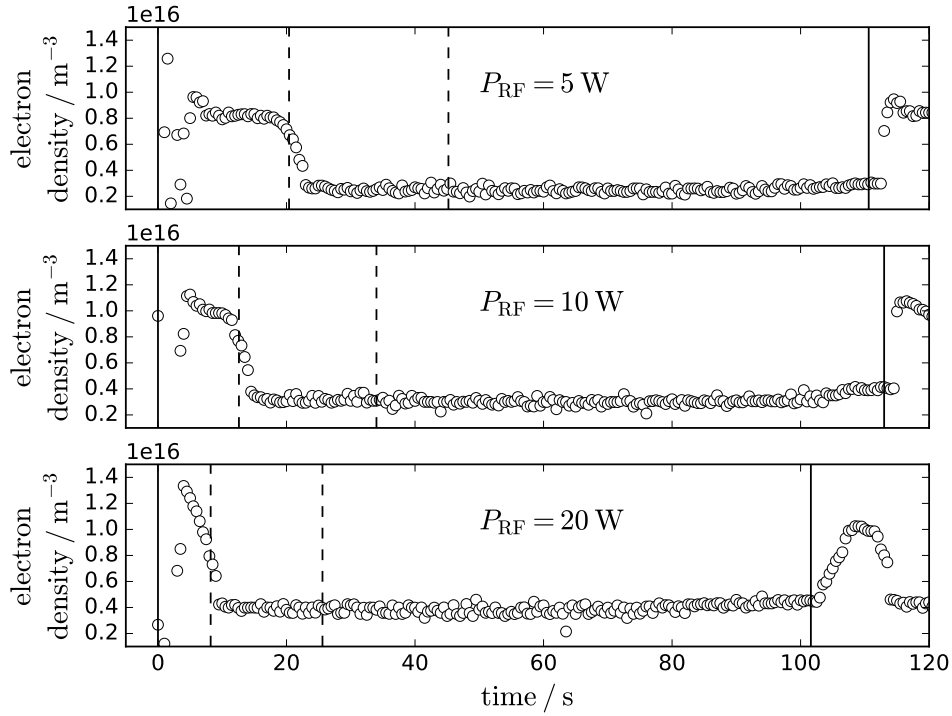


Figure 4.26: Time evolution of the free electron density n_e at three different RF-power levels P_{RF} during the 1st discharge cycle. The dashed vertical lines indicate the end of phase I and II, respectively. The solid black lines mark the ignition of the discharge at $t = 0$ s and the end of the 1st discharge cycle, respectively.

phase I differs for the different power levels, the time evolution during phase II and III is qualitatively the same. After an initial drop at the beginning of phase II the free electron density stays constant. Slight increases of n_e can only be observed at the end of phase III. Another argument for interpreting the constant level of n_e as an artifact is the probe character of the MRP measurements. Like all probe techniques it will inevitably affect the discharge. It is well known that objects that have a negative potential with respect to the plasma potential Φ_p are surrounded by voids [156–158] if they

are immersed in particle containing discharges. This is true for intentionally negatively biased objects as well as objects on the floating potential Φ_f . The MRP is not intentionally biased but is surrounded by a dielectric tube (cf. section 3.3.4) that will charge up to the floating potential. If indeed a void is formed around the MRP, this will affect the measurements of n_e . The free electron density that is determined by the MRP measurements is an averaged value. In a very simple approximation the volume probed by the MRP with its HF field is a sphere with a radius of the order of a few millimetres [159]. Because the MRP is measuring field strength averaged values and the field strength decays with increasing distance from the probe, the volume elements closest to the probe dominate the averaging. Thus, the free electron density measured by the MRP is likely dominated by the free electron density in the void formed around the probe. Unfortunately, the free electron density inside the void is not known. Furthermore, the spatial distribution of n_e inside the void could be quite complex. Like around any object inside the discharge that is not at Φ_p , a space charge sheath will form around the probe (cf. section 2.1). But the structure of the sheath could be affected by the presence of the nanoparticles in the discharge. In principal, the negatively charged nanoparticles should behave like negative ions with a large charge and a very large mass. Therefore, one can speculate that the structure of the sheath around the probe has some of the features observed for electronegative discharges. For example, for certain conditions the sheath in an electronegative discharges can show a triple layer structure [160]. A possible configuration of the sheath structure surrounding the MRP could be a nanoparticle loaded region with a low n_e , followed by a nanoparticle-free layer, in which n_e is larger (cf. figure 4.27). The final layer would be an electron depletion layer, which is the actual sheath in the conventional sheath models. Depending on the particular details of the sheath structure, it could explain the observed behaviour of n_e during phase II and III. After the nanoparticles permanently charge up negatively at the beginning of phase II a void forms around the MRP. The value of n_e determined by the MRP is dominated by the spatial distribution of n_e , i.e. the sheath structure, inside the void. This could result in a value of n_e that is larger than that in the nanoparticle loaded areas of the discharge $n_{e,p}$ but smaller than the free electron density in the pristine discharge. If a further decrease of $n_{e,p}$ does not have a strong influence on the sheath structure inside the void, n_e should stay constant until the void collapses, which is expected to happen when the nanoparticles leave the discharge at the end of phase III, i.e. the end of the discharge cycle. This is of course a highly speculative model and would need to be verified like the presence of a void surrounding the MRP. The presence of the void could be verified in the same way as other voids in

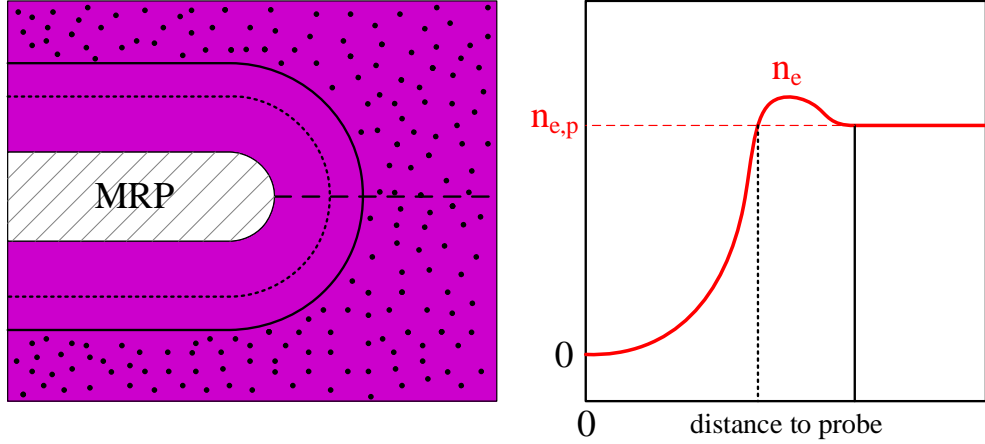


Figure 4.27: Schematic drawing of a potential sheath structure around the MRP. The graph on the right-hand side shows the free electron density n_e along a section through the sheath indicated by the dashed line in the sketch on left-hand side. The solid and dotted line indicate the boundaries of the different layers in the sheath. The dashed red line in the graph marks the free electron density $n_{e,p}$ in the nanoparticle loaded part of the discharge.

the discharge by illuminating the discharge with a laser fan and recording the light scattered by the nanoparticles. An experimental verification of the sheath structure inside the void is at best challenging and should rather be verified by simulations or theoretical modeling.

Because of the arguments given above, for the rest of the discussion it will be assumed that the time evolution of n_e measured by the MRP does not properly reflect the real time evolution of n_e after the onset of phase II. Based on the time evolution of the intensity of the recorded emission lines it will be assumed that n_e follows the following pattern. It decreases throughout phase II and reaches a minimum at the end of phase II. During phase III it increases monotonically until it goes back to its initial value after the end of the discharge cycle. This means that the maximum degree of excitation of the discharge at the end of phase II coincides with the minimum of n_e .

Although it is dissatisfying that, like the previous MWI measurements, the experiments described in this work do not provide an unambiguous description of the time evolution of n_e during the 1st discharge cycle, it once more illustrates very effectively why a multidagnostic approach is required to investigate nanoparticle forming reactive plasmas. Even using two diagnostics as different as MWI and MRP was not sufficient to obtain unambiguous

results.

4.4.2 The Influence of Coulomb Collisions

An increase of T_e can be explained by an increase of the power dissipated in the plasma bulk [161]. As the decrease of the phase angle ϕ_{RF} at the beginning of phase II indicates, the discharge changes from an almost purely capacitive to a more resistive behaviour. This can be explained by an increase of the resistance R_b of the plasma bulk. As will be discussed in the next section, this does not mean that the sheath capacitance does not change as well. Based on (2.8) both the free electron density n_e and the electron collision frequency ν_e^m for momentum loss can contribute to the increase of R_b . The influence of ν_e^m will be discussed first. An increase of R_b can be explained by an increase of ν_e^m . The electron collision frequency for momentum loss can be described as the sum

$$\nu_e^m = \sum_j \nu_{ej}^m \quad (4.12)$$

of all momentum loss collision frequencies ν_{ej}^m associated with a particular type of collision partner j . The individual ν_{ej}^m can be expressed as

$$\nu_{ej}^m = \int_0^\infty dv_e \sigma_{ej}^m(v_e) v_e f_v(v_e) n_j \quad (4.13)$$

with the momentum loss cross section σ_{ej}^m for the specific collision, the electron velocity v_e , the velocity distribution function f_v and the number density n_j of the collision partner j . In other publications it has been suggested that collisions between electrons and nanoparticles could significantly increase ν_e^m [50, 52]. At first, this is an intriguing conclusion. The nanoparticles result in some form of 'impure' plasma bulk. One of the most basic concepts of conductivity is that 'impurities' result in a decreased conductivity. However, it has to be kept in mind that both the density of the 'impurities' as well as their properties eventually determine whether they have any relevant impact on the conductivity. This can be exemplified by a very simple estimation. The mean thermal velocity $v_{e,\text{th}}$ of electrons obeying a Maxwell-Boltzmann distribution with an electron temperature $T_e = 3\text{ eV}$ is $v_{e,\text{th}} \approx 1.2 \times 10^6 \text{ m s}^{-1}$. The momentum loss cross section σ_{ep}^m for the collision of an electron with an uncharged particle can be approximated by the geometric cross section of the nanoparticle $\sigma_p = \pi d_p^2/4$. The electron can be treated as a point particle and its kinetic energy is not so high that it can fly through the particle, like the high energy electrons in a transmission electron microscope (TEM). With a nanoparticle number density $n_p = 5 \times 10^{13} \text{ m}^{-3}$ and a

particle diameter $d_p = 61$ nm one finds an electron-nanoparticle momentum loss collision frequency of $\nu_{ep}^m = \sigma_{ep}^m v_{e,th} n_p \approx 1.7 \times 10^5$ Hz. This is much lower than the electron-Ar momentum loss collision frequency ν_{eAr}^m . The electron-Ar momentum loss collision cross section σ_{eAr}^m at this $v_{e,th}$ is $\sigma_{eAr}^m \approx 5.7 \times 10^{-20}$ m² [162]. The Ar number density n_{Ar} at a pressure of $p = 8$ Pa is $n_{Ar} \approx 2 \times 10^{21}$ m⁻³ assuming Maxwell-Boltzmann behaviour and a neutral gas temperature $T_n = 300$ K. This results in $\nu_{eAr}^m \approx 1.3 \times 10^8$ Hz. Uncharged nanoparticles do not contribute significantly to the electron momentum loss collision frequency ν_e^m . The contribution of ν_{ep}^m corresponds to an increase of n_{Ar} by less than 0.2 %. The fluctuations of n_{Ar} will have a greater impact on ν_e^m . The reader may rightfully criticise that in the back-of-the-envelope calculation above the differentiation between momentum loss collisions and collisions in general is sloppy, but this should only be a minor issue.

That uncharged nanoparticles do not significantly contribute to ν_e^m does not mean that this is true for charged nanoparticles. The electrons will be deflected in the electrical field surrounding the charged particle. Because the charged nanoparticle is massive compared to the electron, the electron will not lose energy in this process. The absolute value of its momentum $|\vec{p}_e|$ will not be changed either, but the change of the direction of \vec{p}_e by the deflection of the electron represents a momentum loss. This scenario is referred to as Coulomb collision. The Coulomb collision cross section σ_{eC}^m of an electron with a charged nanoparticle can be described by

$$\sigma_{eC}^m = \frac{1}{8\pi} \left(\frac{eQ_p}{\epsilon_0 m_e v_e^2} \right)^2 \ln \left[1 + \left(\frac{\epsilon_0 m_e v_e^2 \lambda_D}{eQ_p} \right)^2 \right] \quad (4.14)$$

with the elementary charge e , the free electron mass m_e , the electron velocity v_e , the particle charge Q_p , the Debye-length λ_D , and the permittivity of free space ϵ_0 [163]. However, equation (4.14) was originally derived for the Coulomb collisions between electrons and ions. Both particles are treated as point particles. Whereas the electron can still be treated as a point particle, the charged nanoparticle has a finite size that cannot be neglected. One must therefore expect that equation (4.14) underestimates σ_{eC}^m if it falls below the geometric cross section σ_p of the nanoparticle. This would be especially important for electrons with high velocities, i.e. large kinetic energy, because of the v_e^{-4} dependence in equation (4.14). Inspired by the work of *Khrapak et al.* [163], simulations of the Coulomb collision between electrons and negatively charged nanoparticles were performed. The simulations are admittedly rather simplistic but provide valuable insights about the parameter range in which equation (4.14) can be used to describe the Coulomb

collision of electrons and negatively charged nanoparticles and whether these Coulomb collisions can have a significant influence on ν_e^m . The Coulomb collision cross section σ_{eC}^m is obtained by simulating the trajectory of an electron in a region around a negatively charged nanoparticle for different impact parameters b (cf. figure 4.28). Due to the spherical symmetry of the problem it is sufficient to simulate the electron trajectory in a square 2d plane. Ini-

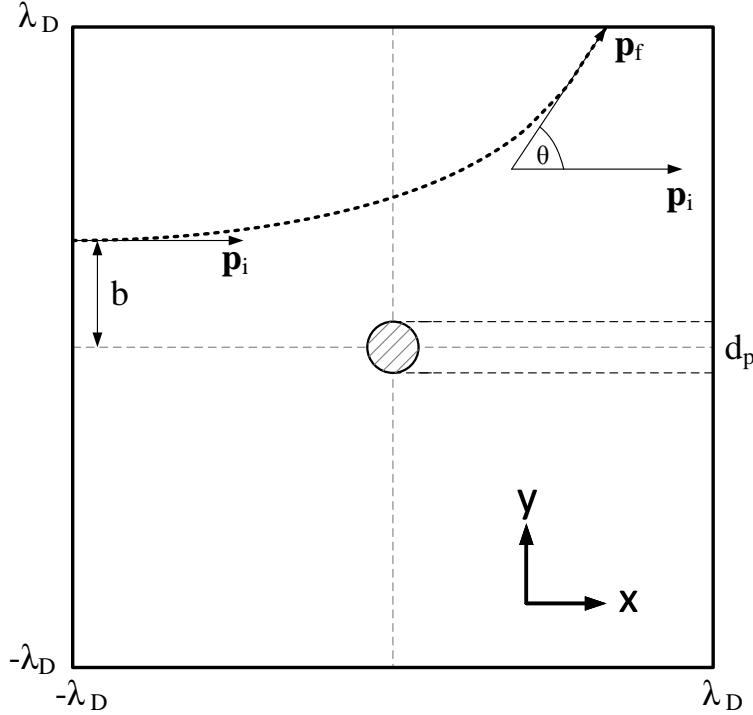


Figure 4.28: Sketch of the simulation area used for simulating the Coulomb collision of an electron with a negatively charged nanoparticle with diameter p . The dotted line indicates a potential electron trajectory. The deflection angle is obtained as the scalar product of the initial and the final electron momentum vector \vec{p}_i and \vec{p}_f , respectively.

tially, the electron has only a momentum component in the x -direction. If the electron has left the simulation area, its deflection angle θ is calculated as the scalar product between its initial and final momentum vector \vec{p}_i and \vec{p}_f . The Coulomb collision cross section σ_{eC}^m can then be calculated [163] by using the relationship

$$\sigma_{eC}^m = 2\pi \int_0^\infty db [1 - \cos\{\theta(b)\}] b \approx 2\pi \int_0^{l_s} db [1 - \cos\{\theta(b)\}] b. \quad (4.15)$$

The upper limit l_S in equation (4.15) is one half of the side length of the square simulation area. The trajectory of the electron is calculated in the framework of Hamiltonian mechanics.

The assumptions made in the simulation are listed below.

- The simulation area is a square with a side length of 2 times the Debye-length λ_D (cf. figure 4.28). At distances larger than λ_D the interaction potential between the electron and the negatively charged particle will decay quickly. Especially, if the interaction potential were described by a screened potential, like the Yukawa potential. Moreover, it has to be taken into account that in the discharge investigated in this work the nanoparticle number density n_p is relatively high. Distributing the nanoparticles of an ensemble with $n_p = 5 \times 10^{13} \text{ m}^{-3}$ on a simple cubic lattice, the inter-particle distance is $\lambda_p = n_p^{-1/3} \approx 27 \text{ }\mu\text{m}$. It is of the same order as the one expected for λ_D . If the electron moves farther away from one particle than λ_D , it will likely be affected by the electrical fields surrounding other particles. Accounting for these effects is beyond the scope of this work.
- The bare Coulomb potential is used to describe the electrostatic interaction between the negatively charged nanoparticle and the electron. In general, one would need to use a screened potential, like the Yukawa potential, to account for the screening effect of the plasma background. But, it is not clear which screened potential accurately describes the potential of the negatively charged nanoparticles. At a floating potential Φ_f^{OML} of several volts, the linearisation of the perturbation of the charge density in the derivation of the Yukawa potential should be inaccurate. Therefore, the potential should not decay as fast as expected. But *Lampe et al.* found that the potential of negatively charged particles in a plasma can indeed be described by a Yukawa potential up to distance of $5\lambda_D$ from the particle surface [164]. However, in that case the floating potential Φ_f of the particle is not as large as Φ_f^{OML} . They have attributed this behaviour to the trapping of ions by the negatively charged nanoparticles. Because it is not clear how the potential is described accurately, the bare Coulomb potential was chosen as it represents an upper limit. The particle charge Q_p is calculated with equation (4.2) under the assumption $\Phi_f = \Phi_f^{\text{OML}}$. In that case Q_p also represents an upper limit.
- The electron does not lose kinetic energy during the Coulomb collision. The mass m_p of the particle is much larger than that of the electron, i.e. $m_p/m_e > 1 \times 10^8 \gg 1$. The electron does not transfer any significant

amount of energy to the particle. The centre of masses coincides with the centre of the particle, i.e. the centre of the simulation area (cf. figure 4.28).

- An intersection of the electron trajectory with the geometric cross section σ_p of the particle is treated as a specular reflection of the electron at the particle surface. The electron does not lose energy in this process. This is of course a rather crude assumption. But, it is not clear how the electron interacts with the charged particle upon impingement. The electron may stick to the particle and thus contribute to the particle charge q_p , it might lose some kinetic energy in an inelastic collision or it might be diffusely scattered without the loss of kinetic energy. In addition, to describe the impingement of the electron on the charged particle one would need to describe the charge density on the surface of the particle in detail. Such a detailed description of the impingement process is beyond the scope of this work.
- The Debye-length λ_D is approximated by the ion Debye-length $\lambda_{D,i} \approx \lambda_D$. Due to the high ratio $T_e/T_i \approx 115$ of ion temperature T_i and electron temperature T_e , the Debye-length will be dominated by the ionic contribution.

The parameters that were used for the simulations are summarised in table 4.4. Selected results of the simulations can be found in figures 4.29 to 4.31.

Table 4.4: Parameters for the simulation of Coulomb collisions

Parameter	Symbol	Value
ion density	n_i	$1.3 \times 10^{16} \text{ m}^{-3}$
ion temperature	T_i	0.026 eV
ion mass	m_i	40 u
electron temperature	T_e	3 eV
Debye-length	λ_D	10.3 μm
floating potential	Φ_f	-7.06 V

One can draw two important conclusions from the data in figures 4.29 to 4.31. Firstly, the simulated data properly approaches the expected values at high and low v_e . At high v_e it is expected that σ_{eC}^m approaches the geometric cross section of the nanoparticle. Electrons with such high v_e are not very strongly deflected by electrical field surrounding the nanoparticle. If one were modelling the direct collision of the electron with the nanoparticle in

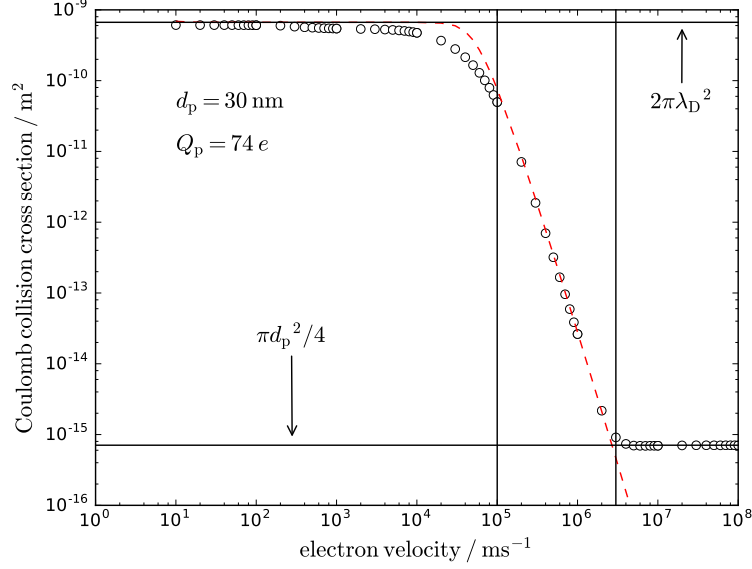


Figure 4.29: Simulated Coulomb collision cross section σ_{eC}^m as a function of the electron velocity v_e . The simulation was performed with the parameters in table 4.4 for a particle diameter $d_p = 30$ nm and a particle charge $q_p = 74 e$. The red dashed line are values calculated with equation (4.14) for the same parameters. The solid vertical lines mark $v_e = 1 \times 10^5$ ms^{-1} and $v_e = 3 \times 10^6$ ms^{-1} . The horizontal solid lines mark the expected asymptotic values of the simulated data.

a different way, one would of course expect a different or no asymptotic value. At high v_e the conventional model for Coulomb collisions (cf. (4.14)) drastically underestimates σ_{eC}^m , because it does not account for the finite size of the nanoparticle. At low v_e , the data for the conventional model as well as the simulated data approach the same asymptotic value. The data based on the conventional model approaches the asymptotic value faster than the simulated data. The asymptotic value reached at low v_e is $\sigma_{eC}^m = 2\pi\lambda_D^2$. This 2 times the area of a circle with a radius equal to the Debye-length. Electrons with low v_e have a very low kinetic energy and are almost instantly repelled by the electrical field surrounding the negatively charged particle once they have entered the simulation area. Due to the symmetry of the problem σ_{eC}^m is defined by a circular area. The additional factor of 2 is a consequence of the large deflection angles θ . As the electrons are almost instantly repelled, the deflections angles will be $\theta \approx 180^\circ$. A deflection angle of $\theta \approx 180^\circ$ means that the electron momentum has changed by approximately $2|\vec{p}_e|$.

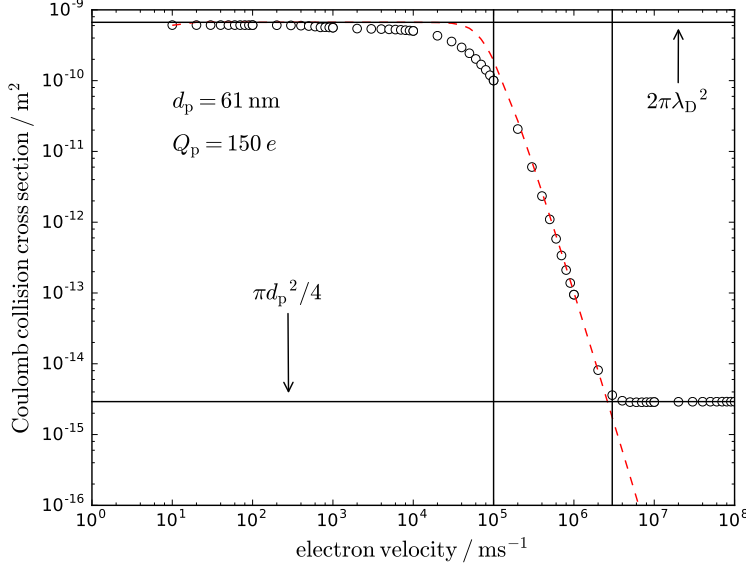


Figure 4.30: Simulated Coulomb collision cross section σ_{eC}^m as a function of the electron velocity v_e . The simulation was performed with the parameters in table 4.4 for a particle diameter $d_p = 61$ nm and a particle charge $q_p = 150 e$. The red dashed line are values calculated with equation (4.14) for the same parameters. The solid vertical lines mark $v_e = 1 \times 10^5$ ms $^{-1}$ and $v_e = 3 \times 10^6$ ms $^{-1}$. The horizontal solid lines mark the expected asymptotic values of the simulated data.

This results in the additional factor 2. One can compare the situation to a ping pong ball bouncing off a massive wall. Secondly, it appears that in the velocity regime that is of interest for the discharge investigated in this work and similar discharges the simulated data does not deviate dramatically from the data based on equation (4.14). The region of interest is enclosed by two solid vertical lines in figures 4.29 to 4.31. They enclose the velocity range 1×10^5 ms $^{-1} \leq v_e \leq 3 \times 10^6$ ms $^{-1}$. If the electrons were obeying a Maxwell-Boltzmann distribution with an electron temperature $T_e = 3$ eV, less than 0.1 % of all electrons were lying outside of this region on each side. In addition, an electron velocity of $v_e = 3 \times 10^6$ ms $^{-1}$ corresponds to a kinetic energy $E_{\text{kin},e} = 25.6$ eV. This is well above the excitation energies of Ar (cf. table 4.3) and the ionization energy of Ar $E_{i,\text{Ar}} = 15.76$ eV [150]. Thus, one should be able to use equation (4.14) instead of detailed simulations to get reasonable estimates of σ_{eC}^m . Probably this approach will be sufficient for most calculations as some of the input parameters need to be estimated

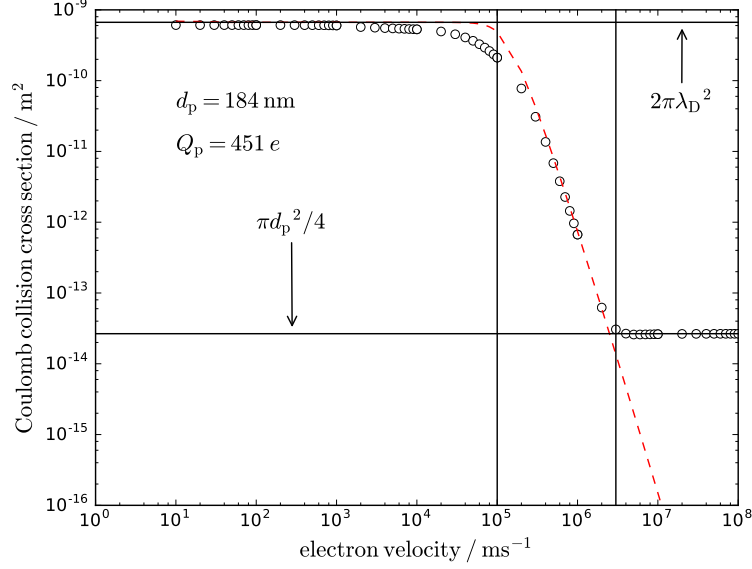


Figure 4.31: Simulated Coulomb collision cross section σ_{eC}^m as a function of the electron velocity v_e . The simulation was performed with the parameters in table 4.4 for a particle diameter $d_p = 184$ nm and a particle charge $q_p = 451 e$. The red dashed line are values calculated with equation (4.14) for the same parameters. The solid vertical lines mark $v_e = 1 \times 10^5$ ms $^{-1}$ and $v_e = 3 \times 10^6$ ms $^{-1}$. The horizontal solid lines mark the expected asymptotic values of the simulated data.

anyway. The possibility to use (4.14) instead of detailed simulations is also advantageous for simulations that model the complete discharge. It is not necessary to simulate the Coulomb collisions themselves but one can simply use the cross section given by equation(4.14).

Coming back to the original question whether Coulomb collisions with negatively charged nanoparticles affect ν_e^m significantly, the question remains difficult to answer. Using equation (4.13) in combination with equation (4.14) one can get a reasonable estimate of ν_{eC}^m . It is assumed that f_v is described by a Maxwell-Boltzmann distribution with an electron temperature $T_e = 3$ eV. With $n_p = 5 \times 10^{13}$ m $^{-3}$, $Q_p = 150e$, and $\lambda_D = 10.3 \mu\text{m}$ one finds $\nu_{eC}^m \approx 0.13 \times 10^8$ Hz. The integration was performed in the limits of $v_e = 1 \times 10^5$ ms $^{-1}$ to $v_e = 3 \times 10^6$ ms $^{-1}$. The value obtained for ν_{eC}^m falls at least in the same range as $\nu_{eAr}^m \approx 2 \times 10^8$ Hz, which was estimated at the beginning of the subsection. The contribution of ν_{eC}^m corresponds to an increase of n_{Ar} by approximately 5 %. This could be called significant, but one should keep

in mind that this values represents an upper limit and could in reality be substantially lower. Another issue is that σ_{eC}^m depends strongly on v_e . One can therefore in general not assume that the EEDF is unaffected by the Coulomb collisions. Even if the initial EEDF were known, one would need to perform a self-consistent calculation. It could well be the case that the rise of T_e indicated by the increased degree of excitation (cf. section 4.4.1) during phase II has a greater effect on ν_e^m than the contribution from ν_{eC}^m . While σ_{eC}^m decreases with increasing v_e , the electron-Ar momentum loss collision cross section σ_{eAr}^m increases with v_e until $v_e \approx 2 \times 10^6 \text{ ms}^{-1}$. Thus, a rise of T_e should increase ν_{eAr}^m . Taking all the aforementioned arguments together, one cannot outright reject the conjecture that Coulomb collisions of electrons with the negatively charged nanoparticles have a significant, i.e. measurable, effect on ν_e^m . But, it appears plausible to assume that it is not a dominant effect. In the future this issue will need to be addressed by more advanced and self-consistent simulations.

Even if the Coulomb collisions have a significant effect on ν_e^m , the increase is expected to be a few percent. This increase of ν_e^m has only a minor effect on ρ_b compared with the drop of the free electron density n_e . The MRP measurements show that n_e drops by at least a factor 3 after the onset of phase II (cf. figure 4.26). Following the conclusion at the end of the preceding subsection that the MRP measurements are affected by an artifact and n_e reaches its minimum at the end of phase II, an even larger drop of n_e is expected. The increase of ρ_b and the associated increase of the plasma bulk resistance R_b are dominated by the drop of n_e during phase II.

4.4.3 Dynamics of the Sheath

The sheath at the driven electrode also shows an interesting dynamic during the discharge cycle. While one can observe the expected thick high voltage sheath above the driven electrode directly after ignition and during phase I, the sheath thickness d_s decreases substantially during phase II and reaches its minimum thickness at the end of phase II (cf. figure 4.32). During phase III the sheath thickness increases continuously until it has reached its original thickness at the end of the discharge cycle. An attempt to determine

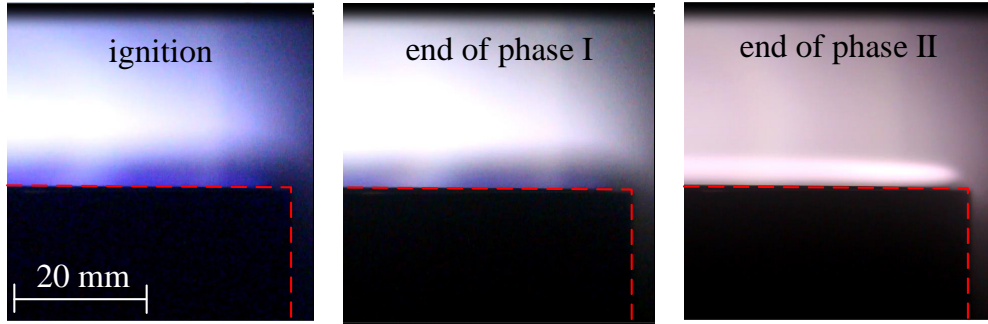


Figure 4.32: Images of the driven electrode at selected points during the discharge cycle. The images show one half of the driven electrode. The red dashed lines mark the surface of the electrode. The scale bar is valid for all three images.

the exact sheath thickness and its time evolution have not been performed. Although it is known, that, in general, the regions with the highest emission intensity are located close to the sheath edge if the discharge is operating in the α – regime (cf. section 2.1), these regions are rather diffuse and it is difficult to derive the exact position of the sheath edge from spatial profiles of the emission intensity.

A decrease of the sheath thickness affects the capacitance C_s of the sheath and thus its impedance $|Z_s|$. As the capacitance scales with the inverse of d_s , its capacitance C_s will increase. The opposite is true for $|Z_s|$. It decreases with decreasing d_s . The increase of C_s in a similar discharge has been quantified by *Wattiaux et al.* [54]. The decrease of $|Z_s|$ during phase II is reflected in the time evolution of the discharge impedance $|Z_d|$, its real part $\text{Re}\{Z_d\}$, and its imaginary part $\text{Im}\{Z_d\}$. The time evolution of all three values is shown in figure 4.33. As expected from the discussion in the previous section, $\text{Re}\{Z_d\}$ increases during phase II because the resistance R_b (cf. subsection 4.4.2) of the plasma bulk increases. However, the impedance

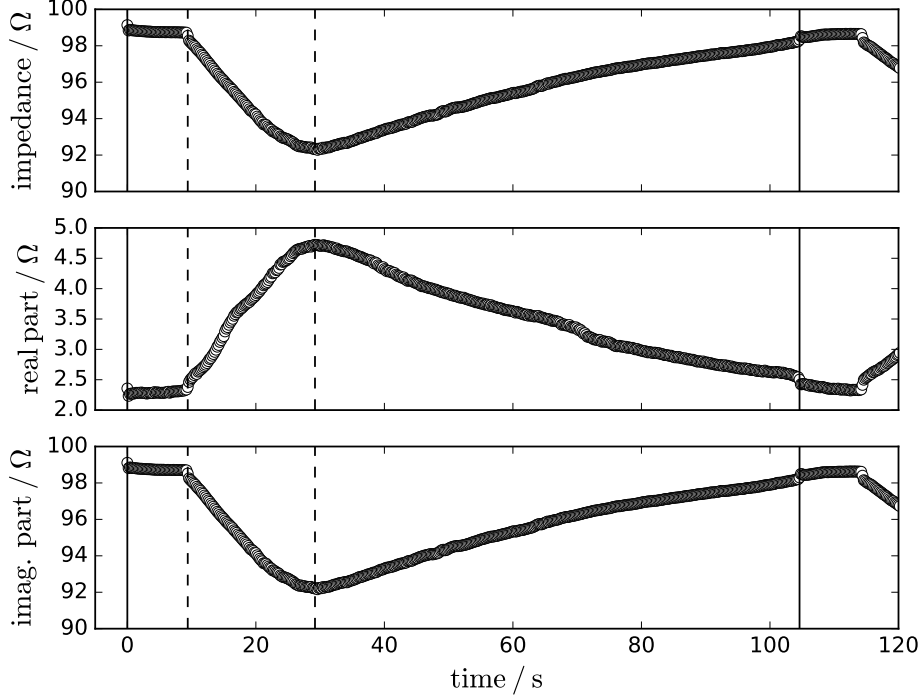


Figure 4.33: Time evolution of the discharge impedance $|Z_d|$, its real part $\text{Re}\{Z_d\}$, and its imaginary part $\text{Im}\{Z_d\}$ during the 1st discharge cycle. The dashed vertical lines indicate the end of phase I and II, respectively. The solid black lines mark the ignition of the discharge at $t = 0$ s and the end of the 1st discharge cycle, respectively.

of the discharge $|Z_d|$ decreases during phase II. The decrease of the sheath impedance $|Z_s|$, which is connected in series with R_b outweighs the increase of R_b . Although the decrease of $\text{Im}\{Z_d\}$ indicates the decrease of $|Z_s|$, the imaginary part $\text{Im}\{Z_d\}$ of the discharge impedance and $|Z_s|$ are not equivalent. Besides $|Z_s|$, other parasitic elements contribute to $\text{Im}\{Z_d\}$. To obtain the actual time evolution of $|Z_s|$ one would need to develop an equivalent circuit of the discharge that contains all relevant parasitic elements and determine the impedance of these elements (cf. for example [54, 165]).

Although the effect of the decreasing sheath thickness on $|Z_d|$ is relatively clear, it is unclear what exactly causes the decrease of d_s . Of course, it is clear that the presence of the nanoparticle ensemble in the discharge is the root cause, but it remains unclear how the nanoparticle ensemble causes the decrease of d_s . Based on the conclusions of the preceding sections, it seems

that the presence of the nanoparticle ensemble only affects the sheath after the charge up of the nanoparticles at the onset of phase II. *Wattiaux et al.* have argued that the charged nanoparticles exert an electrostatic force on the sheath, thereby compressing it [54]. That would implicate that the presence of the nanoparticle ensemble itself causes the decrease of d_s . In other words, even if all other properties of the discharge were completely unaffected by the presence of the nanoparticle ensemble, d_s would decrease. But, it has to be taken into account that the charge up of the nanoparticles at the onset of phase II drastically affects other properties of the discharge as well. Independent of the particular details of the model used to describe the sheath, the thickness of the sheath is given by the relation between the voltage drop V_s across the sheath and the current density j_s flowing through the sheath. From the Child-Langmuir law (cf. equation (2.7)) one would expect

$$d_s \propto \left(\frac{V_s^{3/2}}{j_i} \right)^{1/2}$$

with the current density j_s flowing through the sheath equal to the ion current density j_i flowing through the sheath. One cannot expect that either j_s or V_s are unaffected by the change of other discharge parameters like the free electron density n_e or the electron temperature T_e during phase II. Unfortunately neither V_s nor j_i can be measured by the diagnostics attached to the 'Pequod'-reactor. Even if V_s nor j_i were known, it would be unclear whether any of the sheath models mentioned in section 2.1 can be applied to estimate the sheath thickness. These models were developed for electropositive discharges. As mentioned earlier, the negatively charged nanoparticles should behave like massive negative ions. The presence of the negatively charged nanoparticle ensemble should change the behaviour of the discharge in the direction of an electronegative discharge. It is known that the sheath in electronegative discharge is, by and large, thinner than in electropositive discharge at comparable conditions [166]. Moreover, it has been demonstrated that upon admission of electron attaching gases like BCl_3 the sheath thickness of Ar discharges, which are electropositive, decreases [167]. Therefore, it is probably the best to interpret the decrease of d_s as a self-consistent adjustment to a change of the other discharge parameters and the relations that define d_s . Trying to find a single cause for the decrease of d_s becomes pointless in that case.

In addition to the sheath thickness, the spatial distribution of the emission intensity in the discharge changes. During phase I the region with the highest emission intensity is a diffuse region above the sheath. This diffuse region has also an inhomogeneous spatial distribution. Its vertical extension is largest

in the centre of the electrode and decreases with increasing distance from the rotational symmetry axis of the electrode. This changes after the onset of phase II. Simultaneously to the decrease of the sheath thickness the region with the highest emission intensity collapses into a sheath-like region. This sheath-like region appears to have a quite homogenous vertical extension across the electrode. Only at the edge of the electrode decreases the vertical extension of this sheath-like region. The formation of a region with high emission intensity in the plasma bulk could not be observed during phase II. This was quite unexpected. The model developed by *Bouchoule et al.* predicts that a rapid change of the discharge parameters indicates the so called $\alpha - \gamma'$ transition [39]. Although the discharge investigated in this work does show an increase of the emission intensity during the $\alpha - \gamma'$ transition, which has been observed in other systems as well, [39, 57, 168, 169], the observed spatial profile of the emission intensity does not fit to the expected one. The $\alpha - \gamma'$ transition is named after the conventional $\alpha - \gamma$ transition (cf. section 2.1) because the emission profiles before and after the transition have the same features for both transitions. In the α -regime the emission intensity is highest close to the sheath edges whereas it is low in the plasma bulk. In the γ -regime the emission intensity can have local maxima at the sheath edges but the global maximum of the emission intensity is observed in the centre of the plasma bulk. As mentioned above, a region with high emission intensity in the centre of the plasma bulk was not observed during phase II. In several other studies the emission profile typical for the γ -regime has been observed [56, 116, 161]. The presence of this region with high emission intensity in the plasma bulk has been linked to the formation of a void inside the plasma bulk [56, 105]. The conditions inside the void are different from the conditions in the nanoparticle loaded regions surrounding it and result in a higher emission intensity. This could explain why the observed emission profile differs from the expected profile. The discharges for which the emission profile typical for the γ -regime have been observed were symmetric discharges, whereas the discharge investigated in this work is asymmetric. Although there is evidence that a void forms in the discharge (cf. section 4.2), it is unclear whether it has already formed at the onset of phase II. Furthermore, it is unclear whether the conditions inside of voids formed in asymmetric or symmetric discharges differ. Nevertheless, one could still refer to the drastic changes of the discharge parameters at the onset of phase II as $\alpha - \gamma'$ transition to keep a notation that is consistent with other relevant studies.

The change of the spatial profile of the emission intensity also indicates a shift of the regions in which excitation of Ar takes place. The emission of the discharge is dominated by emission lines originating from the relaxation

of metastable Ar (ArI) (cf. section 4.4.1). The regions of the discharge with high emission intensity correspond to regions with a high number density n_{ArI} of metastable Ar. During phase I the region with the highest emission intensity and thus the highest n_{ArI} is a diffuse region adjacent to the sheath. As mentioned above, this is the emission profile expected for the α -regime of discharge operation. In the α -regime the electrons are mainly heated by the wave-riding mechanism (cf. section 2.1) in the region of the breathing sheath. Excitation of Ar will take place within a few times the electron mean free path l_e around the sheath. The mean free path for excitation l_e^{ex} of electrons that are important for the excitation of metastable states can be estimated as follows. For the sake of simplicity only the direct excitation of the metastable 2p states from the ground state is considered. The number density of Argon atoms is $n_{\text{Ar}} \approx 1.9 \times 10^{21} \text{ m}^{-3}$ at a pressure of $p = 8 \text{ Pa}$, a neutral gas temperature of $T_n = 300 \text{ K}$, and assuming ideal gas behaviour. The energy levels of the 2p states lie in the range of 13 eV to 13.5 eV. (cf. table 4.3). The electrons need a minimum velocity $v_e \approx 2.2 \times 10^6 \text{ m s}^{-1}$ to excite these states directly. At this velocity the total cross section for electron-Ar collisions is $\sigma_{e\text{Ar}}^{\text{tot}} \approx 2.3 \times 10^{-19} \text{ m}^2$ [170]. With these values the electron mean free path can be estimated as $l_e^{\text{ex}} = (n_{\text{Ar}} \sigma_{e\text{Ar}}^{\text{tot}})^{-1} \approx 2.3 \times 10^{-3} \text{ m}$. Thus, the expected extension of the region with a high metastable number density n_{ArI} and correspondingly high emission intensity agrees well with the extension of the high emission intensity region observed during phase I (cf. figure 4.32). Although one cannot directly conclude that ionization takes predominantly place in this region as well, because the observed emission lines only originate from metastable Ar, it is likely that the discharge is sustained by ionization in this region. This is expected for a discharge operating in the α -regime.

After the $\alpha - \gamma'$ transition at the onset of phase II, the discharge is probably sustained by a different mechanism than the wave-riding mechanism in the α -regime. The region with the highest emission intensity is still located close to the sheath, but it has collapsed into sheath-like structure, which is considerably thinner has rather sharp boundaries. The collapse into this thin sheath-like structure could be caused by a decrease of l_e^{ex} . But, l_e^{ex} should not change significantly during phase II. The number density n_{Ar} of Ar should not change significantly and the collision cross section $\sigma_{e\text{Ar}}^{\text{tot}}$ is only a function of the electron velocity v_e . The expected increase of the electron temperature T_e (cf. section 4.4.1) during phase II may increase the number of electrons with high velocities but the mean free path at a given v_e is unaffected. One could now speculate that collisions with charged nanoparticles cause the decrease of l_e^{ex} . However, Coulomb collisions of such fast electrons with charged nanoparticles are rather insignificant, based on the simulations in the preceding section. Moreover, the electrons do not

loose kinetic energy in these Coulomb collisions. Only if an electron collides directly with a nanoparticle, it could lose kinetic energy. As mentioned in the preceding section, the cross section for a direct collision $\sigma_{ep}^{\text{coll}}$ of an electron with a nanoparticle is at best the geometric cross section $\sigma_p = \pi d_p^2/4$ of the nanoparticle. At the end of phase II the mean particle diameter is $\langle d_p \rangle \approx 60$ nm (cf. figure 4.14). With an estimated nanoparticle number density of $n_p = 5 \times 10^{13} \text{ m}^{-3}$ one obtains $l_e = (n_p \sigma_{ep}^{\text{coll}})^{-1} \approx 7$ m. The contribution of charged nanoparticles to l_e^{ex} should be negligible. A better explanation of the observed emission profile could be the pile up of electrons in a layer close to the sheath by an electric field. The radiative life time τ_{rad} of the metastable states in table 4.3 lies in the range of $23 \text{ ns} \leq \tau_{\text{rad}} = A_{\text{kl}}^{-1} \leq 253 \text{ ns}$. The mean thermal velocity of a metastable Ar atom at neutral gas temperature of $T_n = 300 \text{ K}$ is $v_{\text{th,Ar}} \approx 400 \text{ m s}^{-1}$. A metastable Ar atom can at best move 0.1 mm before it decays radiatively. This means that a high emission intensity is not only linked to a high number density n_{ArI} of metastable Ar but also to a high number density n_e of free electrons with sufficient energy that excite Ar atoms. If a large number of free electrons with high energy is indeed confined in a layer next to the sheath, it would explain the observed emission profile. *Gogolides et al.* modeled an electronegative SF_6 discharge and found that electrons indeed pile up in a layer close to the electrode sheath during one half-period of the RF-cycle [171]. The RF field between the electrodes results in a substantial electrical field strength inside the plasma bulk. The free electrons drift towards one of the electrodes. Because neither the negative nor the positive ions can follow the RF field, their spatial distribution is unaffected. Close to the electrode the free electrons are repelled by a space-charge field origination from differences in the number densities of positive n_+ and negative ions n_- . The accumulation of free electrons in this region with a relatively high electric field strength raises the mean electron energy and results in an increased excitation and ionization. The free electrons accumulate until the RF field becomes larger than the space-charge field and the electrons can reach the electrode. After one half-period of the RF-cycle the field in the bulk reverses and the electrons begin to drift towards the other electrode. This behavior would indeed explain the observed emission pattern. It would also be in line with conjectures in previous sections that the nanoparticle loaded discharge displays some of the behavior expected for electronegative discharges. The SF_6 discharge modeled by *Gogolides et al.* is quite electronegative with $n_-/n_e \approx 400$. This would correspond to a nanoparticle loaded discharge with a large Havnes parameter, i.e. $P \gg 1$ (cf. section 2.3). Whether this is true for the discharge investigated in this work is not clear, but even if the discharge is not as electronegative, the results

of *Gogolides et. al.* are a good starting point for interpreting the emission profile. *Gogolides et. al.* also mentioned in their work that the ionization rates in the plasma bulk of the SF₆ discharge are substantial and are more important for sustaining the discharge than the ionization in the electron accumulation layers near the electrodes. The maximum ionization rates in these layers is higher, but the volume is small compared to that of the plasma bulk. They have explained the substantial ionization and excitation rates in the plasma bulk with the substantial electric field strength in the plasma bulk. The presence of a substantial electric field strength in the nanoparticle loaded discharge can also be expected during phase II. The increase of the plasma bulk resistance R_b should result in a larger voltage drop across the plasma bulk. However, it is unclear whether a substantial amount of excitation takes place in the plasma bulk of the nanoparticle loaded discharge. The setup for optical emission spectroscopy has unfortunately no spatial resolution (cf. subsection 3.3.2). Spatially resolved optical emission spectroscopy and phase resolved optical emission spectroscopy (PROES) could provide important information for verifying whether or not the discharge is indeed sustained by a different mechanism during phase II of the discharge cycle, and whether this mechanism is the same as the described by *Gogolides et al.*. Arguably, both the wave-riding mechanism in the α -regime and the mechanism described by *Gogolides et. al.* describe the same mechanism for sustaining the discharge. Both describe Joule heating of the electrons and subsequent ionization of neutrals. The main difference are the positions at which Joule heating and ionization, respectively occur.

4.5 Loss of Nanoparticles (Phase III)

Phase II of the discharge cycle is characterised by a reversal of the changes of the discharge parameters observed during phase I. Whereas most of the measured discharge parameters return to their phase I-levels at the end of phase III, i.e. the end of the discharge cycle (cf. figure 4.15, 4.25, and 4.33), this is not true for parameters that reflect the plasma chemistry in the discharge. The time evolution of the mass spectrometer ion currents I_{26} and I_{50} corresponding to m/z ratios of 26 and 50, respectively, are shown in figure 4.34. The contribution from C_2H_2 and the C_4H_2 molecules are expected to dominate I_{26} and I_{50} , respectively. Neither I_{26} nor I_{50} has reached its phase

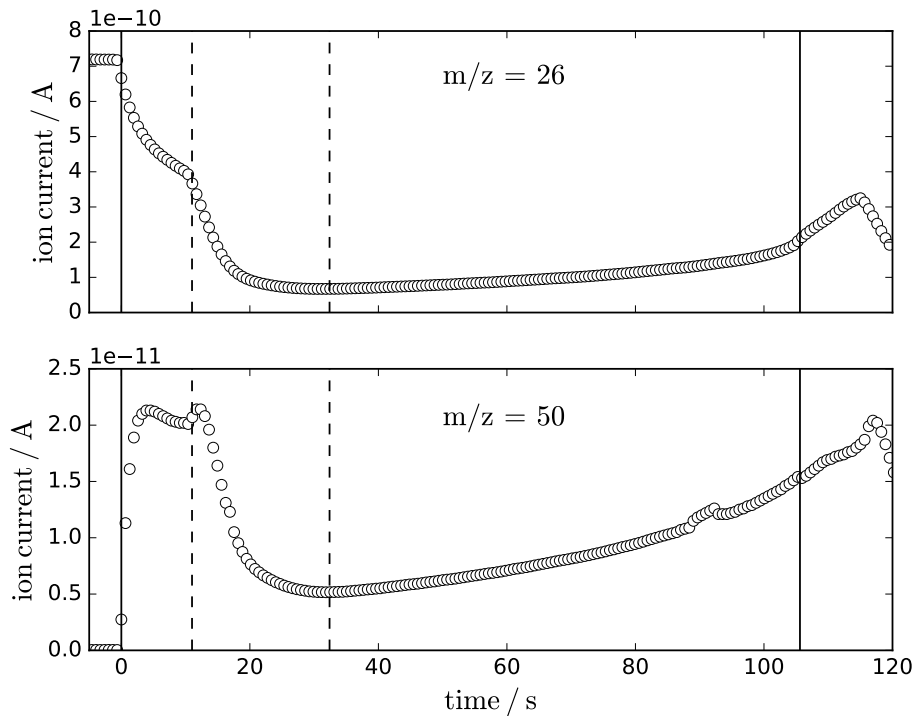


Figure 4.34: Time evolution of the mass spectrometer ion currents I_{26} and I_{50} corresponding to m/z ratios of 26 and 50, respectively, during the 1st discharge cycle. The dashed vertical lines indicate the end of phase I and II, respectively. The solid black lines mark the ignition of the discharge at $t = 0$ s and the end of the 1st discharge cycle, respectively.

I-level at the end of phase III. Only well into phase I of the 2nd discharge cycle does I_{50} reach a level it had during phase I of the 1st discharge cycle.

The mass spectrometer ion current I_{26} does not reach this level at all. Even well into phase I of the 2nd discharge cycle it stays below this level. In fact, it does not even reach the level it had directly before the onset of phase II of the 1st discharge cycle. Another difference between I_{26} and I_{50} is their response to the end of the discharge cycle. Whereas the increase of I_{26} accelerates at the end of the discharge cycle, the increase of I_{50} appears to be completely unaffected. That I_{26} and I_{50} behave differently is not surprising. The C_2H_2 and the C_4H_2 molecules are generated and consumed in different reactions, which will be affected in different ways by the changes at the end of the discharge cycle. For detailed information about the relevant reactions, the interested reader may refer to the work by *Boegarts et al.* [41–43]. The slower response of I_{26} and I_{50} to the end of the discharge cycle can be explained by the low C_2H_2 -flux $Q_{C_2H_2}$ into the 'Pequod'-reactor. Even if no C_2H_2 molecules were consumed it would take a few seconds to restore the number density $n_{C_2H_2}$ of C_2H_2 molecules to a level found in the pristine discharge. In this case the rise of the C_2H_2 -partial pressure $p_{C_2H_2}$ is given by

$$\frac{d}{dt}p_{C_2H_2} = \frac{Q_{C_2H_2}}{V_R}. \quad (4.16)$$

The inner volume of the 'Pequod'-reactor can be estimated as $V_R \approx 5 \times 10^{-3} \text{ m}^3$. The formation of C_2H_2 molecules in the discharge is not taken into account because the number densities of the required educts in the discharge should be orders of magnitudes lower than $n_{C_2H_2}$ [42]. With $Q_{C_2H_2} = 1 \text{ sscm} \approx 1.69 \times 10^{-3} \text{ Pa m}^3 \text{ s}^{-1}$ one finds $d/dt p_{C_2H_2} \approx 0.3 \text{ Pa s}^{-1}$. This is the maximum rate at which $p_{C_2H_2}$ can rise. However, this rate will be much smaller during an actual process run in the 'Pequod'-reactor. The butterfly valve keeps the absolute process pressure p constant at $p = 8 \text{ Pa}$ and the high Ar-flux $Q_{Ar} = 10 \text{ sscm}$ requires a relatively large effective pumping speed S_{eff} to keep this level. Gas molecules are constantly pumped out of the 'Pequod'-reactor. Moreover, the discharge is still rung after the end of the discharge cycle so that C_2H_2 molecules are constantly consumed. Thus, $n_{C_2H_2}$, i.e. $p_{C_2H_2}$, can only rise at a rate which is given by the difference between its production and loss rate. This conclusion also holds for the number density $n_{C_4H_2}$ of C_4H_2 molecules.

In contrast to the slow response at the end of the discharge cycle I_{26} and I_{50} respond rapidly to the increase of the degree of excitation at the onset of phase II (cf. section 4.4.1). The decrease of I_{26} slows down during phase I but suddenly accelerates at the onset of phase II. Although it shows a different behaviour, I_{50} also responds rapidly at the onset of phase II. It slightly increases before it reverses this trend and begins to decrease. Despite these differences at the onset of phase II, do both I_{26} and I_{50} reach their minimum

values at the end of phase II. This is inline with the observation that all other recorded discharge parameters have an extremum at the end of phase II. Because, I_{26} and I_{50} should reflect $n_{\text{C}_2\text{H}_2}$ and $n_{\text{C}_4\text{H}_2}$, respectively, it is expected that $n_{\text{C}_2\text{H}_2}$ and $n_{\text{C}_4\text{H}_2}$ have as well minimum values at the end of phase II. This can be explained by an increased consumption of C_2H_2 and C_4H_2 molecules. They are primarily consumed in reactions with highly energetic electrons, i.e. ionization, dissociative attachment, and electron impact dissociation, or in reactions with radicals and ionised molecules [41–43]. The radicals and ionised molecules are themselves created in reactions that require highly energetic electrons. A higher degree of excitation of the discharge corresponds to an increased amount of highly energetic electrons. Thus, the consumption of C_2H_2 and C_4H_2 should be enhanced. During phase III this is reversed. The degree of excitation decreases and the consumption of C_2H_2 and C_4H_2 decreases as well.

An interesting question is why the degree of excitation actually decreases during phase III. The mean particle diameter $\langle d_p \rangle$ increases continuously during the entire 1st discharge cycle (cf. figure 4.14). Even if the Havnes effect (cf. section 2.3) was limiting the particle charge q_p one would expect a constant degree of excitation instead of a decreasing degree of excitation. Two potential reasons that could explain the observed decrease of the degree of excitation are a rearrangement of the nanoparticle ensemble in the discharge or a continuous loss of nanoparticles from the discharge. A combination of both processes could of course also be a possible explanation. It is unlikely that a simple rearrangement of the nanoparticle ensemble causes the observed decrease of the degree of excitation, because the decrease proceeds continuously over a long period of time. It may well be the case that the nanoparticles rearrange continuously but it is difficult envision a scenario in which the number of nanoparticles stays constant at the same time. For example, the formation of a void could lead to the rearrangement of the nanoparticle ensemble into a shell surrounding the void. If the void expands, which has indeed been reported in other studies [101, 103, 106], the shell should become thinner and the number density n_p of nanoparticles in the shell should increase. As the negatively charged nanoparticles repel each other this increase of n_p should increase the force pushing the nanoparticles out of the discharge. Therefore, it is more reasonable to assume that the loss of nanoparticles is the primary cause for the observed decrease of the degree of excitation. The loss of nanoparticles could of course be exacerbated by a rearrangement of the nanoparticles as outlined above.

A diagnostic that has the potential of providing information about n_p that could verify this hypothesis is the transmission spectroscopy setup installed on the 'Pequod'-reactor. The time evolution of the transmission T_{250} at 250

nm, the transmission T_{532} at 532 nm, and the transmission T_{633} at 633 nm can be found in figure 4.35. The transmission at 532 nm and 633 nm do not

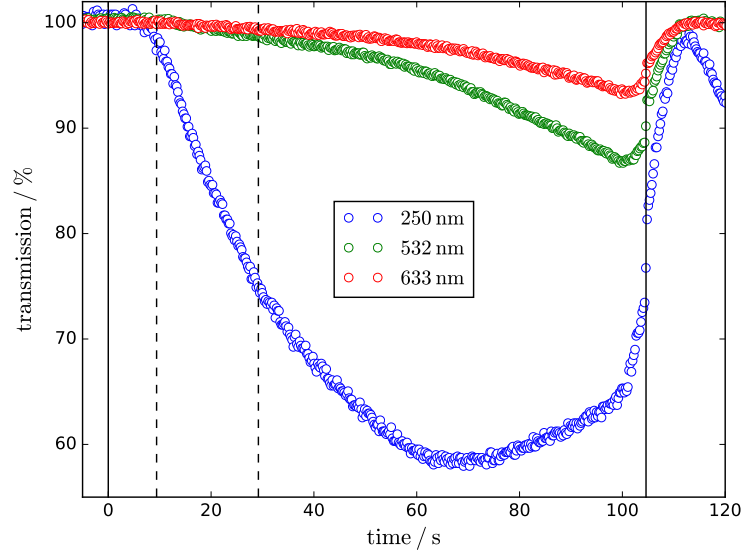


Figure 4.35: Time evolution of the transmission of light with wavelengths of 250 nm, 532 nm, and 633 nm through the discharge during the 1st discharge cycle. The dashed vertical lines indicate the end of phase I and II, respectively. The solid black lines mark the ignition of the discharge at $t = 0$ s and the end of the 1st discharge cycle, respectively.

conclusively indicate that n_p decreases during phase III. Only the increase of T_{532} and T_{633} at the very end of phase III does indicate that n_p decreases. But, this is expected because the discharge cycle ends. The problem is that the transmission at a given wavelength only provides information about the product of line integrated nanoparticle number density n_p^{lin} and the extinction cross section σ_{ext} in the form of the optical depth $\tau = n_p^{\text{lin}} \sigma_{\text{ext}}$ (cf. section 2.4.5). If the increase of σ_{ext} is larger than the decrease of n_p^{lin} the optical depth and thus the transmission will decrease. As $\langle d_p \rangle$ increases continuously during phase III, this is a distinct possibility. One could speculate that the minimum of T_{250} , and thus τ , at around 70 s does indicate that n_p^{lin} decreases at least during the second half of phase III, but for a robust interpretation of T_{250} one would need more information. The extinction cross section σ_{ext} only increases monotonically in the regime in which the Rayleigh approximation $S = \pi \langle d_p \rangle / \lambda \ll 1$ is valid. At 70 s the mean particle diameter is $\langle d_p \rangle \approx 120$ nm. At a wavelength $\lambda = 250$ nm this translates into a size

parameter $S \approx 1.5$. In this size parameter range σ_{ext} may decrease with increasing $\langle d_p \rangle$. *Irvine* calculated the normalised extinction cross section Q_{ext} for absorbing and transparent spheres for different S [172]. The normalised extinction cross section is the ratio of the extinction cross section to the geometric cross section of the sphere. With the mean particle diameter $\langle d_p \rangle$ one can express Q_{ext} as

$$Q_{\text{ext}} = \frac{4\sigma_{\text{ext}}}{\pi\langle d_p \rangle^2} \quad (4.17)$$

Irvine did observe an oscillating behaviour of Q_{ext} for large size parameters. In the range of $S = 1.5$ does Q_{ext} still increase monotonically. But, Q_{ext} also depends on the refractive index $n = n' - i n''$ of the particles, which is also not exactly known for the nanoparticles growing in the discharge. At higher wavelengths some data is available [122, 173, 174], but it remains questionable whether these results can be extrapolated to lower wavelengths. Instead of trying to interpret the transmission spectra with insufficient information, it would be better to obtain the missing information in separate experiments and perform a detailed modeling of the transmission spectra. Information about n could be obtained by in-situ Mie-Ellipsometry [122, 173, 174] or ex-situ by investigating collected nanoparticles. Once sufficient information about n is available, one can calculate σ_{ext} as a function of the size parameter S [172]. By fitting (2.29) to the transmission spectra one would then be able to extract information about n_p^{lin} . In principal the transmission data at a single wavelength would be sufficient to obtain n_p^{lin} from a fit, but the complete transmission spectrum represents a more robust data base. Transmission spectra have indeed been used to obtain information about the particle growth in different discharges [147, 175–177].

This is another example why a multidagnostic approach is necessary to investigate nanoparticle forming reactive plasmas. These systems behave in very complex ways and even several independent diagnostics do not provide enough information to describe the behaviour of these systems unambiguously.

4.6 Particle Formation in the 1st discharge cycle

Although evidence for the formation of a second generation of nanoparticles in the first discharge has been presented in section 4.1, the formation and growth of this particle generation will not be discussed in this section because it seems that it has no effect on the the growth of the first particle generation and on the behaviour of the discharge. As can be seen from figure 4.36 the average particle diameter $\langle d_p \rangle$ grows linearly with time for the better part of the first discharge cycle. At the beginning of the discharge cycle the average particle diameter increases non-linearly.

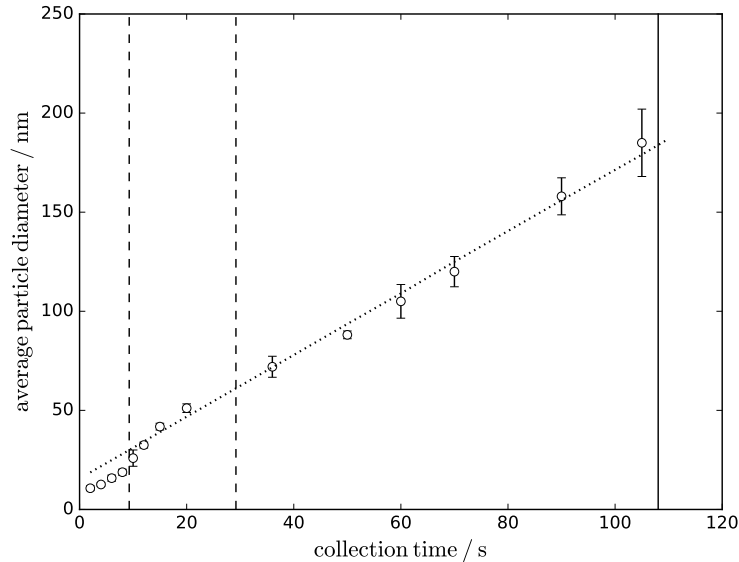


Figure 4.36: Plot of the mean diameter $\langle d_p \rangle$ of 1st generation particles formed in the 1st discharge cycle as a function of the collection time t_c . The dotted line indicates the fit of a straight line to datapoints with $\langle d_p \rangle > 40$ nm. The dashed vertical lines mark the end of phase I and II, respectively. The error bars indicate the $\alpha = 0.05$ confidence interval.

A linear growth of the particle diameter at large particle diameters is a well documented behaviour for the investigated type of discharge [51, 122, 173, 178]. However, these studies are, by and large, limited to diameters larger than 80 nm. As can be seen from figure 4.36, for the system under investigation the linear relationship continues down to $\langle d_p \rangle \approx 40$ nm.

The observed constant growth rate of $\langle d_p \rangle$ with time can be explained by

assuming that the density ρ_p of the particles as well as the mass flux density towards the particles j_p are constant [179]. Furthermore, j_p is assumed to be isotropic. The change of a nanoparticle's mass per time is given by

$$\frac{d}{dt}m_p = \oint_A dA j_p$$

with m_p being the mass of a single nanoparticle. Given that the particle is a perfect sphere with constant density ρ_p one can rewrite the above relation as

$$\frac{d}{dt} \frac{\pi}{6} \rho_p d_p^3 = \int_0^\pi \int_0^{2\pi} d\phi d\theta j_p \frac{d^2}{4} \sin(\theta)$$

After integrating the right hand side and applying the chain rule to the left hand side one finds

$$\frac{\pi}{2} \rho_p d_p^2 \frac{d}{dt} d_p = \pi d_p^2 j_p$$

A final rearrangement yields an expression for a constant growth rate

$$\frac{d}{dt} d_p = 2 \frac{j_p}{\rho_p} = \text{const.} \quad (4.18)$$

Except for the factor 2 this is the same relation one finds for the growth of a thin film with thickness d_f on a substrate if the same assumptions are made, i.e. constant film density ρ_f and constant mass flux density j_f towards the thin film.

$$\frac{d}{dt} d_f = \frac{j_f}{\rho_f} = \text{const.} \quad (4.19)$$

The additional factor 2 in (4.18) is a result of the spherical symmetry of the particles and the isotropy of the mass flux density. If one warps a thin film into a spherical shell and exposes it to a constant, isotropic mass flux density the shell's thickness increases according to (4.19). However, the diameter of the spherical shell increases twice as fast (cf. figure 4.37). The fact that the particle growth can be well described by (4.18) is a clear indication that the particle growth is dominated by surface deposition. Though, there is one significant difference between the growth of thin films on a flat substrate and the growth of the nanoparticles. The area A_s of the substrate, i.e. a silicon wafer, does not change over time. A constant mass flux density only requires a constant mass flux. In case of the nanoparticle ensemble, the situation is different. The surface area A_p of a particle increases continuously during its growth. A constant mass flux density requires an increase of the mass flux J_p to the particles. If the mass flux to the particles were limited by the

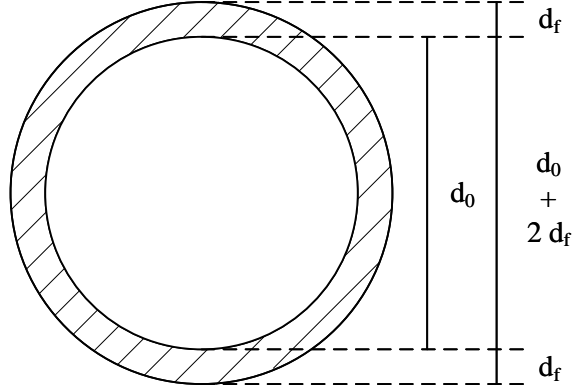


Figure 4.37: Growth of a thin film with spherical symmetry. An increase of the thickness d_f of the thin film translates into an increase of the diameter of the shell it forms that is twice as large.

C_2H_2 -flux $Q_{C_2H_2}$ into the reactor, this requirement could not be met. The total C_2H_2 -mass flux J_{R,C_2H_2} into the 'Pequod'-reactor is given by

$$J_{R,C_2H_2} = m_{C_2H_2} \frac{d}{dt} N_{C_2H_2} \quad (4.20)$$

For the sake of simplicity it is assumed that the total mass of the acetylene molecules $m_{C_2H_2}$ contributes to the mass flux, even if only a small fraction of the hydrogen atoms is eventually incorporated into the nanoparticles. Assuming that the acetylene obeys the ideal gas law and inserting the relations for the number of acetylene molecules $N_{C_2H_2} = p_{C_2H_2} V_{C_2H_2} / k_B T_n$ as well as the formal definition of $Q_{C_2H_2} = d/dt (p_{C_2H_2} V_{C_2H_2})$ one finds the following relation between J_{R,C_2H_2} and $Q_{C_2H_2}$.

$$J_{R,C_2H_2} = m_{C_2H_2} \frac{Q_{C_2H_2}}{k_B T_n} \quad (4.21)$$

The mass flux towards the complete particle ensemble J_p can be estimated from the growth curve in figure 4.36. From the fit to the data in the linear growth regime

$$d_p(t) = \underbrace{1.56}_{s} \frac{\text{nm}}{\text{s}} t + \underbrace{15.5}_{Y} \text{ nm} \quad (4.22)$$

one can derive an expression for the particle mass growth rate $d/dt m_p$.

$$\frac{d}{dt} m_p(t) = \rho_p \frac{\pi}{6} [3s^3 t^2 + 6s^2 Y t + 3m Y^2] \quad (4.23)$$

Choosing the density of the particles $\rho_p = \rho_{\text{a:C-H}} \approx 1.6 \text{ g cm}^{-3}$ to be equal to that of a:C-H films [133] the mass growth rate can be expressed as

$$\frac{d}{dt}m_p(t) = 9.78 \times 10^{-24} \frac{\text{kg}}{\text{s}^3} t^2 + 1.94 \times 10^{-22} \frac{\text{kg}}{\text{s}^2} t + 9.66 \times 10^{-22} \frac{\text{kg}}{\text{s}}. \quad (4.24)$$

The total number of particles is estimated by assuming that they are homogeneously distributed inside the cylindrical volume V_d defined by the electrode and the gap between electrode and showerhead (cf. figure 4.1) with a number density of n_p . Under these assumptions the total mass flux consumed by the particle ensemble is given by

$$J_p(t) = n_p V_d \frac{d}{dt}m_p(t). \quad (4.25)$$

For the ratio of J_p and J_R one obtains the following relationship

$$\frac{J_p}{J_R} = \frac{n_p V_d k_b T_n}{m_{\text{C}_2\text{H}_2} Q_{\text{C}_2\text{H}_2}} \frac{d}{dt}m_p(t). \quad (4.26)$$

With $n_p = 5 \times 10^{13} \text{ m}^{-3}$, $V_d \approx 4.4 \times 10^{-4} \text{ m}^{-3}$, $m_{\text{C}_2\text{H}_2} \approx 26 \text{ u}$, $Q_{\text{C}_2\text{H}_2} = 1 \text{ sccm} \approx 1.69 \times 10^{-3} \text{ Pa m}^3 \text{ s}^{-1}$, $T_n = 300 \text{ K}$, and $t = 100 \text{ s}$ one finds $J_p/J_R \approx 0.15$. Although this back-of-the-envelope type calculation will not be very precise, it supports the assumption of a constant mass flux density in the linear growth regime. Even at the end of the 1st discharge cycle less than 20 % of the mass flux entering the reactor is consumed by the nanoparticles.

The transition of the growth curve from a linear to a non-linear behaviour at particle diameters smaller than $\langle d_p \rangle \approx 40 \text{ nm}$ indicates that either the deposition conditions change over time or that another growth mechanism begins to dominate. The latter conclusion appears to be more plausible. Performing a linear extrapolation of the growth rate at the transition from the linear to the non-linear regime shows that the growth rate is significantly higher in the non-linear regime. The difference of the growth rates in the two regimes gets even more apparent if one considers the time evolution of the particle mass. For the data presented in figure 4.38 it was assumed that the density of the particles $\rho_p = \rho_{\text{a:C-H}} \approx 1.6 \text{ g cm}^{-3}$ is constant, although it has been pointed out earlier that Mie-Ellipsometry and NEXAFS suggest that with increasing diameter the properties of the deposited surface layers change from graphite-like to that of a:C-H films. [122, 123]. The density of graphite $\rho_G \approx 2.2 \text{ g cm}^{-3}$ is higher than the density of a:C-H films [133]. But, the difference between the two is a factor of the order of unity that does not explain the starkly different growth rates seen in figure 4.38. Furthermore, one would expect an even larger difference between the

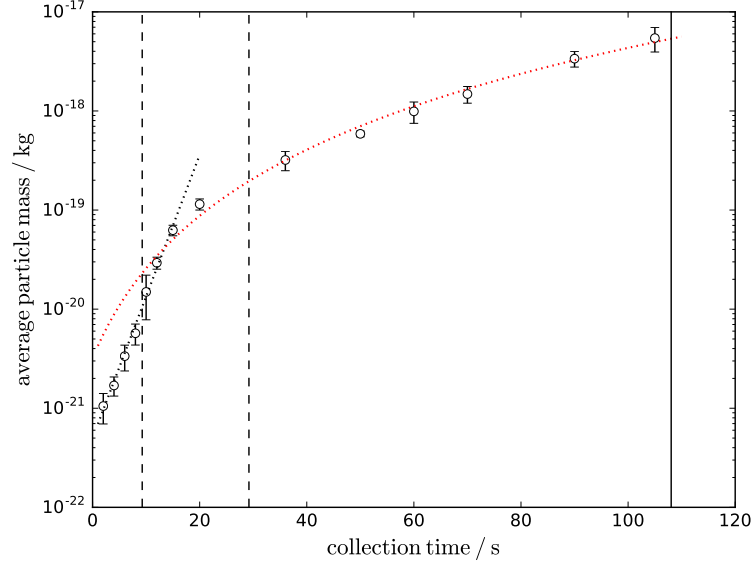
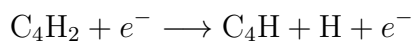
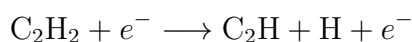


Figure 4.38: Plot of the mean diameter $\langle d_p \rangle$ of 1st generation particles formed at the beginning of the 1st discharge cycle as a function of the collection time t_c . The dotted line indicates a fit of the model described by (4.27) to the data. The error bars indicate the $\alpha = 0.05$ confidence interval.

growth rates because the density of graphite is higher. The red line in figure 4.38 is not a fit to these data but is calculated from equation (4.22). The dotted line in this figure should only be seen as a guidance to the reader. Although it is indeed a fit to the data, it is not based on a specific growth model. That the data can be adequately fitted by a straight line nevertheless suggests that the growth rate in this regime is described by a fast growing function like an exponential function or a higher order polynomial. Such a non-linear growth is compatible with surface deposition as the dominant growth mechanism, but in that case the mass flux density j_p has to increase over time and must be larger than in the linear regime. By combining the relations (4.18) and (4.22) one obtains a value of $j_p^{\text{lin}} = 2.6 \times 10^{-6} \text{ kg m}^{-2} \text{ s}^{-1}$ for the mass flux density in the linear growth regime if a particle density of $\rho_p = \rho_{\text{a:C-H}} \approx 1.6 \text{ g cm}^{-3}$ is assumed. The mass flux density in the non-linear regime $j_p^{\text{n-lin}} = 5.1 \times 10^{-6} \text{ kg m}^{-2} \text{ s}^{-1}$ is estimated from the difference quotient of the data points at 12 s and 15 s. Because j_p cannot be measured directly, it is not possible to say whether the value determined for $j_p^{\text{n-lin}}$ is indeed so large. But, the mass spectrometer measurements (cf. figure 4.34) do provide evidence that $j_p^{\text{n-lin}}$ should be lower than j_p^{lin} . As outlined in

section 4.5, the time evolution of the mass spectrometer ion currents I_{26} and I_{50} reflect the time evolution of the number densities $n_{\text{C}_2\text{H}_2}$ and $n_{\text{C}_4\text{H}_2}$ of the C_2H_2 and the C_4H_2 molecules, respectively. The minima of I_{26} and I_{50} at the end of phase II indicate that the consumption of both molecules is the highest at this point. The increase of their consumption is caused by the higher degree of excitation of the discharge at this point. A high degree of excitation, i.e. a large number of highly energetic electrons, in combination with a high consumption C_2H_2 and the C_4H_2 molecules suggests that the production of radicals by electron impact dissociation reactions is enhanced. Electron impact dissociation reactions include



the production of the C_2H and the C_4H radicals [42]. Radicals are expected to be the main contributors to j_p because stable molecules like C_2H_2 and C_4H_2 should have a low reactivity. Ionised molecules could also contribute to j_p but their number densities are expected to be orders of magnitude smaller than that of the radicals [42]. They should only represent a minor contribution to j_p . Therefore, one would expect that j_p reaches its maximum at the same point at which the production of radicals in the discharge is maximal. Based on the mass spectrometer measurements this should be the case at the end of phase II. But, the non-linear growth regime ends well before the end of phase II (cf. figure 4.38). Based on this evidence it appears unreasonable that $j_p^{\text{n-lin}}$ is larger than j_p^{lin} . The opposite is expected. Because the assumption of surface deposition being the dominant growth mechanism in the non-linear regime is only compatible with the condition $j_p^{\text{n-lin}} > j_p^{\text{lin}}$, one can conclude that surface deposition is not the dominant growth mechanism in the non-linear regime. Another argument for rejecting the assumption that surface deposition is the dominant growth mechanism in the non-linear regime is the particle temperature T_p . In section 4.3.2 it has been argued that a high particle temperature, which might be caused by selective nanoparticle heating, during phase I of the discharge cycle could explain the observed delay of the charge up of the nanoparticle ensemble. A high T_p should also reduce the growth by surface deposition. Many of the reactions in the discharge produce atomic H [41–43]. It has been shown that during the deposition of a:C-H films in hydrocarbon containing discharges the deposited films are eroded by atomic H [180]. At elevated substrate temperatures the erosion rate can even outweigh the deposition rate resulting in a net erosion of the deposited films.

Interestingly, j_p^{lin} seems to be unaffected by the increase of the degree of excitation during phase II and its subsequent decrease during phase III. This

could indicate that the growth of the particles is not limited by the transport of mass to the particles but rather by the reactions on the particle surface.

Given the aforementioned arguments, it appears plausible that another growth mechanism results in the non-linear growth of small particles. Based on the evidence presented in section 4.3.2 that the particles are hot and not highly charged during phase I binary coalescence of nanoparticles is used to explain the observed non-linear growth. Mass conservation during the coalescence of two particles with diameter d_0 into a particle with diameter d_n results in the equality

$$2\frac{\pi}{6}\rho_0d_0^3 = \frac{\pi}{6}\rho_nd_n^3.$$

Given that the density of the particles is the same ($\rho_0 = \rho_n$) the diameter of the particle formed by the coalescence is given by

$$d_n = \sqrt[3]{2} d_0.$$

If all particles in a monodisperse ensemble undergo such a binary coalescence on average after a characteristic time τ_c , the particle diameter will have increased to

$$d_p(t) = d_0(\sqrt[3]{2})^{t/\tau_c} \quad (4.27)$$

after the time t has elapsed. The prefactor d_0 denotes the particle diameter before the onset of the coalescence events. As it turns out this model can adequately describe the non-linear particle growth up to a collection time of 15 s. A fit of this model to the data can be found in figure 4.39. Despite being non-linear, the growth curve has admittedly not many features that would prevent one to successfully fit another model to the data. For example, fits with an exponential function in which the base $\sqrt[3]{2}$ is replaced by a free variable a or a higher order polynomial yield the same or even better agreement with the data. That the presented model can be fitted to the data should thus not be seen as a justification of its validity. Instead, it should be seen as a motivation for future experiments. For the fit shown in figure 4.39 one finds $\tau_c \approx 2.1$ s. Taking into account that the non-linear growth regime spans 13 s, the particles in the discharge undergo approximately 6 coalescence events. This means that the number density of particles should decrease by a factor $2^6 = 64$ in these 13 s. By measuring the particle number density in the discharge one should therefore be able to verify or reject the proposed model as an explanation for the observed non-linear growth. Information about the number density of particles in the discharge would also provide more information about the coalescence process itself. The mean time τ_{coll} between the collision of two nanoparticles of equal size can be estimated in

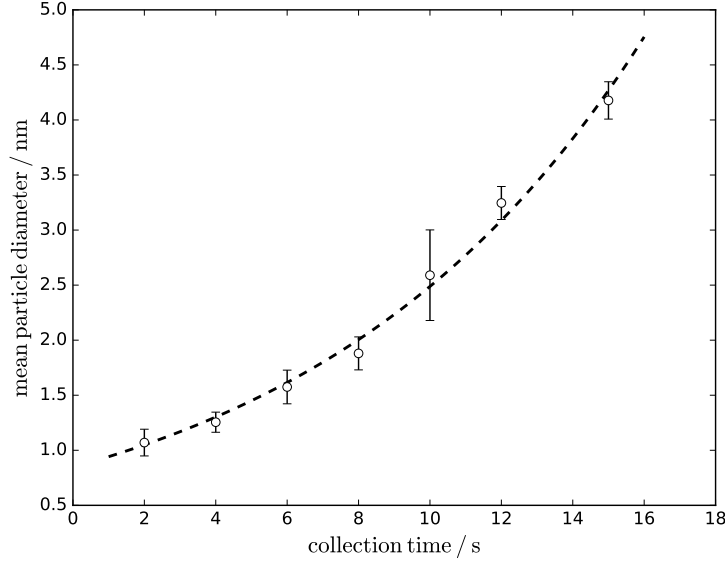


Figure 4.39: Plot of the mean diameter $\langle d_p \rangle$ of 1st generation particles formed at the beginning of the 1st discharge cycle as a function of the collection time t_c . The dotted line indicates a fit of the model described by (4.27) to the data. The error bars indicate the $\alpha = 0.05$ confidence interval.

the following way. The cross section $\sigma_{nn}^{\text{coll}}$ of such a collision is approximated by the cross section $\sigma_{nn}^{\text{coll}} = \pi d_p^2$ for the collision of two hard spheres of equal diameter. The relative velocity of the colliding particles is estimated to be equal to the mean thermal velocity $v_{p,\text{th}}$ of particles obeying the Maxwell-Boltzmann distribution

$$v_{p,\text{th}} = \left(\frac{48k_b T_n}{\pi^2 \rho_p d_p^3} \right)^{1/2}. \quad (4.28)$$

of particles obeying the Maxwell-Boltzmann distribution. It needs to be emphasised that for the calculation of $v_{p,\text{th}}$ the neutral gas temperature T_n is used instead of the particle temperature T_p . The particle temperature T_p is a measure of the energy stored in the vibrational degrees of freedom inside the particle. It is not a measure of the energy stored in the translational degrees of freedom of the particle, i.e. its kinetic energy. It is assumed that its kinetic energy is in equilibrium with that of the neutral gas ensemble in the reactor. Thus, T_n is used instead of T_p . With the nanoparticle number

density n_p one can express τ_{coll} as

$$\tau_{\text{coll}} = \left[4d_p^{1/2} n_p \left(\frac{3k_B T_n}{\rho_p} \right)^{1/2} \right]^{-1}. \quad (4.29)$$

For $d_p = 32$ nm, $n_p = 1 \times 10^{14}$ m⁻³, $\rho_p = 1.6$ g cm⁻³, and $T_n = 300$ K one obtains $\tau_{\text{coll}} \approx 5$ s. This means that τ_{coll} and τ_c are of the same order of magnitude but τ_{coll} is larger than τ_c . This is not expected by the model. In addition, it has to be taken into account that not every collision will necessarily result in the coalescence of the colliding particles and that the coalescence process itself also requires a certain amount of time. If n_p were higher than expected, τ_{coll} could decrease below τ_c . In the earlier stages of particle growth τ_{coll} will fall below τ_c if the model is indeed correct. According to the model one would expect that n_p increases to $n_p = 8 \times 10^{14}$ m⁻³ if the particle diameter decreases to $d_p = 16$ nm. Keeping all other variables constant one finds $\tau_{\text{coll}} \approx 1$ s \leq $\tau_c \approx 2.1$ s. Attractive forces between charged and uncharged nanoparticles as well as oppositely charged nanoparticles could also decrease τ_{coll} [181].

Another observation that seems to contradict the model described above is that the transition from the non-linear to the linear growth regime takes place some seconds after the onset of phase II (cf. figure 4.38). If the conclusion of previous sections that the nanoparticles charge up negatively at the onset of phase II is correct, the binary coalescence should stop immediately at this point as the negatively charged particles repel each other. But, it has to be taken into account that the fits in figure 4.38 have uncertainties as well. Moreover, it needs to be taken into account that even if the particles charge up negatively only new coalescence processes will be suppressed. Particle that have collided before their charge up will like continue to coalesce. If the particle temperature T_p also drops at the beginning of phase II (cf. section 4.3.2), mass transport by diffusion will become less efficient. Thus, the coalescence process will take longer. This could explain why the coalescence of nanoparticles appears to dominate the particle growth for a few seconds after the charge up of the nanoparticles. Because modeling the particle growth in the non-linear regime as the binary coalescence of nanoparticles is highly speculative, a verification by further experiments or simulations is required and it should rather be seen as a motivation and starting point for these investigations.

4.7 SAXS Investigations of Particle Formation

The results presented in the preceding section are very valuable and show that collecting nanoparticles from the discharge and investigating them ex-situ is a reasonable approach for investigating the particle formation in reactive plasmas. But, this approach has one major disadvantage. It is very time-intensive. The data shown in figure 4.36 represents 70 experiments, in which nanoparticles were collected. In addition, it is not only necessary to perform the actual collection experiments but to characterise the particles ex-situ. For the data depicted in figure 4.36 this included the acquisition of more than 700 SEM images and the manual determination of the mean particle diameter $\langle d_p \rangle$ for each image. Obtaining the same information for a different parameter set necessitates the repetition of all this work. Therefore, it would be quite advantageous to have a diagnostic that provides information about $\langle d_p \rangle$ with an in-situ measurement. The different versions of Mie-ellipsometry do offer such in-situ measurements of $\langle d_p \rangle$, but they are, in general, limited to the measurement of diameters $\langle d_p \rangle \geq 40$ nm [122, 173, 174]. Transmission spectroscopy in the UV range could be used as well (cf. subsection 4.5). Measurements of $\langle d_p \rangle \leq 10$ nm have been reported [147].

Another diagnostic that does offer, in principle, the sought after in-situ capabilities is small angle X-ray scattering (SAXS) (cf. subsection 2.4.6). Recently the in-situ measurement of nanoparticles in atmospheric microwave discharges by SAXS has been reported [182, 183]. To further evaluate the prospects of SAXS as a diagnostic for the nanoparticle formation in reactive plasmas, the 'Pequod'-reactor has been installed at the P03 beamline at the DESY synchrotron facility (cf. subsection 3.3.6).

Because it had been unclear how long the integration times for the scattering signal needed to be, the SAXS measurements were performed on a discharge that was operated in a different way than the discharge described in the preceding part of this work. The basic idea was to form nanoparticles of a certain size and trap this nanoparticle ensemble in a pure Ar discharge. The SAXS measurements were then performed on the trapped nanoparticle ensemble. This approach has been successfully used by other groups to trap nanoparticle ensembles in discharges and investigate the trapped particles (cf. for example [76, 152]). The growth of the nanoparticles was limited by injecting only a fixed amount of C_2H_2 into the 'Pequod'-reactor after the Ar discharge had been ignited. To minimize the loss of nanoparticles from the discharge, the discharge was operated with the twin electrode configuration (cf subsection 3.1.3). The electrode gap was 30 mm symmetrically around

the centre point of the 'Pequod'-reactor (cf. subsection 3.1.1). The discharge was driven asymmetrically with the upper electrode grounded. Driving the discharge symmetrically in a push-pull mode did not appear to result in an improved trapping of the nanoparticle ensemble in the discharge. Measurements of the phase angle ϕ_{RF} between the 1st harmonics of RF-current and -voltage showed that it returns much faster to its value in a pristine discharge if the discharge is driven symmetrically, compared to being driven asymmetrically. The process parameters with which the discharge was run are listed in table 4.5. The C_2H_2 – flux into the reactor was only switched on

Table 4.5: Process parameters for running the discharge during SAXS measurements.

Parameter	Symbol	Value
Absolute pressure	p	30 Pa
RF-power	P_{RF}	20 W
Ar-flux	Q_{Ar}	10 sccm
C_2H_2 -flux	$Q_{\text{C}_2\text{H}_2}$	1 sccm

for a short period until the preset amount $M_{\text{C}_2\text{H}_2}$ of C_2H_2 had been admitted into the reactor. The SAXS measurements of the trapped nanoparticle ensemble have been performed 1 minute after the injection of C_2H_2 had been completed. This delay should ensure that $\langle d_p \rangle$ has reached a stable value before the SAXS measurements are started. The effective pumping speed of the 'Pequod'-reactor is given by $S_{\text{eff}} = Q_{\text{Ar}}/p$. With $p = 30$ Pa and $Q_{\text{Ar}} = 10$ sccm $\approx 1.69 \times 10^{-2} \text{ Pa m}^3 \text{ s}^{-1}$ one gets $S_{\text{eff}} \approx 5.6 \times 10^{-4} \text{ m}^3 \text{ s}^{-1}$. Assuming a reactor volume $V_{\text{R}} \approx 5 \times 10^{-3} \text{ m}^3$ one can estimate the gas residence time as $t_{\text{r}} \approx V_{\text{R}}/S_{\text{eff}} \approx 9$ s. Thus, 1 minute should be sufficient to pump all remaining C_2H_2 molecules out of the 'Pequod'-reactor and prevent further growth of the particles by surface deposition.

One problem that was encountered during the SAXS measurements was a large and drifting background signal. Three representative scattering images recorded with the 2d X-ray detector (cf. subsection 3.3.6) are shown in figure 4.40. The set of images in figure 4.40 show that the scattering originating from the nanoparticles dispersed and trapped in the discharge is small compared to parasitic scattering. To the naked eye the difference between the scattering images of the system with (centre) and without (LHS) nanoparticle loaded discharge is almost invisible. Only by subtracting both images (RHS) becomes the scattering intensity originating from the nanoparticles visible to the naked eye. Indeed, the maximum scattering intensity originating from the nanoparticles is at least two orders of magnitude smaller than

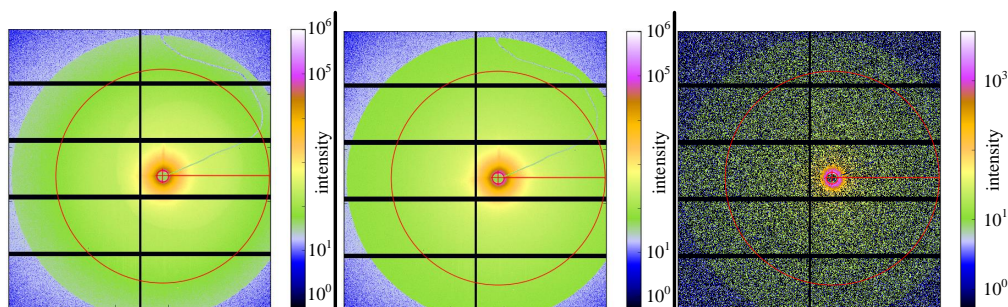


Figure 4.40: Representative scattering images recorded by the 2d X-ray detector. The scattering image on the left-hand side corresponds to a measurement without discharge. The image in the centre shows a measurement in which nanoparticles were trapped inside the running discharge. The image on the right-hand side is the difference between the scattering image with (centre) and without (LHS) nanoparticle loaded discharge. The integration time was $t_i = 60$ s. The red circles indicate the region for azimuthal averaging of the scattering intensity.

that caused by parasitic scattering. The primary source of the parasitic scattering is not exactly known, but it can only originate from matter directly illuminated by the direct beam. The intensity of X-ray light that has been scattered multiple times is too low to cause such a high background signal. The discharge itself does not contribute to the background signal. There is no significant difference between scattering images if the 'Pequod'-reactor is evacuated or a pure Ar-discharge is running. The parasitic scattering originates from the Kapton® windows, particles or films that are deposited on the windows, or a combination of both. Another problem is that the intensity of the background drifts. It increases over time. The drift could be caused by a degradation of the windows due to the illumination with the high intensity X-ray beam or by an increasing deposition of particles and films on the windows. The drift of the background is especially problematic at long integration times. If the background increases significantly during the integration time, one cannot eliminate the background of a measurement by simply subtracting the background recorded in a reference measurement. One strategy to overcome this problem would be to use integration times t_i during which the drift of the background can be neglected for recording two images. One image is used for recording the actual scattering experiment. The other image is used for recording the background. For these two images a simple background subtraction can be performed. By summing a large set of these images with subtracted background one would obtain an image with

high intensity. This approach of course only works if t_i results in a sufficient signal-to-noise ratio. Another shortcoming of this approach is that it requires a high repeatability of the experiment. For the experiments described in this work one would always need to remove the nanoparticles from the discharge for recoding the background and form a new particle ensemble for the next experiment.

Because the SAXS experiments described in this work only serve as a proof of concept such an advanced scheme for the elimination of the background is not used. Furthermore, for an integration time $t_i = 60$ s the drift of the background does not seem to be excessive. As the obtained scattering images are rotationally symmetric (cf. figure 4.40), they are azimuthally averaged to improve the signal-to-noise ratio before they are analysed. The mean diameter $\langle d_p \rangle$ of the nanoparticles trapped was obtained by using the Guinier approximation (cf. subsection 2.4.6). A representative Guinier plot is depicted in figure 4.41. As expected the slope at low values of the scat-

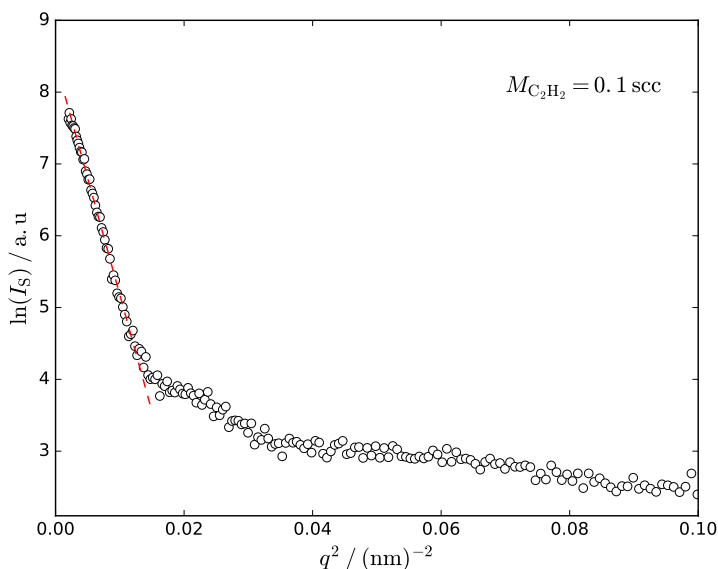


Figure 4.41: Guinier plot of the scattering intensity. The natural logarithm of the scattering intensity I_S is plotted as a function of the squared scattering vector q . A total amount $M_{C_2H_2} = 0.1$ scc of C_2H_2 was injected into the discharge to generate nanoparticles. The dashed red line indicates the fit of a straight line to the data at low q .

tering vector q is linear. By fitting a straight line to the data in this region and using equations (2.33) and (2.35) one can obtain $\langle d_p \rangle$ from the Guinier

plots. The results from analysing the Guinier plots are summarised in figure 4.42. It shows $\langle d_p \rangle$ as a function of the injected C_2H_2 amount $M_{C_2H_2}$. Unfortunately, the data in figure 4.42 is not only sparse, but also suggests

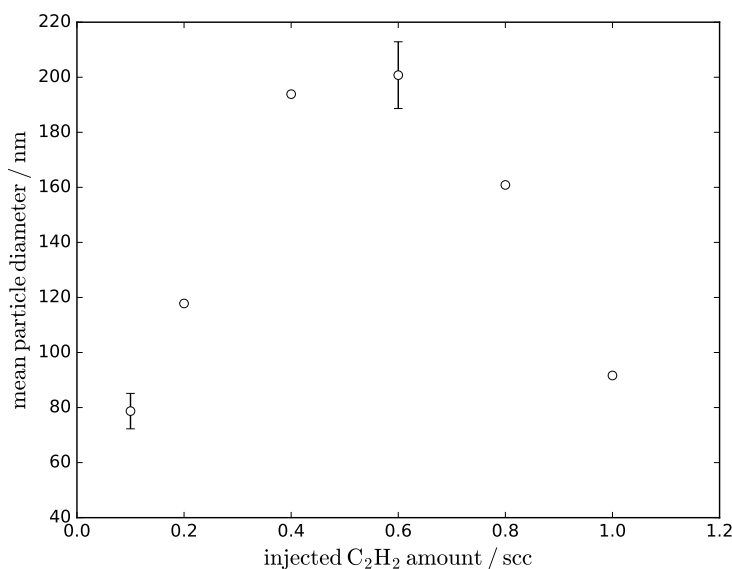


Figure 4.42: Mean particle diameter $\langle d_p \rangle$ as a function of the injected C_2H_2 amount $M_{C_2H_2}$. Repetitive SAXS experiments have only been performed for the data points at $M_{C_2H_2} = 0.1$ scc and $M_{C_2H_2} = 0.6$ scc. The error bars indicate the $\alpha = 0.05$ confidence interval.

that the SAXS measurements are affected by limitations of the experimental setup. It is unexpected that $\langle d_p \rangle$ decreases for $M_{C_2H_2} \geq 0.6$ scc. The particle formation process at the process parameters in table 4.5 has not been studied independently like the formation process at the standard process parameters (cf. table 4.1). But, there is no evidence that would support the assumption that the particle formation process is starkly different for both sets of process parameters. One could argue that the apparent decrease of the particle diameter is caused by a loss of the 1st particle generation and the formation of a 2nd particle generation with smaller $\langle d_p \rangle$. But, the time evolution of the phase angle ϕ_{RF} between the 1st harmonics of RF-current and -voltage does not indicate a sudden loss of nanoparticles. Moreover, in that case one would expect that $\langle d_p \rangle$ drops once and increases afterwards because the 2nd particle generation grows. The data, however, suggests that $\langle d_p \rangle$ decreases with increasing $M_{C_2H_2}$. One could also speculate that the particle might be etched in the Ar-discharge. It has indeed been reported that carbonaceous

nanoparticles trapped in Ar-discharges do loose mass, which indicates etching, but this process seems to be relevant only on time scales that exceed the length of the SAXS experiments [76, 173].

The observed decrease of $\langle d_p \rangle$ for $M_{C_2H_2} \geq 0.6$ scc is most likely caused by an unsuitable experimental setup. In general, it is not reasonable to use the Guinier approximation for data that do not fulfill the requirement $qR_G \leq 2$ because the underlying assumptions of the Guinier approximation are invalid. Even for $qR_G \approx 1.5$ systematic deviations can reach levels of 20 % to 30 % [83]. The minimum recorded scattering vector was $q_{\min} = 4.48 \times 10^{-2} \text{ nm}^{-1}$. Thus, the maximum radius of gyration $R_{G,\max}$ that can be reliably determined with the Guinier approximation is $R_{G,\max} \approx 34 \text{ nm}$. This corresponds to $\langle d_p \rangle \approx 88 \text{ nm}$. Only the data point at $M_{C_2H_2} = 0.1$ scc fulfills the requirement $qR_G \leq 1.5$. It must be expected that all other data points are affected by substantial systematic deviations. These systematic deviations are also evident in the Guinier plots. The agreement between the straight line fits and the data decreases with increasing $M_{C_2H_2}$. The relevant data is hidden behind the direct beam stop. This problem could be overcome by increasing the distance between the reactor centre and the X-ray detector (SDD). However, this has not been possible at the P03 beamline. The SAXS experiments described in this work have been performed with an SDD close to the maximum value of the P03 beamline. Beamlines specifically built for ultra small angle X-ray scattering (USAXS) would be more suitable for such experiments. For example the ID 02 beam line at the ESRF facility offers an SDD of up to 30 m [184]. At this beamline an q_{\min} of the order of 10^{-3} nm^{-1} could be recorded. One of the aforementioned in-situ measurements of nanoparticles in atmospheric microwave discharges by SAXS has indeed been performed at the ID 02 beamline.

Ex-situ SEM measurements of collected nanoparticles show that the mean particle diameters obtained by SAXS do fall in the correct range. But, a direct comparison is at best misleading. The SEM measurements show that the particle size distributions are multimodal. Unless their number density is negligibly small the contribution from the largest particles will dominate the Guinier plot because of the d_p^6 -dependence of $I_S(q)|_{q=0}$ (cf. (2.37)). Unfortunately, it has yet to be investigated how the particle collection method used in this work (cf. subsection 3.2) affects the particle size distribution of the collected particles. It is not possible to infer any information about the number density of particles with a particular size from the SEM measurements. Therefore, it is not clear which of the different particle diameters that could be obtained from the SEM measurements should be compared directly with the SAXS measurements.

Investigating the growth of particles with $\langle d_p \rangle \geq 80 \text{ nm}$ by SAXS is

not very intriguing. The access to synchrotron beamlines is, by and large, severely restricted due to overbooking and in this diameter range other diagnostics, like Mie-Ellipsometry, are also capable of in-situ measurements. SAXS measurements would only be interesting, if they were able to provide information about the time evolution of $\langle d_p \rangle$ in the range that is inaccessible by the well established diagnostics, i.e. at the beginning of the particle formation process. Unfortunately, the data presented in this work suggests that SAXS is unsuitable for this purpose. The required integration times are too long. The integration time for all SAXS measurements presented in this work was $t_i = 60$ s. Reducing the integration time to $t_i = 2$ s would reduce I_S by a factor 30. In this case the time resolution of the growth process would be comparable to the resolution obtained by the collection experiments (cf. figure 4.39). Reducing I_S by a factor 30 means that approximately a factor 3.4 has to be subtracted from $\ln(I_S)$. Comparing this value with the maximum value in figure 4.41, this reduction appears to be tolerable. But, one has to take into account that a reduction of d_p results in a strong reduction of the maximum scattering intensity $I_S(q)|_{q=0}$. A reduction of d_p from 80 nm to 40 nm reduces $I_S(q)|_{q=0}$ by a factor 64. Accordingly, approximately a factor 4.2 is subtracted from $\ln(I_S)$. Taking both contributions together a factor of 7.6 has to be subtracted from $\ln(I_S)$. For a reduction of d_p from 80 nm to 20 nm this reduction would be approximately a factor 11.7. On a linear scale this corresponds to a reduction of I_S by a factor in excess of 10^5 . Because I_S scales only linearly with the number density n_p of nanoparticles, it is unlikely that an increase of n_p can compensate the strong reduction of I_S . This strong reduction of I_S is especially problematic because the intensity of the background signal is not reduced as strongly. Only the decrease of t_i reduces the background signal. The reduction of d_p does not affect the intensity of the background signal. Taking into account that I_S is already fairly low at $t_i = 60$ s and $\langle d_p \rangle \approx 80$ nm, it appears unreasonable to assume that smaller nanoparticles will provide enough scattering intensity during the integration times required to follow the particle formation. One could of course try to trap very small nanoparticles in the discharge and increase t_i , but this approach will likely fail. Firstly, if the conclusion of the preceding sections is correct and the nanoparticles do not charge up significantly at small $\langle d_p \rangle$ it will not be possible to trap them in the discharge. Secondly, if the growth of these particles is not dominated by surface deposition it will not be possible to limit their growth by shutting off the injection of C_2H_2 . For example, if these particles predominantly grow by agglomeration they will simply continue to grow until the agglomeration is stopped by the charge up of the particles. Therefore, it appears that SAXS is not the method of choice for investigating the particle formation process in reactive nanoparticle forming

plasmas that require a time resolution of the order of some minutes or less.

Yet, SAXS might still be an interesting method for studying the particle formation process in, more or less, static systems like gas aggregation cluster sources [143, 144, 185] or flow-through reactors [186–188]. In such systems very long integration times could potentially be used. Studying the particle formation process would then require to measure the particle size at different spatial positions inside the source or reactor. Very long integration times might necessitate a sophisticated background subtraction procedure, but this should not be an insurmountable issue. Studying nanoparticles with a much higher electron density, for example like noble metal nanoparticles, should also help to solve the intensity issue.

Chapter 5

Summary and Outlook

In this work, the formation of nanoparticles in reactive plasmas has been investigated with a large number of conventional and unconventional diagnostics. A capacitively coupled RF discharge operated in an Ar – C₂H₂ atmosphere was chosen as model system.

The first step in the investigation of the discharge was the development and construction of a sophisticated plasma reactor, the 'Pequod'-reactor. It provides enough ports for the installation of the various diagnostics, and is highly mobile so that it can be easily transported to other laboratories. The reactor is based on a cylindrical high-vacuum chamber with an inner diameter of 200 mm and an inner height of 160 mm. In its standard configuration, the reactor is equipped with a planar, water cooled electrode and a shower head. The electrode as well as the shower head are movable, resulting in an even more versatile system. The shower head can be replaced by a second identical electrode to generate symmetric discharges. The following diagnostics were successfully, admittedly not at the same time, installed on the 'Pequod'-reactor: an impedance probe, a multipole resonance probe (MRP), microwave interferometry (MWI) (separate experiments [91]), a quadrupole mass spectrometer, a pirani gauge, optical emission spectroscopy (OES), UV/Vis transmission spectroscopy, and small angle x-ray scattering (SAXS). The 'Pequod'-reactor is additionally equipped with a system for the collection of nanoparticles. The particles are dragged into a separate vacuum chamber by suddenly inducing a high gas flux between the collector chamber and the reactor. As the collector system can be isolated from the 'Pequod'-reactor, it can be used as a load lock. Thus, the collection of nanoparticles can be performed without breaking the vacuum of the 'Pequod'-reactor. In the future, the list of diagnostics installed on the 'Pequod'-reactor should be extended. Especially self-excited electron resonance spectroscopy (SEERS) [189], Mie ellipsometry [122, 173, 174], a laser fan for light scattering [101, 103, 116],

infrared absorption spectroscopy [190, 191], and near-edge x-ray absorption fine structure (NEXAFS) [123] are promising candidates. Another important improvement of the 'Pequod'-reactor would be the development of a suitable control program. Such a control program would drastically simplify the operation of the reactor and the data acquisition from the different diagnostics. The control program should also provide a synchronization signal for diagnostics that cannot be controlled by the program. This would eliminate the need to synchronize the data from different diagnostics manually.

Operating the 'Pequod'-reactor with a suitable set of process parameters results in the formation of nanoparticles and cyclic changes of the measured discharge parameters. For most discharge parameters one can observe clear differences, for example smaller changes, between the 1st and the subsequent discharge cycles. Collection experiments performed at the beginning of the 2nd discharge cycle revealed the presence of three nanoparticle ensembles with distinctly different sizes in the discharge. Nanoparticles from two of these ensembles are so large that they must have formed in the 1st discharge cycle and remained in the discharge after the end of the 1st discharge cycle. This conclusion is confirmed by UV/Vis transmission spectroscopy. The transmission through the discharge increases only gradually towards the values expected for a pristine (devoid of nanoparticles) discharge at the end of the 1st discharge cycle. This gradual increase extends well into the 2nd discharge cycle. It has been speculated that the presence of these nanoparticles in the discharge reduces the nucleation of nanoparticles at the beginning of the second discharge cycle by the consumption of precursor species. But, UV/Vis transmission spectroscopy measurements indicate that this might not be the only effect contributing to the observed differences between the 1st and the subsequent discharge cycles. The spatial distribution of the nanoparticle ensemble in the discharge could also be different. A less ambiguous interpretation of the data can only be achieved by adding more information from independent diagnostics. For example, recording the scattering of laser light by the nanoparticle ensemble would provide valuable information about the spatial distribution of nanoparticles in the discharge.

A more detailed study of the nanoparticle formation in the 1st discharge cycle showed that after approximately 80% of the discharge cycle has elapsed, a second particle generation is formed in the discharge. This is indicated by the shift from a monomodal to a bimodal size distribution of the collected nanoparticles. The formation of the second particle generation can be correlated with the appearance of a transient shoulder in the mass spectrometer ion current associated with the C_4H_2 molecule ($m/z = 50$ amu). It has been conjectured that the formation of the second particle generation takes place in a void formed inside the discharge, because the conditions inside the void

should facilitate the nucleation of nanoparticles. The presence of a void could also be verified by recording the scattering of laser light by the nanoparticle ensemble.

The formation of the first particle generation in the 1st discharge cycle has been extensively studied by the collection of nanoparticles throughout the discharge cycle as well as by monitoring the time evolution of different discharge parameters. Based on the time evolution of the phase angle between the 1st harmonics of RF-current and voltage, the discharge is subdivided into three phases. Phase I spans approximately the first 9 % (9 s) of the discharge cycle and is characterized by small deviations of most discharge parameters from that of a pristine discharge. Substantial changes of all discharge parameters can only be observed at the transition from phase I to II. Nevertheless, nanoparticles with diameters in the range of 8 - 10 nm can be collected from the discharge as early as 2 s after the ignition of the discharge. The discharge parameter that shows the earliest response, which can be directly linked to the presence of nanoparticles in the discharge, is the UV/Vis-transmission. The transmission at 250 nm allows the reliable detection of nanoparticles approximately 7 s after the ignition of the discharge. This corresponds to particle diameters of 15 - 20 nm. At 532 nm the detection threshold is delayed until approximately 13 s corresponding to particle diameters of 35 - 45 nm. Measurements of the electron density with the MRP show that the electron density decreases only slightly during phase I compared to the drastic decrease observed at the transition between phase I and II. This suggests that the nanoparticles may not charge up significantly during phase I, but charge up rapidly at the transition between phase I and II. This coincides with experimental results from MWI experiments previously performed in the 'Pequod'-reactor [91]. Such a behaviour can not be explained by the OML-theory. To resolve this issue the OML-theory was extended so that it self-consistently takes into account the Schottky emission of electrons adsorbed on the nanoparticles. Simulations imply that electrons need to adsorb with an energy of less than 2.5 eV on the particles. Otherwise the contribution of Schottky emission to the current balance can be neglected for reasonable particle temperatures. Including Schottky emission results in a non-linear increase of the particle charge with increasing particle diameter and decreasing particle temperature, in contrast to the temperature independent, linear increase predicted by the OML-theory. Such a non-linear increase of the particle charge may indeed explain the observed behaviour of the discharge parameters. Although there is indirect evidence that the particle temperature is substantially larger than the neutral gas temperature during phase I, future experiments or simulations should aim at providing more detailed information about the time evolution of the particle temper-

ature to prove the hypothetical influence of Schottky emission of adsorbed electrons. As the measurement of the particle temperature of such small particles is a formidable experimental challenge, simulations are probably a more straightforward approach.

Phase II of the first discharge cycle is characterized by substantial changes of the monitored discharge parameters. It spans approximately 18% (20 s) of the discharge cycle. At the end of phase II many of the monitored discharge parameters reach their extrema. The increase of the emission intensity of the discharge indicates that the degree of excitation of the discharge increases during phase II, although the free electron density decreases. This apparent contradiction has been explained by a simultaneous increase of the electron temperature that outweighs the reduction of the free electron density. The increase of the electron temperature has been linked to an increase of the power that is dissipated in the plasma bulk as the resistance of the plasma bulk increases during phase II. This is reflected in the time evolution of the phase angle between the 1st harmonics of RF-current and voltage. Simulations of the Coulomb collisions between negatively charged nanoparticles and free electrons suggest that the increase of the plasma bulk's resistance is dominated by the reduction of the free electron density and that Coulomb collisions only represent a minor contribution. A drastic reduction of the sheath width and a change of the spatial distribution of the emission intensity during phase II indicate that the discharge is sustained by a mechanism other than the wave-riding mechanism. It has been speculated that after charge up of the nanoparticles and the associated reduction of the free electron density the discharge displays, at least partially, behaviour expected for electronegative discharges. Spatially and phase resolved emission spectroscopy could provide further evidence for this interpretation.

Phase III is characterized by a steady change of the discharge parameters, except the electron density, back to values expected for a pristine discharge. This is unexpected as the nanoparticles are continuously growing throughout the entire discharge cycle. It has been conjectured that this discrepancy is caused by a continuous reduction of the number density of nanoparticles in the discharge and a rearrangement of the nanoparticles remaining inside the discharge. The forces pushing the particles out of the discharge, like the ion or neutral drag force, increase faster with the particle size than the force exerted by the electrical field that confines the negatively charged particles in the discharge. Depending on the local conditions in the discharge, the outward directed forces will outweigh the confining force at a critical particle size and particles will leave the discharge. If the loss of particles is not compensated by the increasing particle size, the influence of the nanoparticles on the discharge parameters will diminish. This presumptive explanation could

be verified by measuring the number density of particles dispersed in the discharge. A promising candidate for such experiments is the detailed investigation of UV/Vis-transmission spectra. However, additional information is needed to interpret the transmission spectra unambiguously. Especially information about the refractive index of the nanoparticles is required.

The particle growth displays only a weak correlation with the time evolution of the discharge parameters. The diameter of large particles increases linearly with approximately 1.6 nm / s for the investigated parameter set. This linear increase of the diameter is well documented and the result of surface deposition onto the particles. For the investigated discharge parameters this linear regime extends well into phase II of the discharge cycle down to particle diameters of approximately 40 nm. The constant growth rate during phase III and the better part of phase II suggest that it is not significantly affected by the observed changes of the discharge parameters. The diameter of smaller particles increases non-linearly with time. A simple model based on the binary coalescence of nanoparticles was used to fit the particle growth in this region. The fit shows a reasonable agreement with the data down to the smallest detectable particle diameters of 8 - 10 nm. As the coalescence of nanoparticles will cause a reduction of the number density of particles, one should be able to confirm the validity of this highly speculative model by determining the number density of particles dispersed in the discharge.

The 'Pequod'-reactor was also successfully integrated into the P03 beam-line at the DESY synchrotron facility to investigate the feasibility of an in-situ measurement of the particle diameter with SAXS. For the scattering experiments nanoparticles of different sizes were generated and trapped inside a symmetrically driven Ar discharge by injecting well defined amounts of C_2H_2 into the discharge. The presence of the dispersed particles was clearly detectable in the obtained scattering data. However, this requires the use of comparably long integration times. Even for particles with diameters of more than 80 nm an integration time of the order of 60 s was required. The measurements are further complicated by a high background signal that drifts significantly over time. SAXS measurements are, therefore, unsuitable for studying the particle formation process in reactive nanoparticle forming plasmas that require a time resolution of some minutes or less. Nonetheless, it could be used for systems that do not require such a time resolution. For example, it could be used to study the formation of nanoparticles in gas aggregation cluster sources or in flow-through reactors.

Summarizing the complete work one comes to the conclusion that the presented multidagnostic approach provided valuable insight into the formation of nanoparticles in reactive plasmas. Nevertheless, a complete understanding of the complicated interplay between the particle growth and the discharge

requires the use of even more sophisticated diagnostics. A diagnostic that provides information about the time evolution of the number density of particles smaller than 50 nm would be a significant step forward. The most promising candidate for providing this information is UV/Vis transmission spectroscopy. A continued effort to investigate these systems, which display a multitude of interesting phenomena, will certainly not only boost the basic understanding of plasmas but also trigger the development of advanced plasma diagnostics.

Appendix A

A.1 List of Acronyms

AFM	atomic force microscopy
DESY	Deutsches Elektronen-Synchrotron
EDX	energy dispersive X-ray spectroscopy
EEDF	electron energy distribution function
EELS	electron energy loss spectroscopy
GEC	Gaseous Electronics Conference
LIPEE	laser induced particle explosive evaporation
MRP	multipole resonance probe
MWI	microwave interferometry
NEXAFS	near edge X-ray absorption fine structure
OES	optical emission spectroscopy
OML	orbit motion limit
PECVD	plasma enhanced chemical vapour deposition
PSLLS	polarisation sensitive laser-light scattering
PROES	phase resolved optical emission spectroscopy
RF	radio frequency
SAXS	small angle X-ray scattering
SDD	sample-to-detector distance
SEERS	self-excited electron resonance spectroscopy
SEM	scanning electron microscopy/microscope
STEM	scanning transmission microscopy
TEM	transmission electron microscopy/microscope
USAXS	ultra small angle X-ray scattering
UV/Vis	ultraviolet/visible

A.2 List of Mathematical Symbols

$\langle X \rangle$	average of variable X
$ X $	absolute value of variable X
A	area (general)
A_{kl}	transition probability from level k to l
A_p	particle surface area
A_s	substrate area
b	impact parameter
b_c	collection radius
C_p	particle capacitance
C_s	sheath capacitance
d_0	initial diameter during binary coalescence of particles
d_f	film thickness
d_p	particle diameter
d_s	sheath thickness
D_0	diffusion constant
e	Euler number
e	elementary charge
E	electrical field strength (general)
E_a	activation energy
E_k	upper level energy
E_{kin}	kinetic energy (general)
$E_{kin,e}$	electron kinetic energy
$\Delta E_{kin,e}$	change of electron kinetic energy
E_l	lower level energy
E_s	electron desorption energy
F_{RF}	driving frequency of the discharge
f_v	velocity distribution function
F	form factor
i	imaginary unit
I_0	incident intensity
I_{26}	mass spectrometer ion current corresponding to $m/z = 26$
I_{50}	mass spectrometer ion current corresponding to $m/z = 50$
$I_{750.9}$	emission intensity at 750.9 nm
$I_{750.9,n}$	normalised emission intensity at 750.9 nm
$I_{763.7,n}$	normalised emission intensity at 763.7 nm
I_d	electron desorption current
I_e	electron current (general)
I_E	extinct intensity
I_i	ion current (general)

I_S	X-ray scattering intensity
I_T	transmitted intensity
j_i	ion current density (general)
\dot{j}_p	mass flux density towards particles
j_p^{lin}	mass flux density towards particles (linear growth regime)
$j_p^{\text{n-lin}}$	mass flux density towards particles (non-linear growth regime)
J_p	mass flux towards particles
J_{R,C_2H_2}	C ₂ H ₂ mass flux into the reactor
k_B	Boltzmann constant
K	interparticle interference contribution to I_S
l_e^{ex}	electron mean free path for excitation
l_e	electron mean free path (general)
L	length/thickness (general)
L_b	plasma bulk inductance
m	mass (general)
m_e	free electron mass
m_i	ion mass (general)
m_p	particle mass
$M_{C_2H_2}$	amount of C ₂ H ₂ injected into the reactor
n	complex index of refraction
n'	real part of index of refraction
n''	imaginary part of index of refraction
n_+	positive ion number density
n_-	negative ion number density
n_{Ar}	Ar number density
n_{ArI}	metastable Ar number density
$n_{C_2H_2}$	C ₂ H ₂ number density
$n_{C_4H_2}$	C ₄ H ₂ number density
n_e	free electron density
$n_{e,p}$	free electron density in nanoparticle loaded discharge
n_i	ion density
n_j	number density of collision partner j
n_p	nanoparticle number density
n_p^{lin}	line integrated nanoparticle number density
N_p	number of nanoparticles
$N_{C_2H_2}$	number of C ₂ H ₂ molecules
p	process pressure (absolute)
$p_{C_2H_2}$	C ₂ H ₂ -partial pressure
\vec{p}_e	free electron momentum
p_b	base pressure
p_u	ultimate pressure

P	Havnes parameter
P_{RF}	RF power
\vec{q}	scattering vector
q	(length of the) scattering vector
q_{min}	minimum recorded scattering vector
Q_{Ar}	Ar flux
$Q_{\text{C}_2\text{H}_2}$	acetylene flux
Q_{ext}	normalised extinction cross section
Q_{p}	particle charge
r_{p}	particle radius
s	slope of staright line
R_{b}	plasma bulk resistance
R_{g}	radius of gyration
$R_{\text{G,max}}$	maximum radius of gyration
S	size parameter
S_{eff}	effective pumping speed
t	time (general)
T	transmission (general)
T_{250}	transmission at 250 nm
T_{532}	transmission at 532 nm
T_{633}	transmission at 633 nm
T_{e}	electron temperature
T_{i}	ion temperature
T_{p}	particle (surface) temperature
T_{n}	neutral gas temperature
\hat{v}_1	1st harmonic of the voltage amplitude
\hat{v}_3	3rd harmonic of the voltage amplitude
v_{e}	electron velocity (general)
$v_{\text{e,th}}$	thermal electron velocity
V	volume (general)
$V_{\text{C}_2\text{H}_2}$	volume filled by C_2H_2 molecules
V_{d}	discharge volume
V_{s}	voltage drop across sheath
V_{R}	reactor volume
Y	y-intercept of straight line
W	work function
Z_{b}	plasma bulk impedance
Z_{d}	discharge impedance
Z_{r}	reactor impedance
Z_{s}	sheath impedance
Γ	electron-ion temperature ratio

ϵ_0	permittivity of free space
$\epsilon_{r,p}$	relative permittivity
η_f	normalised floating potential
θ	deflection angle
λ_D	(linearised) Debye length
$\lambda_{D,e}$	electron Debye length
$\lambda_{D,i}$	ion Debye length
λ_p	inter-particle distance
μ	ion-electron mass ratio
ν_e^m	electron collision frequency for momentum loss
ν_{eAr}^m	electron-Ar momentum loss frequency
ν_{ej}^m	electron-j momentum loss frequency
π	π
ρ_0	initial mass density during binary coalescence of particles
$\rho_{a:C-H}$	a:C-H film mass density
ρ_b	resistivity of plasma bulk
ρ_p^e	electron density of a particle
ρ_p	particle mass density
ρ_G	graphite mass density
σ_{ext}	extinction cross section
σ_{eAr}^m	electron-Ar momentum loss cross section
σ_{eAr}^{tot}	total electron-Ar collision cross section
σ_{eC}^m	Coulomb collision cross section
σ_{ej}^m	electron-j momentum loss cross section
σ_{ep}^m	electron-particle momentum loss cross section
σ_{nn}^{coll}	particle-particle collision cross section
σ_p	geometric particle cross section
$\sigma_{ph,a}$	photoabsorption cross section
$\sigma_{ph,d}$	photodetachment cross section
ϕ_{RF}	(absolute) phase angle between
...	the 1st harmonics of RF-current and -voltage
Φ	electrical potential (general)
Φ_c	cloud potential
Φ_f	floating potential
Φ_p	plasma potential
τ	optical depth
τ_c	characteristic time for the coalescence of two particles
τ_{coll}	characteristic time between the collision of two particles
τ_{rad}	radiative life time
ω	angular frequency (general)
$\omega_{p,e}$	electron plasma frequency

$\omega_{p,i}$

ion plasma frequency

Bibliography

- [1] Alfred Grill. “Plasma enhanced chemical vapor deposited SiCOH dielectrics: from low-k to extreme low-k interconnect materials”. In: *Journal of Applied Physics* 93.3 (2003), pp. 1785–1790. DOI: 10.1063/1.1534628.
- [2] Henri Jansen et al. “A survey on the reactive ion etching of silicon in microtechnology”. In: *Journal of Micromechanics and Microengineering* 6.1 (1996), p. 14. DOI: 10.1088/0960-1317/6/1/002.
- [3] J. Tendys et al. “Plasma immersion ion implantation using plasmas generated by radio frequency techniques”. In: *Applied Physics Letters* 53.22 (1988), pp. 2143–2145. DOI: 10.1063/1.100299.
- [4] K.-D. Weltmann et al. “Atmospheric Pressure Plasma Jet for Medical Therapy: Plasma Parameters and Risk Estimation”. In: *Contributions to Plasma Physics* 49.9 (2009), pp. 631–640. DOI: 10.1002/ctpp.200910067.
- [5] XinPei Lu et al. “A single electrode room-temperature plasma jet device for biomedical applications”. In: *Applied Physics Letters* 92.15 (2008), p. 151504. DOI: 10.1063/1.2912524.
- [6] J. F. Kolb et al. “Cold atmospheric pressure air plasma jet for medical applications”. In: *Applied Physics Letters* 92.24 (2008), p. 241501. DOI: 10.1063/1.2940325.
- [7] Gregory Fridman et al. “Applied Plasma Medicine”. In: *Plasma Processes and Polymers* 5.6 (2008), pp. 503–533. DOI: 10.1002/ppap.200700154.
- [8] M G Kong et al. “Plasma medicine: an introductory review”. In: *New Journal of Physics* 11.11 (2009), p. 115012. DOI: 10.1088/1367-2630/11/11/115012.
- [9] M. Gryaznevich et al. “Achievement of Record β in the START Spherical Tokamak”. In: *Phys. Rev. Lett.* 80.18 (1998), pp. 3972–3975. DOI: 10.1103/PhysRevLett.80.3972.

- [10] Thomas Sunn Pedersen et al. “Key results from the first plasma operation phase and outlook for future performance in Wendelstein 7-X”. In: *Physics of Plasmas* 24.5 (2017), p. 055503. DOI: 10.1063/1.4983629.
- [11] B. Lipschultz et al. “Operation of Alcator C-Mod with high-Z plasma facing components and implications”. In: *Physics of Plasmas* 13.5 (2006), p. 056117. DOI: 10.1063/1.2180767.
- [12] Gary S. Selwyn and Edward F. Patterson. “Plasma particulate contamination control. II. Self-cleaning tool design”. In: *Journal of Vacuum Science & Technology A: Vacuum, Surfaces, and Films* 10.4 (1992), pp. 1053–1059. DOI: 10.1116/1.578201.
- [13] Gary S. Selwyn. “Plasma particulate contamination control. I. Transport and process effects”. In: *Journal of Vacuum Science & Technology B: Microelectronics and Nanometer Structures Processing, Measurement, and Phenomena* 9.6 (1991), pp. 3487–3492. DOI: 10.1116/1.585829.
- [14] Gary S. Selwyn, John E. Heidenreich, and Kurt L. Haller. “Rastered laser light scattering studies during plasma processing: Particle contamination trapping phenomena”. In: *Journal of Vacuum Science & Technology A: Vacuum, Surfaces, and Films* 9.5 (1991), pp. 2817–2824. DOI: 10.1116/1.577207.
- [15] Bin Liu, J. Goree, and Yan Feng. “Non-Gaussian statistics and superdiffusion in a driven-dissipative dusty plasma”. In: *Phys. Rev. E* 78.4 (2008), p. 046403. DOI: 10.1103/PhysRevE.78.046403.
- [16] Zach Haralson and J. Goree. “Overestimation of Viscosity by the Green-Kubo Method in a Dusty Plasma Experiment”. In: *Phys. Rev. Lett.* 118.19 (2017), p. 195001. DOI: 10.1103/PhysRevLett.118.195001.
- [17] Chun-Shang Wong et al. “Strongly coupled plasmas obey the fluctuation theorem for entropy production”. In: *Nature Physics* 14 (2018), pp. 21–24. DOI: 10.1103/PhysRevLett.118.195001.
- [18] J Winter. “Dust in fusion devices - experimental evidence, possible sources and consequences”. In: *Plasma Physics and Controlled Fusion* 40.6 (1998), p. 1201. DOI: <http://stacks.iop.org/0741-3335/40/i=6/a=022>.

- [19] J Winter. “Dust in fusion devices—a multi-faceted problem connecting high- and low-temperature plasma physics”. In: *Plasma Physics and Controlled Fusion* 46.12B (2004), B583. DOI: <http://stacks.iop.org/0741-3335/46/i=12B/a=047>.
- [20] Mizuki Tateishi et al. “Real-time mass measurement of dust particles deposited on vessel wall in a divertor simulator using quartz crystal microbalances”. In: *Journal of Nuclear Materials* 463 (2015), pp. 865–868. DOI: <https://doi.org/10.1016/j.jnucmat.2014.10.049>.
- [21] Jan Schablinski et al. “Laser heating of finite two-dimensional dust clusters: A. Experiments”. In: *Physics of Plasmas* 19.1 (2012), p. 013705. DOI: 10.1063/1.3677356.
- [22] A. Melzer. “Mode spectra of thermally excited two-dimensional dust Coulomb clusters”. In: *Phys. Rev. E* 67.1 (2003), p. 016411. DOI: 10.1103/PhysRevE.67.016411.
- [23] R. A. Quinn and J. Goree. “Experimental investigation of particle heating in a strongly coupled dusty plasma”. In: *Physics of Plasmas* 7.10 (2000), pp. 3904–3911. DOI: 10.1063/1.1286988.
- [24] A Piel. “Plasma crystals: experiments and simulation”. In: *Plasma Physics and Controlled Fusion* 59.1 (2017), p. 014001. DOI: 10.1088/0741-3335/59/1/014001.
- [25] Th Wegner, C Küllig, and J Meichsner. “On the E-H transition in inductively coupled radio frequency oxygen plasmas: I. Density and temperature of electrons, ground state and singlet metastable molecular oxygen”. In: *Plasma Sources Science and Technology* 26.2 (2017), p. 025006. DOI: 10.1088/1361-6595/26/2/025006.
- [26] J Hopwood. “Review of inductively coupled plasmas for plasma processing”. In: *Plasma Sources Science and Technology* 1.2 (1992), p. 109. DOI: 10.1088/0963-0252/1/2/006.
- [27] Th. Enk and M. Krämer. “Radio frequency power deposition in a high-density helicon discharge with helical antenna coupling”. In: *Physics of Plasmas* 7.10 (2000), pp. 4308–4319. DOI: 10.1063/1.1288399.
- [28] C. Beneking. “Power dissipation in capacitively coupled rf discharges”. In: *Journal of Applied Physics* 68.9 (1990), pp. 4461–4473. DOI: 10.1063/1.346196.

- [29] J Schulze, E Schüngel, and U Czarnetzki. “The electrical asymmetry effect in capacitively coupled radio frequency discharges – measurements of dc self bias, ion energy and ion flux”. In: *Journal of Physics D: Applied Physics* 42.9 (2009), p. 092005. DOI: 10.1088/0022-3727/42/9/092005.
- [30] Rainer Hippler (Editor) et al. *Low Temperature Plasmas: Fundamentals, Technologies and Techniques*. 2nd ed. Vol. 1. Wiley-VCH, 2008. ISBN: 978-3-527-40673-9.
- [31] Gerhard Franz. *Low Pressure Plasmas and Microstructuring Technology*. 1st ed. Springer-Verlag Berlin Heidelberg, 2009. DOI: 10.1007/978-3-540-85849-2.
- [32] Alexander Piel. *Plasma Physics: An Introduction to Laboratory, Space, and Fusion Plasmas*. 1st ed. Springer-Verlag Berlin Heidelberg, 2010. DOI: 10.1007/978-3-540-85849-2.
- [33] Riccardo d’Agostino et al. “Low-Temperature Plasma Processing of Materials: Past, Present, and Future”. In: *Plasma Processes and Polymers* 2.1 (2005), pp. 7–15. DOI: 10.1002/ppap.200400074.
- [34] H Conrads and M Schmidt. “Plasma generation and plasma sources”. In: *Plasma Sources Science and Technology* 9.4 (2000), p. 441. DOI: 10.1088/0963-0252/9/4/301.
- [35] C.D. Child. In: *Phys. Rev.* 32 (1911), p. 498.
- [36] I. Langmuir. In: *Phys. Rev.* 2 (1913), p. 450.
- [37] M.A. Lieberman. “Analytical solution for capacitive RF sheath”. In: *IEEE Transactions on Plasma Science* 16.6 (1988), pp. 638–644. DOI: 10.1109/27.16552.
- [38] M.A. Lieberman. “Dynamics of a collisional, capacitive RF sheath”. In: *IEEE Transactions on Plasma Science* 17.2 (1989), pp. 338–341. DOI: 10.1109/27.24645.
- [39] A. A. Fridman et al. “Dusty plasma formation: Physics and critical phenomena. Theoretical approach”. In: *Journal of Applied Physics* 79.3 (1996), pp. 1303–1314. DOI: 10.1063/1.361026.
- [40] Y Watanabe. “Formation and behaviour of nano/micro-particles in low pressure plasmas”. In: *Journal of Physics D: Applied Physics* 39.19 (2006), R329. DOI: 10.1088/0022-3727/39/19/R01.

- [41] Ming Mao et al. “New pathways for nanoparticle formation in acetylene dusty plasmas: a modelling investigation and comparison with experiments”. In: *Journal of Physics D: Applied Physics* 41.22 (2008), p. 225201. DOI: 10.1088/0022-3727/41/22/225201.
- [42] Kathleen De Bleecker, Annemie Bogaerts, and Wim Goedheer. “Detailed modeling of hydrocarbon nanoparticle nucleation in acetylene discharges”. In: *Phys. Rev. E* 73.2 (2006), p. 026405. DOI: 10.1103/PhysRevE.73.026405.
- [43] Kathleen De Bleecker, Annemie Bogaerts, and Wim Goedheer. “Aromatic ring generation as a dust precursor in acetylene discharges”. In: *Applied Physics Letters* 88.15 (2006), p. 151501. DOI: 10.1063/1.2193796.
- [44] L C J Heijmans, F M J H van de Wetering, and S Nijdam. “Comment on ‘The effect of single-particle charge limits on charge distributions in dusty plasmas’”. In: *Journal of Physics D: Applied Physics* 49.38 (2016), p. 388001. DOI: 10.1088/0022-3727/49/38/388001.
- [45] F. X. Bronold et al. “Towards a Microscopic Theory of Particle Charging”. In: *Contributions to Plasma Physics* 49.4 (2009), pp. 303–315. DOI: 10.1002/ctpp.200910028.
- [46] Yu. Tyshetskiy and S. V. Vladimirov. “Quantum-tunneling-enhanced charging of nanoparticles in plasmas”. In: *Phys. Rev. E* 83.4 (2011), p. 046406. DOI: 10.1103/PhysRevE.83.046406.
- [47] A. V. Filippov et al. “Ultrahigh charging of dust particles in a nonequilibrium plasma”. In: *JETP Letters* 86.1 (2007), pp. 14–19. DOI: 10.1134/S0021364007130048.
- [48] O. Havnes. “Charges on dust particles”. In: *Advances in Space Research* 4.9 (1984), pp. 75–83. DOI: [https://doi.org/10.1016/0273-1177\(84\)90010-3](https://doi.org/10.1016/0273-1177(84)90010-3).
- [49] A M Hinz et al. “Versatile particle collection concept for correlation of particle growth and discharge parameters in dusty plasmas”. In: *Journal of Physics D: Applied Physics* 48.5 (2015), p. 055203. DOI: 10.1088/0022-3727/48/5/055203.
- [50] L. Boufendi et al. “Detection of particles of less than 5 nm in diameter formed in an argon–silane capacitively coupled radio-frequency discharge”. In: *Applied Physics Letters* 79.26 (2001), pp. 4301–4303. DOI: 10.1063/1.1425431.

- [51] F. M. J. H. van de Wetering, S. Nijdam, and J. Beckers. “Conclusive evidence of abrupt coagulation inside the void during cyclic nanoparticle formation in reactive plasma”. In: *Applied Physics Letters* 109.4 (2016), p. 043105. DOI: 10.1063/1.4959835.
- [52] J-C Schauer, S Hong, and J Winter. “Electrical measurements in dusty plasmas as a detection method for the early phase of particle formation”. In: *Plasma Sources Science and Technology* 13.4 (2004), p. 636. DOI: 10.1088/0963-0252/13/4/012.
- [53] Mark A. Sobolewski. “Electrical characterization of radio-frequency discharges in the Gaseous Electronics Conference Reference Cell”. In: *Journal of Vacuum Science & Technology A: Vacuum, Surfaces, and Films* 10.6 (1992), pp. 3550–3562. DOI: 10.1116/1.577783.
- [54] Gaëtan Wattieaux and Laïfa Boufendi. “Discharge impedance evolution, stray capacitance effect, and correlation with the particles size in a dusty plasma”. In: *Physics of Plasmas* 19.3 (2012), p. 033701. DOI: 10.1063/1.3689013.
- [55] U Fantz. “Basics of plasma spectroscopy”. In: *Plasma Sources Science and Technology* 15.4 (2006), S137. DOI: 10.1088/0963-0252/15/4/S01.
- [56] M Mikikian et al. “Optical diagnostics of dusty plasmas during nanoparticle growth”. In: *Plasma Physics and Controlled Fusion* 59.1 (2017), p. 014034. DOI: 10.1088/0741-3335/59/1/014034.
- [57] Vladimir Sushkov, Ann-Pierra Herrendorf, and Rainer Hippler. “Metastable argon atom density in complex argon/acetylene plasmas determined by means of optical absorption and emission spectroscopy”. In: *Journal of Physics D: Applied Physics* 49.42 (2016), p. 425201. DOI: 10.1088/0022-3727/49/42/425201.
- [58] V M Donnelly. “Plasma electron temperatures and electron energy distributions measured by trace rare gases optical emission spectroscopy”. In: *Journal of Physics D: Applied Physics* 37.19 (2004), R217. DOI: 10.1088/0022-3727/37/19/R01.
- [59] J. Hopwood and J. Asmussen. “Neutral gas temperatures in a multipolar electron cyclotron resonance plasma”. In: *Applied Physics Letters* 58.22 (1991), pp. 2473–2475. DOI: 10.1063/1.105232.
- [60] Jean-Paul Booth et al. “Time-resolved electric-field measurements in 30 kHz hydrogen discharges by optical emission Stark spectroscopy”. In: *Journal of Applied Physics* 74.2 (1993), pp. 862–867. DOI: 10.1063/1.354878.

- [61] H Nassar et al. “N 2 + /N 2 ratio and temperature measurements based on the first negative N 2 + and second positive N 2 overlapped molecular emission spectra”. In: *Journal of Physics D: Applied Physics* 37.14 (2004), p. 1904. DOI: 10.1088/0022-3727/37/14/005.
- [62] H. R. Griem. *Principles of Plasma Spectroscopy*. Cambridge University Press, 2009. DOI: 10.1017/CB09780511524578.
- [63] Jürgen H Gross. *Mass Spectrometry*. 3rd ed. Springer International Publishing, 2017. DOI: 10.1007/978-3-319-54398-7.
- [64] Edmond de Hoffmann and Vincent Stroobant. *Mass Spectrometry: Principles and Applications*. 3rd ed. Wiley-VCH, 2007. ISBN: 978-0-470-03310-4.
- [65] Valery Godyak. “Comments on plasma diagnostics with microwave probes”. In: *Physics of Plasmas* 24.6 (2017), p. 060702. DOI: 10.1063/1.4984781.
- [66] I. Langmuir and H. Mott-Smith. In: *Gen. Elec. Rev.* 27 (1926), p. 449.
- [67] M. Lapke, T. Mussenbrock, and R. P. Brinkmann. “The multipole resonance probe: A concept for simultaneous determination of plasma density, electron temperature, and collision rate in low-pressure plasmas”. In: *Applied Physics Letters* 93.5 (2008), p. 051502. DOI: 10.1063/1.2966351.
- [68] Martin Lapke et al. “The multipole resonance probe: characterization of a prototype”. In: *Plasma Sources Science and Technology* 20.4 (2011), p. 042001. DOI: 10.1088/0963-0252/20/4/042001.
- [69] M. K. Hedayati et al. “Plasmonic tunable metamaterial absorber as ultraviolet protection film”. In: *Applied Physics Letters* 104.4 (2014), p. 041103. DOI: 10.1063/1.4863202.
- [70] A. Biswas et al. “Tunable multiple plasmon resonance wavelengths response from multicomponent polymer-metal nanocomposite systems”. In: *Applied Physics Letters* 84.14 (2004), pp. 2655–2657. DOI: 10.1063/1.1697626.
- [71] Ulrich Schuermann et al. “Controlled syntheses of Ag–polytetrafluoroethylene nanocomposite thin films by co-sputtering from two magnetron sources”. In: *Nanotechnology* 16.8 (2005), p. 1078. DOI: 10.1088/0957-4484/16/8/014.
- [72] Wolfgang Haiss et al. “Determination of Size and Concentration of Gold Nanoparticles from UV-Vis Spectra”. In: *Analytical Chemistry* 79.11 (2007), pp. 4215–4221. DOI: 10.1021/ac0702084.

- [73] Vincenzo Amendola and Moreno Meneghetti. “Size Evaluation of Gold Nanoparticles by UV-vis Spectroscopy”. In: *The Journal of Physical Chemistry C* 113.11 (2009), pp. 4277–4285. DOI: 10.1021/jp8082425.
- [74] Dipak Kumar Bhui et al. “Synthesis and UV-vis spectroscopic study of silver nanoparticles in aqueous SDS solution”. In: *Journal of Molecular Liquids* 145.1 (2009), pp. 33–37. DOI: <https://doi.org/10.1016/j.molliq.2008.11.014>.
- [75] H. Moosmueller, R.K. Chakrabarty, and W.P. Arnott. “Aerosol light absorption and its measurement: A review”. In: *Journal of Quantitative Spectroscopy and Radiative Transfer* 110.11 (2009), pp. 844–878. DOI: <https://doi.org/10.1016/j.jqsrt.2009.02.035>.
- [76] Carsten Killer et al. “Long-term spatio-temporal evolution of the dust distribution in dusty argon rf plasmas”. In: *Plasma Sources Science and Technology* 25.5 (2016), p. 055004. DOI: 10.1088/0963-0252/25/5/055004.
- [77] J. Bolze et al. “Formation and Growth of Amorphous Colloidal CaCO₃ Precursor Particles as Detected by Time-Resolved SAXS”. In: *Langmuir* 18.22 (2002), pp. 8364–8369. DOI: 10.1021/1a025918d.
- [78] D. Pontoni, T. Narayanan, and A. R. Rennie. “Time-Resolved SAXS Study of Nucleation and Growth of Silica Colloids”. In: *Langmuir* 18.1 (2002), pp. 56–59. DOI: 10.1021/1a015503c.
- [79] Holger Borchert et al. “Determination of Nanocrystal Sizes: A Comparison of TEM, SAXS, and XRD Studies of Highly Monodisperse CoPt₃ Particles”. In: *Langmuir* 21.5 (2005), pp. 1931–1936. DOI: 10.1021/1a0477183.
- [80] D. I. Svergun et al. “Protein hydration in solution: Experimental observation by x-ray and neutron scattering”. In: *Proceedings of the National Academy of Sciences* 95.5 (1998), pp. 2267–2272.
- [81] Fajun Zhang et al. “Protein Interactions Studied by SAXS: Effect of Ionic Strength and Protein Concentration for BSA in Aqueous Solutions”. In: *The Journal of Physical Chemistry B* 111.1 (2007), pp. 251–259. DOI: 10.1021/jp0649955.
- [82] Greg L Hura et al. “Robust, high-throughput solution structural analyses by small angle X-ray scattering (SAXS)”. In: *Nature Methods* 6 (2009), pp. 606–612. DOI: 10.1038/nmeth.1353.
- [83] L.A. Feigin and D.I. Svergun. *Structure Analysis by Small-Angle X-Ray and Neutron Scattering*. 1st ed. Springer US, 1987. DOI: 10.1007/978-1-4757-6624-0.

- [84] Ludwig Reimer. *Scanning Electron Microscopy: Physics of Image Formation and Microanalysis*. 2nd ed. Springer-Verlag Berlin Heidelberg, 1998. DOI: 10.1007/978-3-540-38967-5.
- [85] Joseph I. Goldstein et al. *Scanning Electron Microscopy and X-Ray Microanalysis*. 4th ed. Springer-Verlag New York, 2018. DOI: 10.1007/978-1-4939-6676-9.
- [86] Ludwig Reimer and Helmut Kohl. *Transmission Electron Microscopy: Physics of Image Formation*. 5th ed. Springer-Verlag New York, 2008. DOI: 10.1007/978-0-387-40093-8.
- [87] David B. Williams and C. Barry Carter. *Transmission Electron Microscopy: A Textbook for Materials Science*. 2nd ed. Springer US, 2009. DOI: 10.1007/978-0-387-76501-3.
- [88] Adeline Buffet et al. “P03, the microfocus and nanofocus X-ray scattering (MiNaXS) beamline of the PETRA III storage ring: the microfocus endstation”. In: *Journal of Synchrotron Radiation* 19.4 (July 2012), pp. 647–653. DOI: 10.1107/S0909049512016895.
- [89] J.K. Olthoff and K. E. Greenberg. “The Gaseous Electronics Conference RF Reference Cell—An Introduction”. In: *Journal of Research of the National Institute of Standards and Technology* 100.4 (1995), pp. 327–339. DOI: 10.6028/jres.100.025.
- [90] Morten Hundt et al. “Real-time monitoring of nucleation-growth cycle of carbon nanoparticles in acetylene plasmas”. In: *Journal of Applied Physics* 109.12 (2011), p. 123305. DOI: 10.1063/1.3599893.
- [91] Th. Wegner et al. “Influence of nanoparticle formation on discharge properties in argon-acetylene capacitively coupled radio frequency plasmas”. In: *Applied Physics Letters* 108.6 (2016), p. 063108. DOI: 10.1063/1.4941806.
- [92] P D Haaland et al. “On form and flow in dusty plasmas”. In: *Plasma Sources Science and Technology* 3.3 (1994), p. 381. DOI: 10.1088/0963-0252/3/3/022.
- [93] A Garscadden et al. “Overview of growth and behaviour of clusters and particles in plasmas”. In: *Plasma Sources Science and Technology* 3.3 (1994), p. 239. DOI: 10.1088/0963-0252/3/3/001.
- [94] Eva Kovačević et al. “Infrared fingerprints and periodic formation of nanoparticles in Ar/C₂H₂ plasmas”. In: *Journal of Applied Physics* 93.5 (2003), pp. 2924–2930. DOI: 10.1063/1.1541118.

- [95] F. M. J. H. van de Wetering, S. Nijdam, and J. Beckers. “Conclusive evidence of abrupt coagulation inside the void during cyclic nanoparticle formation in reactive plasma”. In: *Applied Physics Letters* 109.4 (2016), p. 043105. DOI: 10.1063/1.4959835.
- [96] J Beckers, W W Stoffels, and G M W Kroesen. “Temperature dependence of nucleation and growth of nanoparticles in low pressure Ar/CH₄ RF discharges”. In: *Journal of Physics D: Applied Physics* 42.15 (2009), p. 155206. DOI: 10.1088/0022-3727/42/15/155206.
- [97] J. Beckers and G. M. W. Kroesen. “Surprising temperature dependence of the dust particle growth rate in low pressure Ar/C₂H₂ plasmas”. In: *Applied Physics Letters* 99.18 (2011), p. 181503. DOI: 10.1063/1.3658730.
- [98] C. Y. Robert Wu, F. Z. Chen, and D. L. Judge. “Measurements of temperature-dependent absorption cross sections of C₂H₂ in the VUV-UV region”. In: *Journal of Geophysical Research: Planets* 106.E4 (2001), pp. 7629–7636. DOI: 10.1029/2000JE001292.
- [99] Marjan Khamesian et al. “Study of the radiative electron attachment and photodetachment processes for the C₂H/C₂H⁻ and C₄H/C₄H⁻ molecules”. In: *The European Physical Journal D* 70.11 (2016), p. 240. DOI: 10.1140/epjd/e2016-70138-1.
- [100] Nicolas Douguet, Viatcheslav Kokoouline, and Ann E. Orel. “Photodetachment cross sections of the C_{2n}H⁻ ($n = 1 - 3$) hydrocarbon-chain anions”. In: *Phys. Rev. A* 90.6 (2014), p. 063410. DOI: 10.1103/PhysRevA.90.063410.
- [101] F M J H van de Wetering et al. “Fast and interrupted expansion in cyclic void growth in dusty plasma”. In: *Journal of Physics D: Applied Physics* 48.3 (2015), p. 035204. DOI: 10.1088/0022-3727/48/3/035204.
- [102] Marjorie Cavarroc et al. “Successive Generations of Dust in Complex Plasmas: A Cyclic Phenomenon in the Void Region”. In: *Phys. Rev. Lett.* 100.4 (2008), p. 045001. DOI: 10.1103/PhysRevLett.100.045001.
- [103] Maxime Mikikian et al. “Dust particles in low-pressure plasmas: Formation and induced phenomena”. In: *Pure and Applied Chemistry* 82.6 (2010), pp. 1273–1282. DOI: 10.1351/PAC-CON-09-10-30.
- [104] V Land and W J Goedheer. “The plasma inside a dust free void: hotter, denser, or both?” In: *New Journal of Physics* 9.8 (2007), p. 246. DOI: 10.1088/1367-2630/9/8/246.

- [105] D. Samsonov and J. Goree. “Instabilities in a dusty plasma with ion drag and ionization”. In: *Phys. Rev. E* 59.1 (1999), pp. 1047–1058. DOI: 10.1103/PhysRevE.59.1047.
- [106] Ilija Stefanović et al. “Plasma density measurements in a developing void”. In: *IEEE Transactions on Plasma Science* 36.4 (2008), pp. 1018–1019. DOI: 10.1109/TPS.2008.924620.
- [107] Mehdi Keshavarz Hedayati et al. “Design of a Perfect Black Absorber at Visible Frequencies Using Plasmonic Metamaterials”. In: *Advanced Materials* 23.45 (2011), pp. 5410–5414. DOI: 10.1002/adma.201102646.
- [108] Chloé Minnai and Paolo Milani. “Metal-polymer nanocomposite with stable plasmonic tuning under cyclic strain conditions”. In: *Applied Physics Letters* 107.7 (2015), p. 073106. DOI: 10.1063/1.4928725.
- [109] Ch Deschenaux et al. “Investigations of CH₄, C₂H₂ and C₂H₄ dusty RF plasmas by means of FTIR absorption spectroscopy and mass spectrometry”. In: *Journal of Physics D: Applied Physics* 32.15 (1999), p. 1876. DOI: 10.1088/0022-3727/32/15/316.
- [110] J Perrin et al. “Possible routes for cluster growth and particle formation in RF silane discharges”. In: *Plasma Sources Science and Technology* 3.3 (1994), p. 252. DOI: 10.1088/0963-0252/3/3/003.
- [111] C Courteille et al. “Partial-depth modulation study of anions and neutrals in low-pressure silane plasmas”. In: *Plasma Sources Science and Technology* 5.2 (1996), p. 210. DOI: 10.1088/0963-0252/5/2/014.
- [112] Kathleen De Bleecker, Annemie Bogaerts, and Wim Goedheer. “Modeling of the formation and transport of nanoparticles in silane plasmas”. In: *Phys. Rev. E* 70.5 (2004), p. 056407. DOI: 10.1103/PhysRevE.70.056407.
- [113] Seung J. Choi and Mark J. Kushner. “The role of negative ions in the formation of particles in low-pressure plasmas”. In: *Journal of Applied Physics* 74.2 (1993), pp. 853–861. DOI: 10.1063/1.354877.
- [114] A A Howling et al. “Negative hydrogenated silicon ion clusters as particle precursors in RF silane plasma deposition experiments”. In: *Journal of Physics D: Applied Physics* 26.6 (1993), p. 1003. DOI: 10.1088/0022-3727/26/6/019.

- [115] I Stefanović et al. “Development of voids in pulsed and CW- driven reactive plasmas with large nanoparticle density”. In: *Journal of Physics D: Applied Physics* 48.38 (2015), p. 385202. DOI: 10.1088/0022-3727/48/38/385202.
- [116] Benjamin Tadsen, Franko Greiner, and Alexander Piel. “Preparation of magnetized nanodusty plasmas in a radio frequency-driven parallel-plate reactor”. In: *Physics of Plasmas* 21.10 (2014), p. 103704. DOI: 10.1063/1.4897169.
- [117] G. Praburam and J. Goree. “Experimental observation of very low-frequency macroscopic modes in a dusty plasma”. In: *Physics of Plasmas* 3.4 (1996), pp. 1212–1219. DOI: 10.1063/1.871745.
- [118] Kurt Sonderegger et al. “Very fast-opening UHV gate valve”. In: *Journal of Vacuum Science & Technology A: Vacuum, Surfaces, and Films* 31.6 (2013), p. 060601. DOI: 10.1116/1.4813836.
- [119] Uwe Kortshagen. “Nonthermal plasma synthesis of semiconductor nanocrystals”. In: *Journal of Physics D: Applied Physics* 42.11 (2009), p. 113001. DOI: 10.1088/0022-3727/42/11/113001.
- [120] Lorenzo Mangolini and Uwe Kortshagen. “Selective nanoparticle heating: Another form of nonequilibrium in dusty plasmas”. In: *Phys. Rev. E* 79.2 (2009), p. 026405. DOI: 10.1103/PhysRevE.79.026405.
- [121] H R Maurer and H Kersten. “On the heating of nano- and microparticles in process plasmas”. In: *Journal of Physics D: Applied Physics* 44.17 (2011), p. 174029. DOI: 10.1088/0022-3727/44/17/174029.
- [122] Suk-Ho Hong and Jörg Winter. “Size dependence of optical properties and internal structure of plasma grown carbonaceous nanoparticles studied by in situ Rayleigh-Mie scattering ellipsometry”. In: *Journal of Applied Physics* 100.6 (2006), p. 064303. DOI: 10.1063/1.2338132.
- [123] Eva Kovacevic et al. “Size dependent characteristics of plasma synthesized carbonaceous nanoparticles”. In: *Journal of Applied Physics* 112.1 (2012), p. 013303. DOI: 10.1063/1.4731751.
- [124] F. X. Bronold, H. Deutsch, and H. Fehske. “Physisorption kinetics of electrons at plasma boundaries”. In: *The European Physical Journal D* 54.3 (2009), pp. 519–544. DOI: 10.1140/epjd/e2009-00213-7.
- [125] F. X. Bronold et al. “Surface States and the Charge of a Dust Particle in a Plasma”. In: *Phys. Rev. Lett.* 101.17 (2008), p. 175002. DOI: 10.1103/PhysRevLett.101.175002.

- [126] K. J. Laidler, S. Glasstone, and H. Eyring. “Application of the Theory of Absolute Reaction Rates to Heterogeneous Processes I. The Adsorption and Desorption of Gases”. In: *The Journal of Chemical Physics* 8.9 (1940), pp. 659–667. DOI: 10.1063/1.1750736.
- [127] P. Oelhafen et al. “Electron spectroscopy study of hydrogenated amorphous carbon films formed by methane ion beam deposition”. In: *Thin Solid Films* 120.3 (1984), pp. 231–238. DOI: [https://doi.org/10.1016/0040-6090\(84\)90299-2](https://doi.org/10.1016/0040-6090(84)90299-2).
- [128] Chunshi Cui and John Goree. “Fluctuations of the charge on a dust grain in a plasma”. In: *IEEE Transactions on Plasma Science* 22.2 (1994), pp. 151–158. DOI: 10.1109/27.279018.
- [129] P. A. Thrower and R. M. Mayer. “Point defects and self-diffusion in graphite”. In: *physica status solidi (a)* 47.1 (1978), pp. 11–37. DOI: 10.1002/pssa.2210470102.
- [130] H. Bracht, E. E. Haller, and R. Clark-Phelps. “Silicon Self-Diffusion in Isotope Heterostructures”. In: *Phys. Rev. Lett.* 81.2 (1998), pp. 393–396. DOI: 10.1103/PhysRevLett.81.393.
- [131] Y.-W. Mo et al. “Surface self-diffusion of Si on Si(001)”. In: *Surface Science* 268.1 (1992), pp. 275–295. DOI: [https://doi.org/10.1016/0039-6028\(92\)90968-C](https://doi.org/10.1016/0039-6028(92)90968-C).
- [132] M. José-Yacamán et al. “Surface Diffusion and Coalescence of Mobile Metal Nanoparticles”. In: *The Journal of Physical Chemistry B* 109.19 (2005), pp. 9703–9711. DOI: 10.1021/jp0509459.
- [133] J. Robertson. “Amorphous carbon”. In: *Advances in Physics* 35.4 (1986), pp. 317–374. DOI: 10.1080/00018738600101911.
- [134] Martin Linck et al. “Chromatic Aberration Correction for Atomic Resolution TEM Imaging from 20 to 80 kV”. In: *Phys. Rev. Lett.* 117.7 (2016), p. 076101. DOI: 10.1103/PhysRevLett.117.076101.
- [135] Mhairi H. Gass et al. “Four-Dimensional Spectral Tomography of Carbonaceous Nanocomposites”. In: *Nano Letters* 6.3 (2006), pp. 376–379. DOI: 10.1021/nl052120g.
- [136] F M J H van de Wetering et al. “Laser-induced incandescence applied to dusty plasmas”. In: *Journal of Physics D: Applied Physics* 49.29 (2016), p. 295206. DOI: 10.1088/0022-3727/49/29/295206.
- [137] L. Boufendi et al. “Study of initial dust formation in an Ar-SiH₄ discharge by laser induced particle explosive evaporation”. In: *Journal of Applied Physics* 76.1 (1994), pp. 148–153. DOI: 10.1063/1.357120.

- [138] H. R. Maurer, R. Basner, and H. Kersten. “Temperature of Particulates in Low-Pressure rf-Plasmas in Ar, Ar/H₂ and Ar/N₂ Mixtures”. In: *Contributions to Plasma Physics* 50.10 (2010), pp. 954–961. DOI: 10.1002/ctpp.201000022.
- [139] Horst Maurer, Ralf Basner, and Holger Kersten. “Measuring the temperature of microparticles in plasmas”. In: *Review of Scientific Instruments* 79.9 (2008), p. 093508. DOI: 10.1063/1.2987688.
- [140] H. R. Maurer et al. “Measurement of plasma-surface energy fluxes in an argon rf-discharge by means of calorimetric probes and fluorescent microparticles”. In: *Physics of Plasmas* 17.11 (2010), p. 113707. DOI: 10.1063/1.3484876.
- [141] J P Feist, A L Heyes, and J R Nicholls. “Phosphor thermometry in an electron beam physical vapour deposition produced thermal barrier coating doped with dysprosium”. In: *Proceedings of the Institution of Mechanical Engineers, Part G: Journal of Aerospace Engineering* 215.6 (2001), pp. 333–341. DOI: 10.1243/0954410011533338.
- [142] Jeffrey I. Eldridge et al. “Depth-penetrating temperature measurements of thermal barrier coatings incorporating thermographic phosphors”. In: *Journal of Thermal Spray Technology* 13.1 (2004), pp. 44–50. DOI: 10.1007/s11666-004-0048-0.
- [143] Mikhail V. Dutka et al. “On the formation of copper nanoparticles in nanocluster aggregation source”. In: *Journal of Vacuum Science & Technology A: Vacuum, Surfaces, and Films* 33.3 (2015), p. 031509. DOI: 10.1116/1.4917002.
- [144] Panagiotis Grammatikopoulos et al. “Kinetic trapping through coalescence and the formation of patterned Ag-Cu nanoparticles”. In: *Nanoscale* 8.18 (2016), pp. 9780–9790. DOI: 10.1039/C5NR08256K.
- [145] S Hong, J Berndt, and J Winter. “Growth precursors and dynamics of dust particle formation in the Ar/CH₄ and Ar/C₂H₂ plasmas”. In: *Plasma Sources Science and Technology* 12.1 (2003), p. 46. DOI: 10.1088/0963-0252/12/1/306.
- [146] F. M. J. H. van de Wetering et al. “Interaction of nanosecond ultraviolet laser pulses with reactive dusty plasma”. In: *Applied Physics Letters* 108.21 (2016), p. 213103. DOI: 10.1063/1.4952616.
- [147] S. Barbosa et al. “An introduction to light extinction spectrometry as a diagnostic for dust particle characterisation in dusty plasmas”. In: *Journal of Plasma Physics* 82.4 (2016), p. 615820403. DOI: 10.1017/S0022377816000714.

- [148] Masaharu Shiratani et al. “In situ polarization-sensitive laser-light-scattering method for simultaneous measurements of two-dimensional spatial size and density distributions of particles in plasmas”. In: *Journal of Vacuum Science & Technology A: Vacuum, Surfaces, and Films* 14.2 (1996), pp. 603–607. DOI: 10.1116/1.580152.
- [149] Tsuyoshi Fukuzawa et al. “Detection of particles in rf silane plasmas using photoemission method”. In: *Journal of Applied Physics* 80.6 (1996), pp. 3202–3207. DOI: 10.1063/1.363273.
- [150] A. Kramida et al. NIST Atomic Spectra Database (ver. 5.5.3), [Online]. Available: <https://physics.nist.gov/asd> [2018, March 30]. National Institute of Standards and Technology, Gaithersburg, MD, 2018.
- [151] John B. Boffard et al. “Electron-impact excitation of argon: Optical emission cross sections in the range of 300–2500nm”. In: *Atomic Data and Nuclear Data Tables* 93.6 (2007), pp. 831–863. DOI: <https://doi.org/10.1016/j.adt.2007.06.004>.
- [152] Benjamin Tadsen et al. “Self-excited dust-acoustic waves in an electron-depleted nanodusty plasma”. In: *Physics of Plasmas* 22.11 (2015), p. 113701. DOI: 10.1063/1.4934927.
- [153] F J Gordillo-Vázquez, M Camero, and C Gómez-Aleixandre. “Spectroscopic measurements of the electron temperature in low pressure radiofrequency Ar/H₂/C₂H₂ and Ar/H₂/CH₄ plasmas used for the synthesis of nanocarbon structures”. In: *Plasma Sources Science and Technology* 15.1 (2006), p. 42. DOI: 10.1088/0963-0252/15/1/007.
- [154] N Bilik et al. “Langmuir probe measurements of electron energy probability functions in dusty plasmas”. In: *Journal of Physics D: Applied Physics* 48.10 (2015), p. 105204. DOI: <http://stacks.iop.org/0022-3727/48/i=10/a=105204>.
- [155] I. B. Denysenko, H. Kersten, and N. A. Azarenkov. “Electron energy distribution in a dusty plasma: Analytical approach”. In: *Phys. Rev. E* 92.3 (2015), p. 033102. DOI: 10.1103/PhysRevE.92.033102.
- [156] E. Thomas Jr., K. Avinash, and R. L. Merlino. “Probe induced voids in a dusty plasma”. In: *Physics of Plasmas* 11.5 (2004), pp. 1770–1774. DOI: 10.1063/1.1688333.
- [157] C. O. Thompson, N. D’Angelo, and R. L. Merlino. “The interaction of stationary and moving objects with dusty plasmas”. In: *Physics of Plasmas* 6.5 (1999), pp. 1421–1426. DOI: 10.1063/1.873392.

- [158] M. Klindworth et al. “Dust-Free Regions around Langmuir Probes in Complex Plasmas under Microgravity”. In: *Phys. Rev. Lett.* 93.19 (2004), p. 195002. DOI: 10.1103/PhysRevLett.93.195002.
- [159] Private communication with M. Oberberg from the Ruhr Universität Bochum. 2017.
- [160] J I Fernández Palop et al. “Sheath structure in electronegative plasmas”. In: *Plasma Sources Science and Technology* 16.1 (2007), S76. DOI: 10.1088/0963-0252/16/1/S08.
- [161] J. P. Boeuf and Ph. Belenger. “Transition from a capacitive to a resistive regime in a silane radio frequency discharge and its possible relation to powder formation”. In: *Journal of Applied Physics* 71.10 (1992), pp. 4751–4754. DOI: 10.1063/1.350666.
- [162] Y Nakamura and M Kurachi. “Electron transport parameters in argon and its momentum transfer cross section”. In: *Journal of Physics D: Applied Physics* 21.5 (1988), p. 718. DOI: 10.1088/0022-3727/21/5/008.
- [163] S. A. Khrapak et al. “Scattering in the Attractive Yukawa Potential in the Limit of Strong Interaction”. In: *Phys. Rev. Lett.* 90.22 (2003), p. 225002. DOI: 10.1103/PhysRevLett.90.225002.
- [164] Márton Lampe et al. “Trapped ion effect on shielding, current flow, and charging of a small object in a plasma”. In: *Physics of Plasmas* 10.5 (2003), pp. 1500–1513. DOI: 10.1063/1.1562163.
- [165] Mark A. Sobolewski. “Electrical characterization of radio-frequency discharges in the Gaseous Electronics Conference Reference Cell”. In: *Journal of Vacuum Science & Technology A: Vacuum, Surfaces, and Films* 10.6 (1992), pp. 3550–3562. DOI: 10.1116/1.577783.
- [166] Shigeru Kakuta et al. “Influence of frequency, pressure, and mixture ratio of electronegative gas on electrical characteristics of rf discharges in N₂-SF₆ mixtures”. In: *Journal of Applied Physics* 74.8 (1993), pp. 4923–4931. DOI: 10.1063/1.354326.
- [167] Richard A. Gottscho. “Glow-discharge sheath electric fields: Negative-ion, power, and frequency effects”. In: *Phys. Rev. A* 36.5 (1987), pp. 2233–2242. DOI: 10.1103/PhysRevA.36.2233.
- [168] W. W. Stoffels et al. “Electron density fluctuations in a dusty Ar/SiH₄ rf discharge”. In: *Journal of Applied Physics* 78.8 (1995), pp. 4867–4872. DOI: 10.1063/1.359774.

- [169] I Stefanović et al. “Influence of nanoparticle formation on the time and the space resolved metastable density in argon-acetylene plasmas”. In: *Plasma Sources Science and Technology* 26.6 (2017), p. 065014. DOI: 10.1088/1361-6595/aa6f9c.
- [170] Robert B. Brode. “The Quantitative Study of the Collisions of Electrons with Atoms”. In: *Rev. Mod. Phys.* 5.4 (1933), pp. 257–279. DOI: 10.1103/RevModPhys.5.257.
- [171] Evangelos Gogolides and Herbert H. Sawin. “Continuum modeling of radio-frequency glow discharges. I. Theory and results for electropositive and electronegative gases”. In: *Journal of Applied Physics* 72.9 (1992), pp. 3971–3987. DOI: 10.1063/1.352250.
- [172] William M. Irvine. “Light Scattering by Spherical Particles: Radiation Pressure, Asymmetry Factor, and Extinction Cross Section”. In: *J. Opt. Soc. Am.* 55.1 (1965), pp. 16–21. DOI: 10.1364/JOSA.55.000016.
- [173] Sebastian Groth et al. “Kinetic Mie ellipsometry to determine the time-resolved particle growth in nanodusty plasmas”. In: *Journal of Physics D: Applied Physics* 48.46 (2015), p. 465203. DOI: 10.1088/0022-3727/48/46/465203.
- [174] Franko Greiner et al. “Imaging Mie ellipsometry: dynamics of nanodust clouds in an argon–acetylene plasma”. In: *Plasma Sources Science and Technology* 21.6 (2012), p. 065005. DOI: <http://stacks.iop.org/0963-0252/21/i=6/a=065005>.
- [175] F.R.A. Onofri, M. Wozniak, and S. Barbosa. “On the Optical Characterisation of Nanoparticle and their Aggregates in Plasma Systems”. In: *Contributions to Plasma Physics* 51.2-3 (2011), pp. 228–236. DOI: 10.1002/ctpp.201000056.
- [176] S Barbosa et al. “In-situ characterisation of the dynamics of a growing dust particle cloud in a direct-current argon glow discharge”. In: *Journal of Physics D: Applied Physics* 49.4 (2016), p. 045203. DOI: 10.1088/0022-3727/49/4/045203.
- [177] S Dap et al. “Agglomeration processes in carbonaceous dusty plasmas, experiments and numerical simulations”. In: *New Journal of Physics* 12.9 (2010), p. 093014. DOI: 10.1088/1367-2630/12/9/093014.
- [178] I. Denysenko et al. “The response of a capacitively coupled discharge to the formation of dust particles: Experiments and modeling”. In: *Physics of Plasmas* 13.7 (2006), p. 073507. DOI: 10.1063/1.2222258.

- [179] J. Berndt et al. “Some Aspects of Reactive Complex Plasmas”. In: *Contributions to Plasma Physics* 49.3 (2009), pp. 107–133. DOI: 10.1002/ctpp.200910016.
- [180] A. von Keudell and W. Jacob. “Growth and erosion of hydrocarbon films investigated by in situ ellipsometry”. In: *Journal of Applied Physics* 79.2 (1996), pp. 1092–1098. DOI: 10.1063/1.360796.
- [181] Lavanya Ravi and Steven L. Girshick. “Coagulation of nanoparticles in a plasma”. In: *Phys. Rev. E* 79.2 (2009), p. 026408. DOI: 10.1103/PhysRevE.79.026408.
- [182] E. Jerby et al. “Nanoparticle plasma ejected directly from solid copper by localized microwaves”. In: *Applied Physics Letters* 95.19 (2009), p. 191501. DOI: 10.1063/1.3259781.
- [183] J. B. A. Mitchell et al. “Evidence for Nanoparticles in Microwave-Generated Fireballs Observed by Synchrotron X-Ray Scattering”. In: *Phys. Rev. Lett.* 100.6 (2008), p. 065001. DOI: 10.1103/PhysRevLett.100.065001.
- [184] Michael Sztucki and Theyencheri Narayanan. “Development of an ultra-small-angle X-ray scattering instrument for probing the microstructure and the dynamics of soft matter”. In: *Journal of Applied Crystallography* 40.s1 (2007), s459–s462. DOI: 10.1107/S0021889806045833.
- [185] Tilo Peter et al. “Influence of reactive gas admixture on transition metal cluster nucleation in a gas aggregation cluster source”. In: *Journal of Applied Physics* 112.11 (2012), p. 114321. DOI: 10.1063/1.4768528.
- [186] C. R. Gorla et al. “Silicon and germanium nanoparticle formation in an inductively coupled plasma reactor”. In: *Journal of Vacuum Science & Technology A: Vacuum, Surfaces, and Films* 15.3 (1997), pp. 860–864. DOI: 10.1116/1.580721.
- [187] B. Giesen et al. “Formation of Si-nanoparticles in a microwave reactor: Comparison between experiments and modelling”. In: *Journal of Nanoparticle Research* 7.1 (2005), pp. 29–41. DOI: 10.1007/s11051-005-0316-z.
- [188] Ameya Bapat et al. “A plasma process for the synthesis of cubic-shaped silicon nanocrystals for nanoelectronic devices”. In: *Journal of Physics D: Applied Physics* 40.8 (2007), p. 2247. DOI: 10.1088/0022-3727/40/8/S03.

- [189] H Kersten et al. “Micro-disperse particles as probes for plasma surface interaction”. In: *Thin Solid Films* 377-378 (2000), pp. 530–536. DOI: [https://doi.org/10.1016/S0040-6090\(00\)01439-5](https://doi.org/10.1016/S0040-6090(00)01439-5).
- [190] V Schulz-von der Gathen et al. “Diagnostic studies of species concentrations in a capacitively coupled RF plasma containing CH₄-H₂-Ar”. In: *Plasma Sources Science and Technology* 10.3 (2001), p. 530. DOI: 10.1088/0963-0252/10/3/318.
- [191] F Hempel et al. “Monitoring of hydrocarbon concentrations in dust-producing RF plasmas”. In: *Plasma Sources Science and Technology* 21.5 (2012), p. 055001. DOI: 10.1088/0963-0252/21/5/055001.

Acknowledgments

I would like to thank Prof. Dr. Franz Faupel and Prof. Holger Kersten for giving me the opportunity to work in their groups during my doctorate. It has been a great time and I very much enjoyed the freedom they provided me. From the beginning of my doctorate I have felt like a valued member of their groups and an independent researcher. I am also very grateful for their support during my search for a suitable Postdoc position. I would also like to thank Prof. Kersten once more for organising my stay at the University of Kyushu in Fukuoka, Japan. It has been a wonderful time, which I will remember for the rest of my life.

I would also like to thank Dr. Vladimir Zaporozhchenko for giving me my first job in the Chair for Multicomponent Materials. He left this world too early for the last big adventure. I miss him and his supervision. I find solace in the thought that he would have been delighted that I stayed at the Chair for Multicomponent Materials for so long and will start my tenure as a Postdoc at the University of Cambridge in a few days.

I would also like to thank the other members of the Chair for Multicomponent Materials. I think we had a great time together. Special thanks goes to Dr. Tilo Peter, a former supervisor of mine. I learned a lot from him about how to doctorate. I would also like to thank Dr. Viktor Schneider, who has been an ideal office mate, and has become a friend of mine. I am confident that he will find his way in this world. I am especially grateful for having met Brook Shurtleff. From my perspective, he is a fountain of wisdom and has encouraged me to start traveling the world and finding out where I belong. I regret that he had to spend the night shifts during the worst beamtime ever with me at the P03 beamline. He had deserved better. Talking of beamtimes, I would also like to thank Dr. Oleksandr Polonskyi for having spend numerous beamtimes together with me at P03. When he was around, the shifts didn't appear to be that long. I would also like to thank him for acting as my supervisor when I needed one.

I would also like to thank Erik von Wahl, Fabian Haase, and Thorben Kewitz for letting me join them for a short road trip in the United States. It was awesome.

I am also grateful for having met Gary Owston. I have met him only on six occasions, each time for less than three hours. Nevertheless, he managed to teach me more about speaking the English language and giving wonderful presentation than all my other teachers before.

Most importantly, I owe a great debt of gratitude to my family. They have always supported me and I wouldn't be the person who I am without them.

List of Publications

In chronological order:

1. *P. Solar, O. Polonskyi, A. Olbricht, **A. Hinz**, A. Shelemin, O. Kylian, A. Choukourov, F. Faupel, H. Biederman*, Scientific Reports (**2017**), Single-step generation of metal-plasma polymer multicore@shell nanoparticles from the gas phase
doi: 10.1038/s41598-017-08274-6
2. *A. M. Ahadi, **A. Hinz**, O. Polonskyi, T. Trottenberg, T. Strunskus, H. Kersten, F. Faupel*, J. of Vac. Sci. and Tech. A (**2016**), Modification of a metal nanoparticle beam by a hollow electrode discharge
doi: 10.1116/1.4936188
3. *Th. Wegner, **A. M. Hinz**, F. Faupel, T. Strunskus, H. Kersten, and J. Meichsner*, Appl. Phys. Lett. (**2016**), Influence of nanoparticle formation on discharge properties in argon-acetylene capacitively coupled radio frequency plasmas
doi: 10.1063/1.4941806
4. ***A. M. Hinz**, E. von Wahl, F. Faupel, T. Strunskus and H. Kersten*, J. Phys. D: Appl. Phys. (**2015**), Versatile particle collection concept for correlation of particle growth and discharge parameters in dusty plasmas
doi: 10.1088/0022-3727/48/5/055203
5. *O. Polonskyi, T. Peter, A. M. Ahadi, **A. Hinz**, T. Strunskus, V. Zaporozhchenko, H. Biederman, and F. Faupel*, Appl. Phys. Lett. (**2013**), Huge increase in gas phase nanoparticle generation by pulsed direct current sputtering in a reactive gas admixture
doi: 10.1063/1.4816036
6. ***A. Hinz**, E. von Wahl, F. Faupel, T. Strunskus, and H. Kersten*, Nanoparticle forming reactive plasmas: a multidagnostic approach accepted by EPJ D
7. *O. Polonskyi, A. M. Ahadi, T. Peter, K. Fujioka, J. W. Abraham, E. Vasiliauskaite, **A. Hinz**, T. Strunskus, S. Wolf, M. Bonitz, H. Kersten, and F. Faupel*, Plasma based formation and deposition of metal and metal oxide nanoparticles using a gas aggregation source accepted by EPJ D

8. *J. W. Abraham, A. Hinz, T. Strunskus, F. Faupel, M. Bonitz*, Formation of polymer-based nanoparticles and nanocomposites by plasma-based deposition methods
accepted by EPJ D